University of Alberta

Advanced Silicon Microring Resonator Devices for Optical Signal Processing

by

Ashok Prabhu Masilamani

A thesis submitted to the Faculty of Graduate Studies and Research
in partial fulfillment of the requirements for the degree of

Doctor of Philosophy
in
Photonics and Plasma

Electrical and Computer Engineering

Spring 2012
Edmonton, Alberta

This thesis is dedicated

to my wife Meena

and

to my parents and siblings

Abstract

Chip level optical interconnects has gained momentum with recent demonstrations of silicon-on-insulator (SOI) based photonic modules such as lasers, modulators, wavelength division multiplexing (WDM) filters, etc. A fundamental building block that has enabled many of these silicon photonic modules is the compact, high Q factor microring resonator cavity. However, most of these demonstrations have WDM processing components based on simple add-drop filters that cannot realize the dense WDM systems required for the chip level interconnects. Dense WDM filters have stringent spectral shape requirements such as flat-top filter passband, steep band transition etc. Optical filters that can meet these specifications involve precise placement of the poles and zeros of the filter transfer function. Realization of such filters requires the use of multiple coupled microring resonators arranged in complex coupling topologies. In this thesis we have proposed and demonstrated new multiple coupled resonator topologies based on compact microring resonators in SOI material system.

First we explored novel microring architectures which resulted in the proposal of two new coupled microring architectures, namely, the general 2D microring array topology and the general cascaded microring network topology. We also developed the synthesis procedures for these two microring architectures. The second part of this thesis focussed on the demonstration of the proposed architectures in the SOI material system. To accomplish this, a fabrication process for SOI was developed at the UofA Nanofab facility. Using this process, ultra-compact single microring filters with microring radii as small as 1μm were demonstrated. Higher order filter demonstration with multiple microrings necessitated post-fabrication microring resonance tuning. We developed additional fabrication steps to install micro heaters on top of the microrings to thermally tune its resonance. Subsequently, a thermally tuned fourth order filter response based on the cascaded microring architecture was demonstrated.

Acknowledgements

I am deeply grateful to my supervisor Dr. Vien Van for his guidance, support and mentorship throughout the entire duration of this doctoral work. Without his support this thesis work wouldn't have been possible. I was also very fortunate to work at the UofA Nanofab which is the host for several cutting edge nano fabrication technologies. Once again I must thank Dr. Van who enabled my work at Nanofab which was truly a great experience.

Life at my lab (NPRL) and Nanofab was made largely pleasant by my colleagues. Steve Buswell in particular was a great friend and a colleague throughout my graduate school years and I am very thankful to him for the countless valuable discussions from which I learned a great deal about nanofabrication process development.

My thanks goes out to my other colleagues from NPRL which include Tracy Liew, David Perron, Marcelo Wu, Alan Tsay, Siamak Abdollahi, Daniel Backman and Cameron Horvath who contributed in many technical discussions as well as in my philosophical ponderings. I will miss taking part in the witty conversations and friendly banters at NPRL which provided a balance to the intensive technical demands of graduate school.

I also value the support from various colleagues at the Nanofab whose contribution to the process development was vital. In particular I am very grateful to all the Nanofab staff members who were very helpful throughout my stint there. Many thanks to Mike O'Tool from National Institute of NanoTechnology who helped with wire bonding of my chips. I am also thankful to Dr. Raymond Decorby and his student Dr. Nakkeeran who shared some of their equipments for my experiments.

Finally, thanks to my wife Meena and my family for their love and support.

Table of Contents

List of Figures

List of Tables

List of Symbols

R	microring radius in m
λ_0	operating wavelength in μm
n	refractive index of the medium
n_{eff}	effective index of the waveguide
n_g	group index of the waveguide
v_g	group velocity in ms^{-1}
m	longitudinal mode number
L_{coup}	effective physical length of a coupling junction in μm
κ_c	per unit length coupling strength
κ	field coupling coefficient
τ	field transmission coefficient
S_i	input port optical signal
S_d	drop port optical signal
S_t	through port optical signal
S_a	add port optical signal
A_{rt}	roundtrip power attenuation
β	propagation constant of the optical waveguide
$\Delta\phi$	roundtrip phase of the microring
Δf_{3dB}	3dB bandwidth
F	finesse
Q	quality factor
$A(t)$	energy signal in the microring
$U(t)$	power signal circulating inside the microring
ω	frequency in rad/s
ω_0	resonant frequency of a microring resonator
μ	energy coupling coefficient
γ	energy decay rate in a microring
γ_L	energy loss due to intrinsic losses in a microring

α	power attenuation coefficient in m^{-1}
V_{in}^{+}	normalized voltage wave at input port
V_{in}^{-}	normalized voltage wave at through port
V_{out}^{+}	normalized voltage wave at add port
V_{out}^{-}	normalized voltage wave at drop port
S_{11}	input reflection coefficient
S_{22}	output reflection coefficient
S_{12}	input transmission coefficient
S_{21}	output transmission coefficient
X	capacitive coupling element
Y	admittance
Z	impedance
s	frequency variable
$S_t(s)$	through port transfer function
$S_d(s)$	drop port transfer function
p	filter poles
z	filter zeros
ψ	differential π-phase shift element
g	coupling gap in nm
$\frac{dn}{dT}$	thermo-optic coefficient of a material in K^{-1}
t_{clad}	upper cladding thickness in μm
T_{top}	temperature at the top of the upper cladding in °C
P_{top}	power dissipation at the top of the upper cladding in W
k	thermal conductivity of a material in W/(m·K)
R_{thin}	thin film resistance in Ω
ρ	resistivity in Ω.m

Chapter 1
Introduction

Silicon based Very Large Scale Integrated (VLSI) Complementary Metal Oxide Semiconductor (CMOS) electronic devices have made a massive impact in the information technology and networking industry, triggering an exponential growth in the computing and consumer electronics market over the past several decades. However, over the last few years, the combination of information and networking technologies has witnessed huge volumes of data transfers between computing nodes due to demanding internet based applications such as, "video-on-demand", voice over internet protocol (VOIP), etc. These new web enabled electronic devices are further demanding increase in processing speeds, faster data transfer rates, low power consumption and smaller form factors. The recent advances in silicon fabrication technology have reduced the electronic circuit feature sizes to a few tens of nanometer. While this has enabled further miniaturization of electronic devices, it has become increasingly difficult to push the limits of processing speed and data transfer rates along with keeping power consumption minimal. Especially with the high volumes of data, the conventional data transfer technology which is based on electrical interconnects is heavily strained. For example, the distribution of the clock signal has been estimated to dissipate up to 50% of the total chip power in a processor chip. Power dissipation and routing length constraints (RC delay and skewing) has stagnated the clock signal close to 3GHz. Also other critical signals like the Input/Output (I/O) bus signals running between various processor units

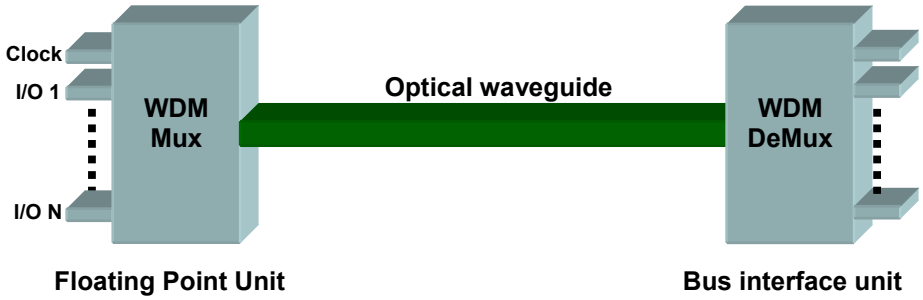

Figure 1.1. An optical interconnect layer within a processor.

are facing similar issues with routing. As a solution to this problem, optical waveguides are being explored as an interconnect technology for clock and signal distribution within high performance processors [1]. An example is illustrated in Figure 1.1 where a single optical waveguide along with wavelength division multiplexing (WDM) technology can carry multiple critical high speed signals in a multiplexed format between two blocks within a processor.

1.1 Optical interconnects

For several decades, electrical interconnects have been the primary mode of data transfer, from macro level twisted pair copper wire for Ethernet local area network (LAN) computer networking all the way down to the aluminum interconnects used within the microchips. Similarly, optical interconnects based on the mature fibre optic WDM technology was the workhorse for long distance telecommunications data transfers for almost 30 years. Fibre optic technology, offers many attractive features such as

- very high bandwidth interconnections,
- WDM based low interference interconnections,
- ultra fast optical information processing.

In spite of this, it was still largely restricted to long distance communications (> 100 km) due to the high costs involved with single mode fibre optic links. But in the 1990's multimode fibre (MMF) and light emitting diode (LED) based low cost optical interconnects slowly replaced the building-wide computer interconnections, namely, the LAN campus backbones. The early 2000's saw the high speed LAN standards [2, 3] and the 10Gbps fibre channel [4], driving the use of a low cost vertical cavity surface

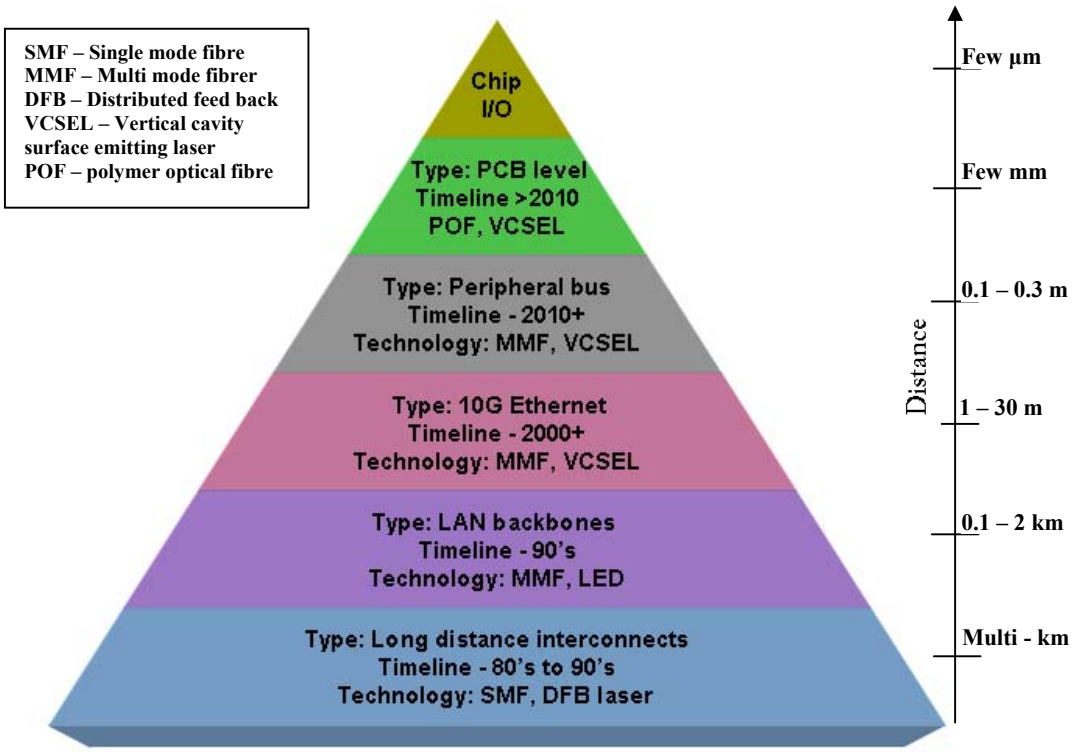

Figure 1.2. Time chart of optical interconnects.

emitting laser (VCSEL) based MMF fibre optic link which replaced the twisted pair copper wire based LAN cables for links with distances covering more than a few tens of meter. Optical interconnects are also making inroads into computer peripheral level interconnections with the proposal of "Lightpeak" fibre optic PC peripheral bus standard by Intel in 2009 [5]. Lightpeak is expected to work at up to 100Gbps data rates and is aimed to replace the several existing electronic peripheral interconnect technologies like universal serial bus (USB), Firewire, high definition multi-media interface (HDMI), etc. In the near future, optical interconnects are expected to replace the copper based printed circuit board traces especially in PC motherboards where routing 64 bit high speed bus signals in the printed circuit board (PCB) has become increasingly difficult. Several research groups have been working with polymer optical waveguides to serve as an inter-chip level interconnection for PCBs [6, 7]. The evolution of optical interconnect technologies over the past few decades is charted in Figure 1.2.

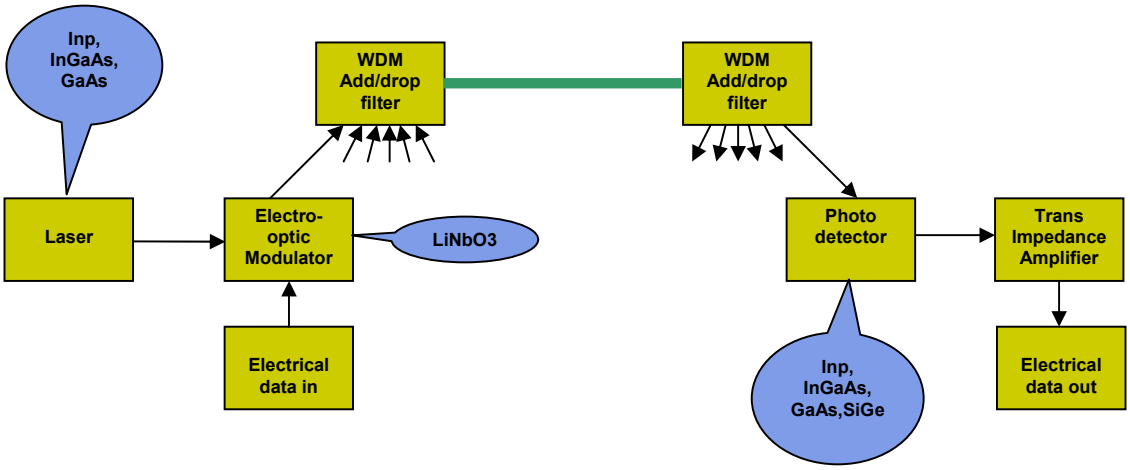

Figure 1.3. A conventional optical link along with conventional material systems for each block.

In the chart, all the optical links have corresponding electro-optical interface devices such as the laser diodes, photo diodes, etc. and WDM devices such as filters, modulators, amplifiers, etc. To realize intra chip level optical interconnects these photonic devices have to comply with the established CMOS VLSI technology. However, integration of photonic devices faces several technological hurdles. Currently a variety of material systems such as gallium arsenide (GaAs), indium phosphide (InP), indium gallium arsenide (InGaAs), and lithium niobate ($LiNbO_3$), are being used to realize various photonic devices. Figure 1.3 shows a complete optical link with discrete optical blocks made from different material systems. There is no single monolithic material from which all photonic devices could be fabricated. Also, the fabrication technology in these material systems are not as matured as the CMOS technology, which causes a major bottleneck in achieving large scale integration as well as lowering manufacturing costs.

1.2 Silicon photonics

To overcome the above-mentioned difficulties, two approaches based on the silicon material system [8, 9] and CMOS fabrication methodology [10, 11] have been considered in the optical research arena:

1) The first approach is to use silicon as a photonic material. The fabrication technology for silicon is very mature. It supports very large scale integration and

has already reached the nano meter scale fabrication dimensions. However, silicon does not have a direct band gap and hence, is a poor light emitter. Light emission and many signal processing functions in silicon are based on non-linearity which requires high optical intensities, leading to high power consumption. Nevertheless, recent progress has enabled various discrete photonic components based on silicon, such as Electro-Optic (EO) modulators [12 - 15], Raman lasers [16] and optical switching components [17 - 19], to be demonstrated.

2) The second approach is to use silicon along with other photonic material systems like germanium, indium phosphide or gallium arsenide to realize active devices required for the optical interconnect layer. This is called the hybrid silicon platform. To date, several discrete components such as hybrid silicon lasers [20 - 23], EO modulators [24, 25] and photo detectors [26, 27] have been reported. In 2010 researchers from Intel demonstrated a 50Gbps complete WDM optical link using the hybrid silicon platform [28].

In spite of the differences in the approach, hybrid or monolithic, silicon based photonic devices are gaining interest as devices of the future. Silicon-on-insulator (SOI), SiO_2 glass, Si_3N_4, etc. are some of the Si-based material systems that are being explored for this purpose. From a fabrication perspective it is interesting to note that all three material systems are currently being used in CMOS fabrication, which is an added benefit. Of these material systems, the SOI material system has the advantage of high index contrast, which allows the realization of compact photonic elements based on strongly-confined silicon wires with sub-micrometer dimensions and tight bending radii.

1.2.1 Silicon microring resonators

In the VLSI electronics technology, the MOSFET serves as a basic building block to build complex functionalities. Similarly, there is a need for a photonic building block that would play a vital role in realizing advanced functionalities in integrated photonics. A central element in photonic devices technology is an optical resonator, which enables several fundamental photonic functionalities such as light generation, modulation,

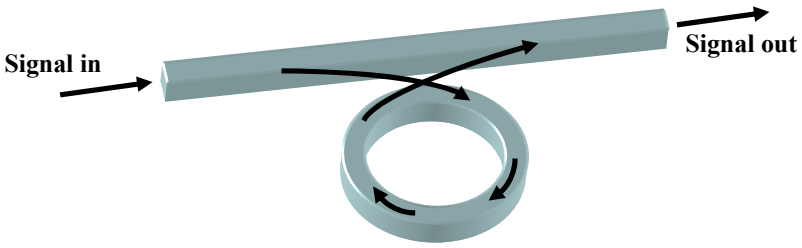

Figure 1.4. A microring resonator in all pass configuration.

filtering and other optical signal processing units. It is thus desirable to have an optical resonator in SOI material system that can not only be used to accomplish a great variety of optical signal processing functions, but lends itself to the miniaturization and large scale integration of silicon photonic devices. One such element is the microring resonator, whose compact size and versatility has been demonstrated to greatly enhance the functionality of VLSI silicon photonic circuits. A microring resonator is a whispering-gallery-mode, high quality (Q) factor, ring shaped optical cavity with typical diameters in the range of several hundred micrometers to several micrometers. Figure 1.4 shows a microring resonator in a typical configuration alongside a straight optical waveguide for coupling light in and out of the ring evanescently. Advances in fabrication techniques over the past few years have enabled microring resonators with extremely high Q factors (i.e. low loss) to be realized, with typical Q values in the range of 10^4–10^6 [29]. Microring resonators have been demonstrated in various material systems, including SiO_2 glass [30, 31], SiN [32, 33], SiON [34], silicon-on-insulator [35, 36], semiconductors [37, 38], and polymers [39, 40]. Due to their compact sizes, high Q factors and strong dispersion characteristics, microring resonators have played a key role in various optical spectral engineering applications such as add/drop filters for wavelength division multiplexing (WDM) systems [41], dispersion compensators [42, 43], optical delay lines [44], microwave photonic filters [45], and wavelength selective mirrors for lasers [46]. Their high Q factors also enable enhanced optical non-linearity to be realized at low power consumption.

1.3 Research goals of the thesis

The microring based silicon photonic devices discussed in the previous section have fuelled much research interest in CMOS integrated photonic devices. Currently much of

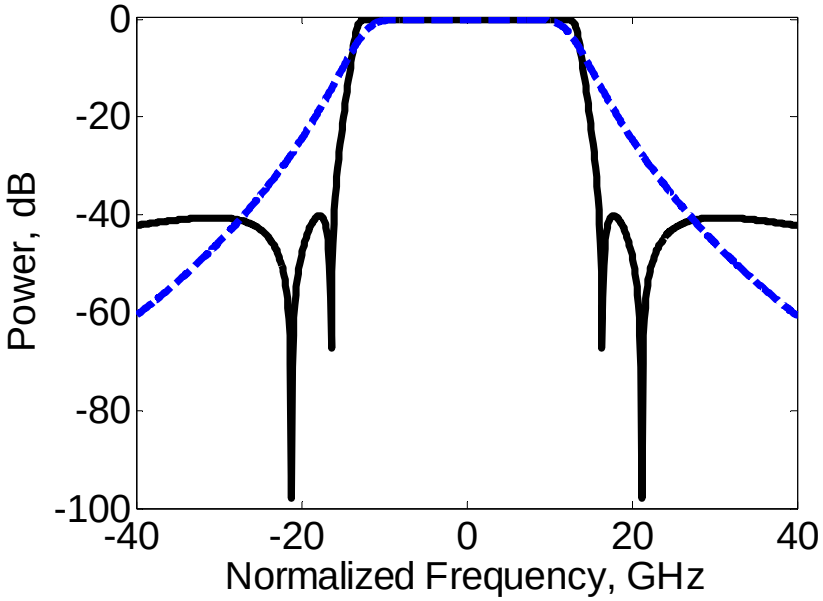

Figure 1.5. A 4th order Elliptic filter response (Black line) along with a butterworth filter response (dotted blue line) of same order.

these demonstrated systems have WDM processing components based on simple add-drop filters with simple spectral characteristics such as the Butterworth filter response shown by the dotted blue curve in Figure 1.5. As the integration gets denser and the interconnect speed increases, many of these applications are expected to switch to Dense WDM (DWDM) systems. DWDM systems are currently in use for high capacity, long distance telecommunication networks and often have very stringent requirements for the spectral characteristics of add-drop filters, such as flat-top passband, steep band transition, high adjacent channel isolation, linear dispersion slope or constant group delay. Such spectral characteristics, as shown by the black curve in Figure 1.5, can be achieved only by more advanced filters such as the elliptic or inverse Chebyshev type. The design of elliptic and inverse Chebyshev optical filters that can meet these specifications involves the precise placement of the poles and zeros of the filter transfer function, whose realization often requires the use of multiple coupled microring resonators arranged in complex coupling topologies.

Based on these premises, it is expected that advanced add-drop filters based on compact SOI microrings would play a vital role in on-chip WDM optical interconnects in the near future. This led us to set a broader goal for this thesis: ***to explore, propose and***

demonstrate new coupled resonator topologies based on microring resonators in SOI material system which can be used to realize complex optical transfer functions. Specifically, the aim is to realize ultra compact SOI microrings and use them to demonstrate advanced optical filters based on new coupling topologies. We believe that these devices would be an integral part in silicon based optical interconnect technology as well as other optical signal processing applications.

Specific objectives of the thesis

The specific objectives of the thesis are as follows:

- Explore new coupled microring architectures that could overcome the disadvantages of existing microring filter architectures.
- Develop analysis and synthesis techniques for these new coupled microring architectures.
- Explore the application of the proposed coupling topologies to realize advanced signal processing functions.
- Experimentally demonstrate microring filters in the SOI platform.
- Explore the limits of miniaturization of microring resonators in SOI to reduce the device foot prints.
- Develop the fabrication process for SOI material system with integrated micro heater elements.
- Demonstrate thermo-optic control and tunability of microring filters using micro heaters.

1.4 Summary

This chapter outlined the background and the growing interest in integrated silicon based photonic devices for future on-chip interconnects. It also highlighted the emergence of SOI material system and silicon microring resonators as potential candidates for integration of photonic devices. The necessity to realize high order WDM filters for dense WDM systems was identified based on which, specific goals as listed in the previous section were set for the thesis work.

Chapter 2
Microring Resonator Filters and Characteristics

In this chapter we give an overview of microring resonator filters and their various spectral characteristics. An equivalent circuit model for a single microring add-drop filter is introduced. Also the existing microring filter architectures reported in the literature are reviewed and their advantages and disadvantages are highlighted.

2.1 Microring resonator

A microring resonator is a travelling wave optical resonator in a ring shaped structure which is usually formed by bending a rectangular dielectric optical waveguide into a circular loop as shown in Figure 2.1(a). Typically, microrings have bending radii in the range of tens or hundreds of micrometers. Light can be coupled in and out of this structure by placing a straight optical waveguide in close proximity to the ring as shown in Figure 2.1(a). This configuration of the microring is called the all-pass configuration as signals at all frequencies are transmitted under lossless condition. The evanescent coupling between the input bus and the ring waveguide leads to the transfer of power from the bus waveguide into the ring cavity. The coupled light then propagates along

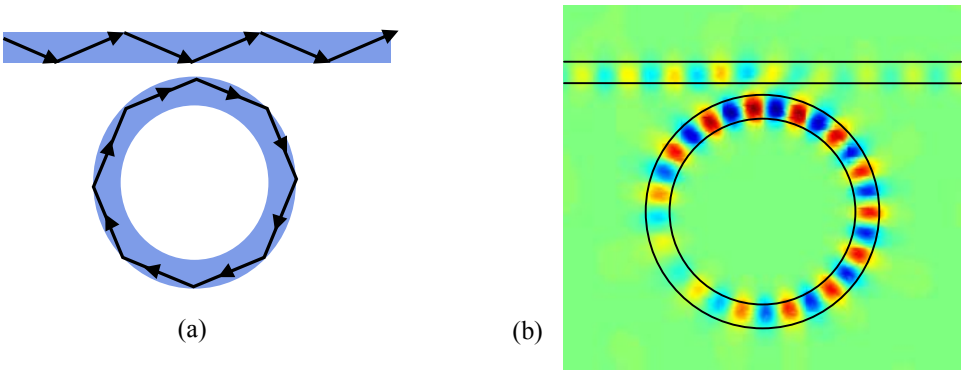

Figure 2.1 (a) Schematic of an all pass microring configuration with ray tracing. (b) 2D-FDTD simulation result of electric field in an all pass microring.

the circumference of the ring by total internal reflections as shown by the black ray trace in Figure 2.1(a). Figure 2.1(b) shows the electric field distribution inside a microring obtained from a numerical simulation using the 2D finite difference time domain (FDTD) technique. The microring is a closed loop structure and only certain optical frequencies can resonate in the ring. These resonant frequencies are determined by the resonance condition as given by

$$2\pi R = m\lambda_0 / n_{eff} \qquad (2.1)$$

where R is the radius of the ring, m is an integer and represents the longitudinal mode number, n_{eff} is the effective index of the ring waveguide so that λ_0/n_{eff} is the guided wavelength of the light propagating in the ring. The resonance condition requires the circumference of the ring to be equal to an integral multiple of the guided wavelengths.

Considering the coupling junction of the microring in Figure 2.1(a), the evanescent tails extending from the modes of the straight waveguide and the ring waveguide overlap with each other, leading to power transfer between them. A better visualization of this mode overlap is shown in Figure 2.2. From coupled mode theory of dielectric waveguides one could deduce the amount of field coupling between the bus and the ring. Considering the junction as a point junction with no physical length, the field coupling strength κ between the two waveguides could be defined.

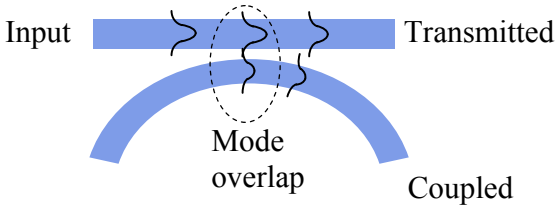

Figure 2.2. Mode overlap at the coupling junction.

In reality the coupling junction would have an effective physical length L_{coup} so that the field coupling coefficient κ per unit length coupling strength is calculated from [87] as

$$\kappa = \sin(\kappa_c L_{coup}) \tag{2.2}$$

where κ_c is the per unit length coupling strength. The remaining power transmitted in the straight waveguide can then be quantified by the power transmission coefficient τ^2. From power conservation, we obtain

$$|\kappa|^2 + |\tau|^2 = 1. \tag{2.3}$$

2.2 Microring resonator as an add-drop filter

To study the properties of the microring resonator from a WDM filter perspective, consider an add-drop microring resonator with radius R. In the add-drop configuration, the microring consists of two bus waveguides placed near to it as shown in Figure 2.3. The input optical signal S_i consisting of several multiplexed WDM channels

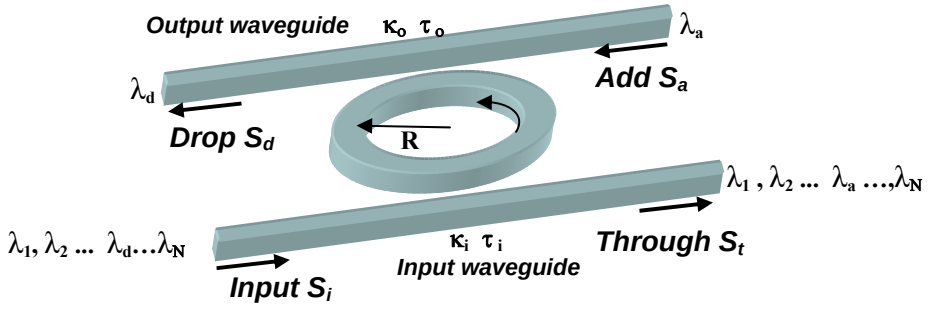

Figure 2.3. Schematic of an add-drop microring configuration.

including the drop channel of interest enters the input bus waveguide. The drop wavelength λ_d is the same as the resonant wavelength of the microring so that only the drop signal can couple into the microring via the power coupling coefficient κ_i^2 and resonates in the microring. This signal is subsequently transmitted to the drop port in the output waveguide via the coupling coefficient κ_o^2. An add signal S_a at the resonant wavelength λ_a can also be applied to the add port and gets added to the through signal S_t along with all the off-resonance wavelengths. The drop-port and the through-port spectral responses of the microring can be derived as [35]

$$\left|\frac{S_d}{S_i}\right|^2 = \frac{\kappa_i^2 \kappa_o^2 A_{rt}^{1/2}}{1 - 2\tau_i \tau_o A_{rt}^{1/2} \cos(\Delta\phi) + \tau_i^2 \tau_o^2 A_{rt}}, \tag{2.4}$$

$$\left|\frac{S_t}{S_i}\right|^2 = \frac{\tau_i^2 + \tau_o^2 A_{rt} - 2\tau_i \tau_o A_{rt}^{1/2} \cos(\Delta\phi)}{1 - 2\tau_i \tau_o A_{rt}^{1/2} \cos(\Delta\phi) + \tau_i^2 \tau_o^2 A_{rt}}, \tag{2.5}$$

where A_{rt} is the roundtrip power attenuation, $\tau_i^2 = 1 - \kappa_i^2$, $i = \{1, 2\}$, are the power transmission coefficients, $\Delta\phi = 2\pi R\beta$ is the roundtrip phase of the microring and β is the propagation constant of the optical waveguide. Figure 2.4 shows the plotted spectral responses of the drop and through ports of a typical add-drop filter. At the resonant wavelength λ_d, the drop port S_d has total transmission due to the constructive interference occurring in the microring, while destructive interference occurring at the coupling junction between through port and the microring leads to total extinction at the through port S_t. The spectral characteristics observed in Figure 2.4 are discussed below.

3dB bandwidth (FWHM)

As shown in Figure 2.4, the bandwidth of the resonator is the full width of the resonance measured at half power (-3dB point) from the peak. The 3dB bandwidth is a very important quantity that determines the maximum data rate at which the optical channel can operate at the corresponding resonance. The expression for the full-width at half-maximum (FWHM) bandwidth of the microring is obtained by equating the drop

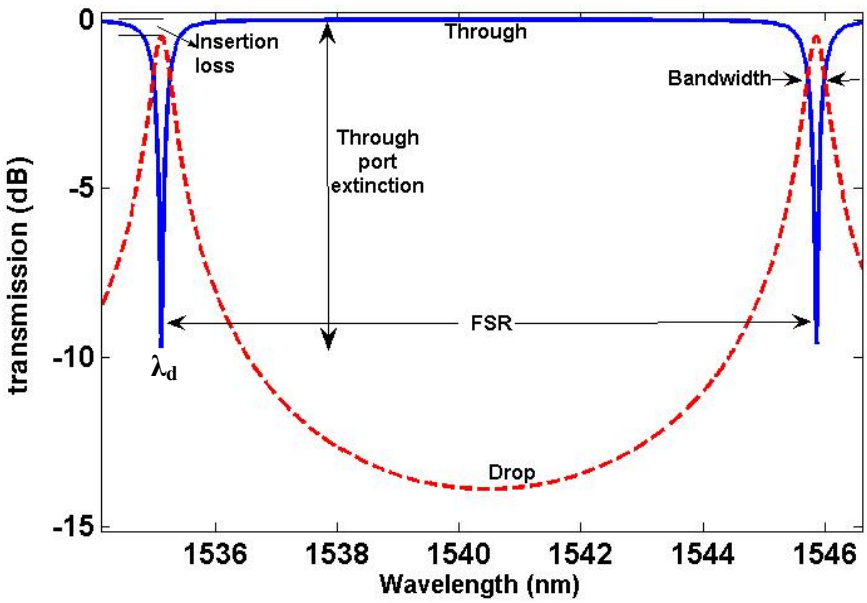

Figure 2.4. Add drop microring spectral response.

port equation (2.4) to 1/2. Using the approximation $\cos(\Delta\phi) = 1 - (\Delta\phi)^2/2$ for small angles, the bandwidth can be derived to give:

$$\Delta f_{3\mathrm{dB}} \approx \frac{c}{2\pi^2 R n_{eff}} \cdot \frac{1 - \tau_1 \tau_2 A_{rt}^{1/2}}{\sqrt{\tau_1 \tau_2 A_{rt}^{1/2}}} \tag{2.6}$$

where c is the speed of light, R is the radius of the microring, n_{eff} is the effective index of the microring waveguide.

Free Spectral Range (FSR)

Free spectral range is another important quantity of the microring which is defined as the spectral span between two successive resonances defined by two consecutive longitudinal mode numbers. The FSR can be obtained from the resonance condition of the microring given in equation 2.1, which gives the following results expressed in both wavelength and frequency domains as

$$FSR_\lambda \approx \frac{\lambda_0^2}{2\pi R n_g}, \qquad FSR_f \approx \frac{c}{2\pi R n_g}, \tag{2.7}$$

where n_g is the group index of the microring. Along with the 3dB resonance bandwidth, the FSR determines how many data channels the add-drop microring filter can accommodate. Another useful quantity is the normalized bandwidth which is given as

$$\frac{\Delta f_{3\text{dB}}}{FSR} \approx \frac{1-\tau_1\tau_2 A_{rt}^{1/2}}{\pi\sqrt{\tau_1\tau_2 A_{rt}^{1/2}}}. \tag{2.8}$$

Insertion loss (I.L)

Insertion loss is the difference between the peak power of the drop port response and the off resonance power level in the through port. In a WDM system this quantifies the loss encountered by an optical channel which is either being dropped or added in to the system. The peak power in the drop port occurs at $\cos(\Delta\phi) = 1$ in equation 2.4, from which the insertion loss is obtained as:

$$I.L = \left|\frac{S_d}{S_i}\right|^2_{\max} = \frac{\kappa_i^2 \kappa_o^2 A_{rt}^{1/2}}{\left(1-\tau_i\tau_o A_{rt}^{1/2}\right)^2}. \tag{2.9}$$

Through port extinction (T.P.E)

This quantity directly relates to the measure of the cross talk between adjacent channels and plays a crucial role in dense WDM systems. It is defined as the minimum power of the through port at resonance $\left(\cos(\Delta\phi) = 1\right)$ with respect to the off resonance power, giving the following expression

$$T.P.E = \left|\frac{S_t}{S_i}\right|^2_{\min} = \left(\frac{\tau_i - \tau_o A_{rt}^{1/2}}{1-\tau_i\tau_o A_{rt}^{1/2}}\right)^2. \tag{2.10}$$

Critical Coupling

The maximum through port extinction occurs when equation 2.10 becomes zero which leads to the following expression:

$$\tau_i = \tau_o A_{rt}^{1/2}. \tag{2.11}$$

The above condition is called the critical coupling condition. This condition relates the internal losses of the microring represented by the roundtrip power attenuation A_{rt} to the external losses represented by the transmission coefficients.

Finesse (F)

This quantity signifies the number of filter passbands that could fit within a single FSR. Given the 3dB bandwidth and the FSR of the microring, the finesse F of the resonator is simply the ratio of the FSR to the 3dB bandwidth

$$\frac{FSR}{\Delta f_{3\mathrm{dB}}} \approx \frac{\pi\sqrt{\tau_1\tau_2 A_{rt}^{1/2}}}{1-\tau_1\tau_2 A_{rt}^{1/2}}. \tag{2.12}$$

Since each filter passband corresponds to an optical channel, the finesse gives an estimate of the number of optical channels that can be accommodated for a given microring add-drop filter.

Quality factor (Q)

The quality factor is a measure of the sharpness of the microring resonance which can be expressed as the ratio of the resonant frequency f_0 to the bandwidth given as

$$Q = \frac{f_0}{\Delta f_{3\,dB}} = \frac{2\pi^2 R n_{eff}}{\lambda} \frac{\sqrt{\tau_1\tau_2 A_{rt}^{1/2}}}{1-\tau_1\tau_2 A_{rt}^{1/2}}. \tag{2.13}$$

Equation 2.13 gives the overall quality factor of the add-drop filter, which could be further split into an intrinsic Q factor due to intrinsic losses and an extrinsic Q factor representing power extracted at the coupling junction.

$$\frac{1}{Q} = \frac{1}{Q_{\mathrm{int}}} + \frac{1}{Q_{ext}}. \tag{2.14}$$

Intrinsic Losses

A microring resonator experiences loss from different mechanisms which are generally known as intrinsic losses. The four major mechanisms causing intrinsic losses are:

- Radiation loss due to bending,
- Loss due to scattering at the waveguide sidewalls,
- Scattering loss at coupling junctions,
- Loss due to material absorption.

The optical mode in a bent waveguide experiences some amount of its power pushed out of the outer sidewall of the waveguide, which gets radiated. The smaller the bend radius, the larger the power extended outside causing subsequent loss through radiation. This loss could be reduced by using material systems with high index contrast like silicon-on-insulator, which offers waveguides with high power confinement. Bending loss is inversely proportional to the bending radius and the square of the index contrast. Therefore high index contrast materials such as SOI are better suited for fabricating microring resonators with smaller footprints and hence, have the potential for denser photonic integration.

Loss due to scattering at the sidewalls is mostly due to fabrication imperfections causing roughness in the etched sidewalls. Depending on the fabrication process used to define the waveguides, the surface roughness of the sidewalls could be approximately estimated. For e.g. for a thin silicon waveguide with dimensions 300x300nm^2, it would be better if the side wall roughness is within a few nanometers to avoid substantial loss. Scattering loss also occurs at the coupling junctions due to the interaction of the evanescent tail extending out of the ring waveguide with the bus waveguides. Loss due to absorption occurs in materials which absorb or scatter energy at the wavelength of interest. In Si material absorption at the 1550nm telecommunication wavelength is due primarily to impurities and two photon absorption.

Extrinsic Losses

In the add-drop microring resonator, the extraction of energy from the cavity via the input and output bus waveguides is called the extrinsic loss. Extrinsic loss depends only on the coupling coefficient κ of the microring.

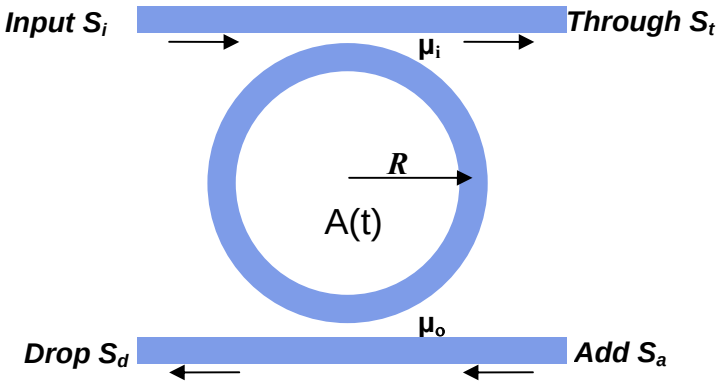

Figure 2.5. Schematic of an add-drop microring configuration for energy coupling analysis.

2.3 Energy coupling analysis

The spectral responses in equations 2.4 and 2.5 are derived based on power coupling analysis of the microring resonator. Another powerful approach for analyzing coupled microrings is the energy coupling analysis. This analysis is performed by assuming that the microring is a lumped element with time varying energy signal A(t), normalized such that $|A(t)|^2$ represents the energy stored in the resonator. If U(t) represents the power signal circulating inside the ring (normalized such that $|U(t)|^2$ represents the power flow), then the relationship between U(t) and A(t) in the add drop filter shown in Figure 2.5 is given by [47]

$$\left|U(t)\right|^2 = A(t)^2(\upsilon_g / 2\pi R) \tag{2.15}$$

where υ_g is the group velocity. The energy A(t) oscillates at the resonant frequency ω_0 and decays at a rate of γ with contributions from 3 factors:

- Energy lost due to intrinsic losses in the microring at the rate of

$$\gamma_L = \frac{\alpha \upsilon_g}{2} \tag{2.16}$$

where α is the power attenuation coefficient (m^{-1}).

- Energy lost at the input coupling junction at the rate of $\gamma_i = \mu_i^2 / 2$.
- Energy lost at the output coupling junction at the rate of $\gamma_o = \mu_o^2 / 2$.

The rate of change of energy inside the microring can be written as [47]

$$\frac{dA}{dt} = (j\omega_0 - \gamma_L - \gamma_i - \gamma_o)AS - j\mu_i S_i . \tag{2.17}$$

Introducing harmonic variation for the input signal and the energy signal inside the microring

$$A(t) \propto \exp(j\omega t) \text{ and}$$

$$S_i(t) \propto \exp(j\omega t),$$

equation 2.17 becomes

$$(j\Delta\omega + \gamma_L + \gamma_i + \gamma_o)A = -j\mu_i S_i, \tag{2.18}$$

where $\Delta\omega = \omega - \omega_0$ is the frequency detuning from the resonance. The drop and through port signals are given by

$$S_t = S_i - j\mu_i A \tag{2.19}$$

$$S_d = -j\mu_o A . \tag{2.20}$$

Using equations 2.18, 2.19 and 2.20 the transfer functions at the through and the drop ports are derived as

$$\frac{S_t}{S_i} = \frac{j\Delta\omega - \gamma_i + \gamma_o + \gamma_L}{j\Delta\omega + \gamma_i + \gamma_o + \gamma_L}, \tag{2.21}$$

$$\frac{S_d}{S_i} = \frac{-2\sqrt{\gamma_i \gamma_o}}{j\Delta\omega + \gamma_i + \gamma_o + \gamma_L} . \tag{2.22}$$

In the above expressions, the term $j\Delta\omega$ can be replaced by the frequency variable s in the Laplace domain. Thus the energy analysis naturally leads to the frequency response of the add-drop filter. This approach is very useful in modeling microring resonators with 3dB bandwidths much smaller than their FSRs. In such a narrowband approximation the microring can be modeled as a LC oscillator in the electrical domain. This would allow us to utilize well established Laplace domain based filter design techniques to synthesize microring filters for a variety of filter classes like Butterworth, Chebyshev, inverse Chebyshev and elliptic. In the later chapters, new microring filter architectures will be proposed and analyzed using the s-domain filter design techniques.

2.3.1 Equivalent circuit model of a microring resonator

The add-drop microring resonator is essentially a four port device. However if the back-scattering into the input and add ports are negligible then it can be modeled as a two port electrical network as shown in Figure 2.6. The signals V_{in}^{+}, V_{in}^{-}, V_{out}^{+}, and V_{out}^{-} are normalized voltage waves corresponding the input and output energy signals in Figure 2.5. The S-parameters of the two port network in Figure 2.6 could be related to the optical signals as

$$\frac{s_t}{s_i} = \frac{V_{in}^{-}}{V_{in}^{+}} = S_{11} \tag{2.23}$$

$$\frac{s_t}{s_a} = \frac{V_{in}^{-}}{V_{out}^{+}} = S_{12} \tag{2.24}$$

$$\frac{s_d}{s_i} = \frac{V_{out}^{-}}{V_{in}^{+}} = S_{21} \tag{2.25}$$

$$\frac{s_d}{s_a} = \frac{V_{out}^{-}}{V_{out}^{+}} = S_{22} \tag{2.26}$$

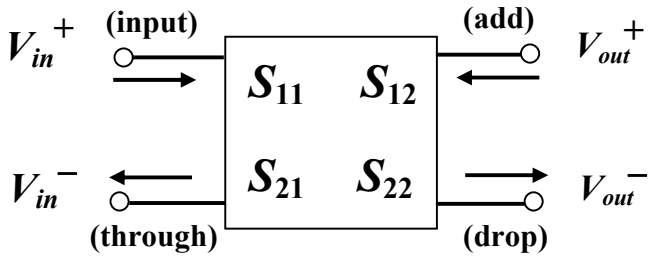

Figure 2.6. Two-port network representation of an add-drop microring filter.

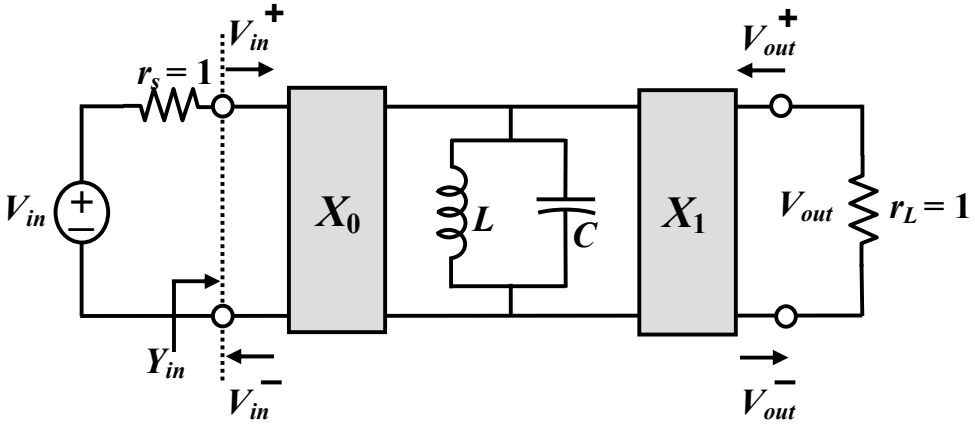

Figure 2.7. Equivalent bandpass circuit model of a single microring resonator.

In the narrowband approximation the microring resonator has a Lorentzian response at the resonance frequency. Thus it can be modeled as a simple first order LC oscillator circuit [48] as shown in Figure 2.7. Here the microring coupling junctions are modeled as capacitive voltage coupling elements X_0 and X_1 which also act as admittance inverters. The coupling elements can be related to the coupling coefficients by equating the microring spectral responses to the S-parameters of the equivalent circuit network. The S_{11} parameter of the given network can be determined from the input admittance Y_{in} of the circuit given by

$$Y_{in} = \frac{X_0^2}{Y_0 + X_1} \tag{2.27}$$

where Y_0 is the admittance of the shunt-LC resonator,

$$Y_0 = j\omega C + \frac{1}{j\omega L} = j\omega_0 C\left(\frac{\omega}{\omega_0} - \frac{\omega_0}{\omega}\right) \approx j\Delta\omega 2C \tag{2.28}$$

where $\Delta\omega = \omega - \omega_0 << \omega_0$ for narrow band approximation. From this the reflection parameter S_{11} is obtained as

$$S_{11} = \frac{V_{in}^-}{V_{in}^+} = \frac{1 - Y_{in}}{1 + Y_{in}} = \frac{j\Delta\omega - X_0^2/2C + X_1^2/2C}{j\Delta\omega + X_0^2/2C + X_1^2/2C}. \tag{2.29}$$

The transmission parameter S_{21} of the network can be obtained as

$$S_{21} = \frac{V_{out}^-}{V_{in}^+} = \frac{2V_{out}}{V_{in}} = \frac{-X_0 X_1/C}{j\Delta\omega + X_0^2/2C + X_1^2/2C}. \tag{2.30}$$

Consider the microring through and drop port equations 2.21 and 2.22 in the lossless scenario ($\gamma_L = 0$). Comparing equations 2.21 with 2.29 and 2.22 with 2.30, one can deduce the following relationships between the voltage coupling elements and the microring coupling coefficients

$$\mu_0 = X_0/\sqrt{C}, \tag{2.31}$$

$$\mu_1 = X_1/\sqrt{C}. \tag{2.32}$$

The LC equivalent circuit model developed above for the single microring resonator will be used as a building block for modeling high-order coupled microring resonator filters in the later chapters.

2.4 High-order microring resonator filters

In the previous sections we discussed the filter characteristics of a single microring resonator. In practical applications, the Lorentzian response of a single resonator is usually not sufficient to meet WDM filter requirements such as flat-top pass band, sharp

transition from pass band to stop band, high out-of-band extinction etc. Such filter characteristics usually require higher order transfer functions which can be realized by increasing the number of microring resonators. Borrowing well established filter design principles in microwave, standard filter shapes such as Butterworth, Chebyshev, elliptic and inverse Chebyshev can be achieved by appropriate design of the poles and zeros of the structure.

Simple filters have been already implemented in the optical domain using various arrangements of multiple microrings in different topologies. For e.g. the Butterworth and Chebyshev filters, which have only poles and no transmission zeros, can be realized by cascading microring resonators in a serial coupling topology as shown in Figure 2.8. Assuming all microrings to be synchronous, at the resonant wavelength the input optical signal S_i couples through the microrings from 1 to N and gets transmitted at the drop port (optical signal S_d). Appropriate choice of the inter-ring coupling coefficients can control the placement of poles which gives the necessary spectral shapes. The serial coupling topology is simple and easy to design as direct synthesis techniques are readily available in the literature [47, 48]. The serial coupling topology is also relatively easy to fabricate. Several serially coupled high-order microring filters have been demonstrated in various material systems such as semiconductors [49], polymer [50], SiN [33] and SOI [51, 52]. However, a disadvantage with the serial coupling topology is that only all-pole filters can be realized. To realize all-pole filters with box-like spectral responses with very sharp roll-off and high out-of-band rejection, the required filter order would be very high . If the number of microrings needed is in the order of several tens, then the fabrication would become unfeasibly complicated which is not desirable.

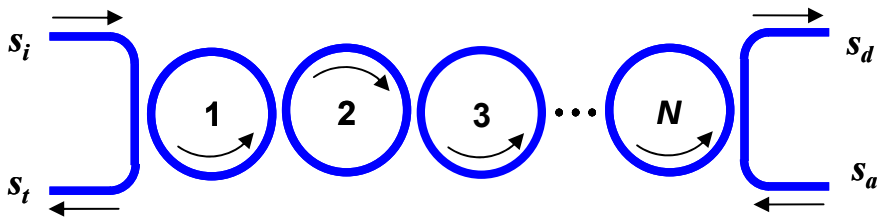

Figure 2.8. Schematic of a serially-coupled microring filter.

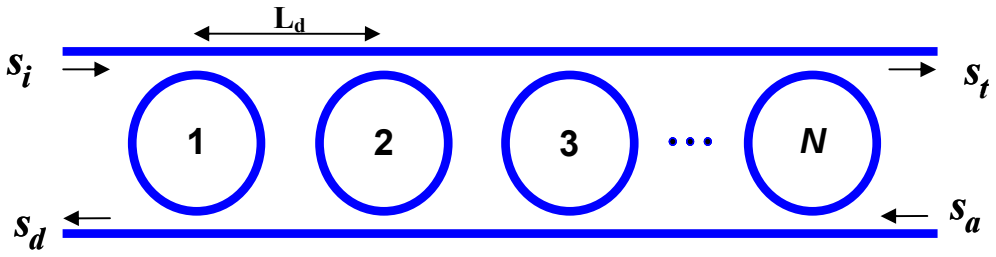

Figure 2.9. Schematic of parallel-cascaded microrings.

Filters which have transmission zeros in their transfer functions can have box like responses with very sharp roll-offs without requiring high filter orders. Examples are the elliptic and inverse Chebyshev types of filters. Two microring coupling configurations have been proposed in the literature that can realize filters with transmission zeros. The first topology is the parallel coupling topology [53, 54] whose schematic is shown in Figure 2.9. Here each microring is coupled only to the upper and lower bus waveguides and there is no direct coupling between the microrings. To avoid any inter microring coupling, each pair of microring is placed apart by a distance $L_d > 2R$. The parallel coupling configuration can be regarded as a distributed-feedback (DFB) grating where each microring acts as a reflection element in the grating. In this topology, box like spectral responses can be realized due to the presence of transmission zeros. However, only a few attempts have been made [55, 56] to realize this topology since 1) the poles of

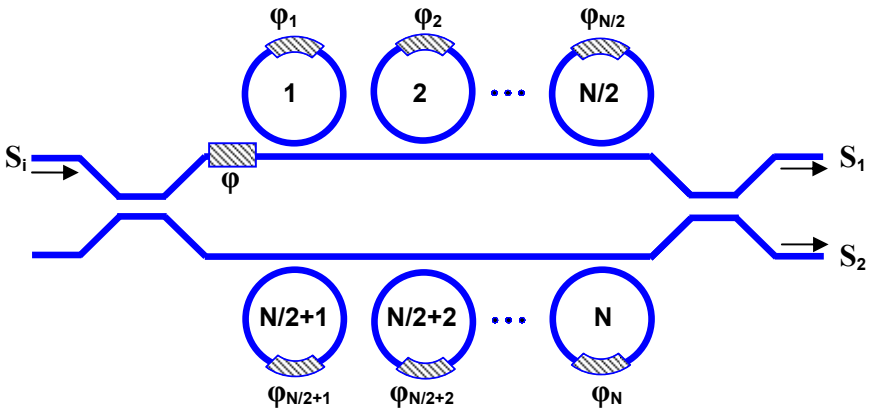

Figure 2.10. A MZI loaded with all-pass microrings.

the filter cannot be independently controlled and 2) there is no direct synthesis procedure available so that numerical optimization is required to design the filter.

The microring loaded Mach Zehnder Interferometer (MZI) configuration as shown in Figure 2.10 is the other microring topology that can realize optical filters with transmission zeros [57, 58]. The disadvantage of this architecture is that it requires asynchronous microring resonators, whose round trip phases φ_n have to be precisely controlled. Thus along with N+2 couplers, the device needs N+1 phase shifters to realize an N^{th} order filter. To date there is only one known demonstration of this filter architecture [59].

2.5 Summary

This chapter provided the background information on microring resonators and their characteristics as optical filters. The analysis of the single add-drop microring resonator using the energy coupling approach was presented and an equivalent circuit model was developed based on the energy coupling analysis. Various existing topologies for realizing complex higher order filters were reviewed and their advantages and disadvantages were highlighted. In chapters 3 and 4 we explore new coupled microring architectures for realizing advanced optical filter responses.

Chapter 3
Coupled-Microring Filters of General 2D Coupling Topology

In this chapter a new topology for realizing high order microring filters is introduced. This topology consists of direct-coupled asynchronous microring resonators arranged in a two-dimensional array. Such a 2D array of microrings can be considered as a generalized extension of 1D arrays of serially coupled microrings discussed in chapter 2. By allowing for coupling between non-adjacent microrings, high-order filter transfer functions with transmission zeros such as inverse Chebyshev or elliptic type can be realized. Also, the asynchronous microring resonators enable the realization of complex asymmetric filter shapes. The analysis of the 2D coupling topology is done using the energy coupling approach, from which the filter spectral response is derived. In order to synthesize the architecture for a given high order filter response, first an equivalent two-port circuit network is derived based on the *LC* circuit model of a single microring resonator developed in chapter 2. Using filter synthesis techniques available in the electrical domain, the equivalent electrical network is then synthesized to generate a coupling matrix corresponding to the desired filter. This coupling matrix is subsequently transformed into the physical coupling topology of the 2D coupled microring filter.

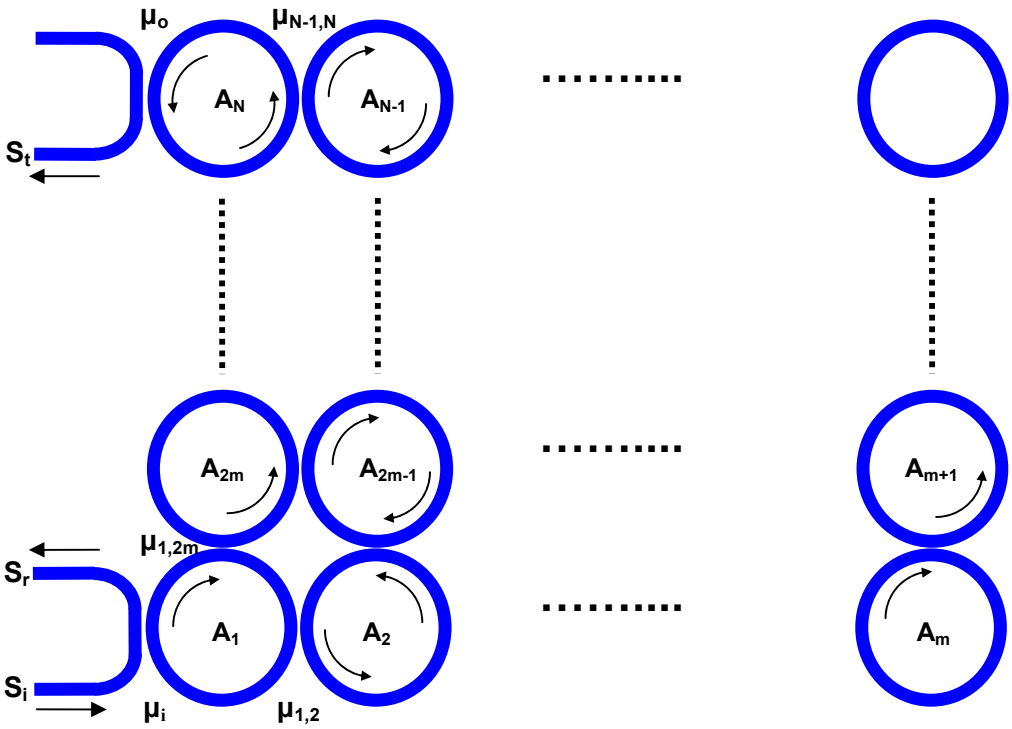

Figure 3.1. Schematic of a direct-coupled microring filter consisting of N resonators arranged in the most general coupling topology.

3.1 Energy coupling analysis of general 2D microring topology

Figure 3.1 shows the schematic of N asynchronous microring resonators arranged in the most general two-dimensional coupling topology. Microring 1 is coupled to the input waveguide via energy coupling coefficient μ_i while microring N is coupled to the output waveguide via energy coupling coefficient μ_o. Also every microring i is coupled to every other microring j in the network via energy coupling coefficient $\mu_{i,j}$. The signals s_i, s_r and s_t represent the input, reflected and transmitted optical signal amplitudes, respectively. Each microring i has resonant frequency ω_i which is detuned from the center frequency ω_0 of the filter passband given by

$$\Delta\omega_i = \omega_i - \omega_0 . \tag{3.1}$$

For practical filters, the detunings $\Delta\omega_i$ are usually small enough so that the microrings are approximately the same size and have the same intrinsic loss γ_L. As shown in Figure 3.1 the instantaneous energy amplitudes in the microrings are denoted by $A_i(t)$. In the energy coupling analysis, these energy amplitudes can be formulated into a system of coupled-mode equations given by [60],

$$\frac{dA_1}{dt} = (j\omega_1 - \tfrac{1}{2}\mu_i^2 - \gamma_L)A_1 - j\mu_{1,2}A_2 - j\mu_{1,3}A_3 - \ldots - j\mu_{1,N}A_N - j\mu_i s_i ,$$

$$\frac{dA_2}{dt} = -j\mu_{1,2}A_1 + (j\omega_2 - \gamma_L)A_2 - j\mu_{2,3}A_3 - j\mu_{2,4}A_4 - \ldots - j\mu_{2,N}A_N ,$$

$$\frac{dA_3}{dt} = -j\mu_{1,3}A_1 - j\mu_{2,3}A_2 + (j\omega_3 - \gamma_L)A_3 - j\mu_{3,4}A_4 - \ldots - j\mu_{3,N}A_N ,$$

$$\ldots$$

$$\frac{dA_N}{dt} = -j\mu_{1,N}A_1 - j\mu_{2,N}A_2 \ldots - j\mu_{N-1,N}A_{N-1} + (j\omega_N - \tfrac{1}{2}\mu_o^2 - \gamma_L)A_N . \qquad (3.2)$$

Introducing harmonic variation by letting $A_i, s_i \propto \exp(j\omega t)$, the above system of equations become

$$[(s - j\Delta\omega_1) + \tfrac{1}{2}\mu_i^2 + \gamma_L]A_1 + j\mu_{1,2}A_2 + j\mu_{1,3}A_3 + \ldots + j\mu_{1,N}A_N = -j\mu_i s_i ,$$

$$j\mu_{1,2}A_2 + [(s - j\Delta\omega_2) + \gamma_L]A_2 + j\mu_{2,3}A_3 + j\mu_{2,4}A_4 + \ldots + j\mu_{2,N}A_N = 0 ,$$

$$j\mu_{1,3}A_1 + j\mu_{2,3}A_2 + [(s - j\Delta\omega_3) + \gamma_L]A_3 + j\mu_{3,4}A_4 + \ldots + j\mu_{3,N}A_N = 0 ,$$

$$\ldots$$

$$j\mu_{1,N}A_1 + j\mu_{2,N}A_2 + \ldots + j\mu_{N-1,N}A_{N-1} + [(s - j\Delta\omega_N) + \tfrac{1}{2}\mu_o^2 + \gamma_L]A_N = 0 \qquad (3.3)$$

where $s = j(\omega - \omega_0)$ is the frequency variable and $s - j\Delta\omega_i = j(\omega - \omega_i)$. The above system of equations can be expressed in matrix form as,

$$(s\mathbf{I} + \mathbf{L} + j\mathbf{M})\mathbf{a} = \mathbf{b}, \tag{3.4}$$

where $\mathbf{I}$ is the $N \times N$ identity matrix,

$$\mathbf{a} = \left[A_1, A_2, \cdots, A_N\right]^T,$$

$$\mathbf{b} = \left[-j\mu_i s_i, 0, \cdots, 0\right]^T, \tag{3.5}$$

$\mathbf{M}$ is the symmetric energy coupling matrix having the general form

$$\mathbf{M} = \begin{bmatrix} \Delta\omega_1 & \mu_{1,2} & \mu_{1,3} & \cdots & \mu_{1,N} \\ \mu_{1,2} & \Delta\omega_2 & \mu_{2,3} & \cdots & \mu_{2,N} \\ \mu_{1,3} & \mu_{2,3} & \Delta\omega_3 & \cdots & \mu_{3,N} \\ \vdots & \vdots & \vdots & \ddots & \vdots \\ \mu_{1,N} & \mu_{2,N} & \mu_{3,N} & \cdots & \Delta\omega_N \end{bmatrix}, \tag{3.6}$$

and $\mathbf{L}$ is a diagonal matrix that represents the energy lost or coupled in and out of the system via the bus waveguides:

$$\mathbf{L} = \begin{bmatrix} \gamma_L + \mu_i^2/2 & & & & \\ & \gamma_L & & & \\ & & \ddots & & \\ & & & \gamma_L & \\ & & & & \gamma_L + \mu_o^2/2 \end{bmatrix} \tag{3.7}$$

The loss matrix $\mathbf{L}$ can also be written as:

$$\mathbf{L} = \gamma_L \mathbf{I} + \mathbf{L}_{ex} \tag{3.8}$$

where $\mathbf{L}_{ex}$ is the external loss matrix

$$\mathbf{L}_{ex} = \begin{bmatrix} \mu_i^2/2 & & & & \\ & 0 & & & \\ & & \ddots & & \\ & & & 0 & \\ & & & & \mu_o^2/2 \end{bmatrix} . \tag{3.9}$$

Substituting equation 3.8 into equation 3.4 we get

$$[(s+\gamma_L)\mathbf{I} + \mathbf{L}_{ex} + j\mathbf{M})\mathbf{a} = \mathbf{b} . \tag{3.10}$$

Equation 3.10 can be solved by diagonalizing the matrix ($\mathbf{L}_{ex} + j\mathbf{M}$) in the form,

$$\mathbf{L}_{ex} + j\mathbf{M} = \mathbf{Q} \cdot \mathbf{D} \cdot \mathbf{Q}^{-1}, \tag{3.11}$$

where **D** is the diagonal matrix containing the eigenvalues of ($\mathbf{L}_{ex} + j\mathbf{M}$) and **Q** is the corresponding eigenvector matrix. Substituting equation 3.11 into 3.10 and solving for **a** we get

$$\mathbf{a} = \mathbf{Q}[(s+\gamma_L)\mathbf{I} + \mathbf{D}]^{-1}\mathbf{Q}^{-1}\mathbf{b} . \tag{3.12}$$

Each element of **a** can be expressed as

$$A_n = -j\mu_i s_i \sum_{k=1}^{N} \frac{Q_{n,k} Q_{k,1}^{-1}}{s + \gamma_L + jd_k}, \text{ n = 1 to N.} \tag{3.13}$$

Here d_k is the kth diagonal element of **D** which is also related to the pole p_k of the filter transfer function with no loss ($\gamma_L = 0$) as

$$p_k = -jd_k . \tag{3.14}$$

From the relationships $s_r = s_i - j\mu_i a_1$ and $s_t = -j\mu_o a_N$, the reflected and transmitted spectral responses of the microring filter at the through port and drop port can be obtained as

$$\frac{s_r}{s_i} = 1 - \mu_i^2 \sum_{k=1}^{N} \frac{Q_{1,k} Q_{k,1}^{-1}}{s + \gamma_L + jd_k}, \tag{3.15}$$

$$\frac{s_t}{s_i} = -\mu_i \mu_o \sum_{k=1}^{N} \frac{Q_{N,k} Q_{k,1}^{-1}}{s + \gamma_L + jd_k}. \tag{3.16}$$

Equations 3.15 and 3.16 are the closed-form expressions of the 2D direct coupled microring system. From the equations it can be noted that loss in the system causes the filter poles to shift by a constant amount γ_L to the left in the s-plane. In general the effect of loss in microrings is to cause rounding of the passband edges and increase the group delay dispersion. If prior knowledge of the microring loss γ_L is available, one could compensate for the effect of loss using a technique called predistortion. In this technique the filter transfer function is predistorted by shifting the poles and zeros to the right by an amount equal to γ_L [61] to compensate for loss in the microrings. When loss is present, the poles and zeros are moved back to their desired locations and the desired filter characteristics are recovered in both the amplitude and group delay responses.

3.2 Equivalent circuit model

For a given filter transfer function, a 2D microring coupling topology having the desired filter response can be constructed by determining the energy coupling matrix **M** of the network (equation 3.6). This can be accomplished by first constructing an equivalent circuit network model of the topology and then generating the coupling matrix **X** of the electrical network using well known electrical filter synthesis techniques. The coupling matrix **X** can then be correlated to the energy coupling matrix **M** of the microring filter. In chapter 2 it was shown that a single lossless microring resonator along with its coupling junctions could be modeled as a simple shunt LC oscillator with capacitive coupling elements. Using this model as a building block, the 2D coupled microring topology with no loss ($\gamma_L = 0$) can be modeled by the electrical network shown in Figure 3.2.

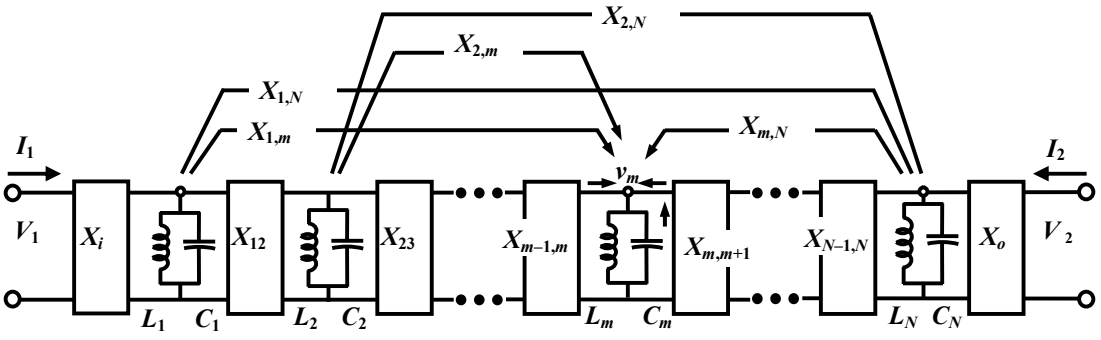

Figure 3.2. Schematic of the equivalent electrical network model of the 2D direct-coupled microring topology consisting of *N* resonators.

Here each asynchronously tuned microring *m* with resonant frequency ω_m is modeled as a LC oscillator with $L_m C_m = (\omega_m)^{-2}$. X_i, X_o and $X_{i,j}$ are the capacitive or susceptance coupling elements representing the input coupling, output coupling and mutual coupling between microrings *i* and *j* respectively. We consider the case of a lowpass prototype filter circuit with center frequency ω_0 = 0 rad/s and cut-off frequency ω_c = 1 rad/s. Similar to equation 2.28, each microring *m* with resonance frequency ω_m can be represented by the LC shunt oscillator admittance $\boldsymbol{Y_m}$,

$$Y_m = j\omega C_m + \frac{1}{j\omega L_m} \approx j(\omega - \omega_m)2C_m . \tag{3.17}$$

For practical band pass filters the frequency detuning $\Delta\omega_m = \omega_m - \omega_0$ of microring *m* with respect to the center frequency ω_0 is usually small, which implies that $C_m \approx C_0$ and, by choosing C_0 = 1/2 farads, we can express equation 3.17 as

$$Y_m \approx j(\omega - \omega_m) \approx j(\omega - \omega_0) - j(\omega_m - \omega_0) = s - j\Delta\omega_m \tag{3.18}$$

where $s = j(\omega - \omega_0)$ is the bandpass frequency variable.

Let v_m be the voltage at each node *m* = 1 to *N* in the electrical network in Figure 3.2. Using Kirchoff's current law (KCL), the sum of the currents flowing in and out of each node *m* is given by

Node 1: $jX_i V_1 - (s - j\Delta\omega_1)v_1 + jX_{1,2}v_2 + jX_{1,3}v_3 + \cdots + jX_{1,N}v_N = 0$,

Node 2: $jX_{1,2}v_1 - (s - j\Delta\omega_2)v_2 + jX_{2,3}v_3 + jX_{2,4}v_4 \cdots + jX_{2,N}v_N = 0$,

...

Node N: $jX_{1,N}v_1 + jX_{2,N}v_2 + \cdots + jX_{N-1,N}v_N - (s - j\Delta\omega_N)v_N = 0$. (3.19)

Applying KCL at the input and output port gives the relationships $jX_i v_1 + I_1 = 0$ and $jX_o v_N + I_2 = 0$, respectively, from which we obtain $v_1 = -I_1 / jX_i$ and $v_N = -I_2 / jX_o$. Substitute these expressions for v_1 and v_N in equation 3.19 to form the matrix equation:

$$(\mathbf{sI} - j\mathbf{X})\mathbf{V} = \mathbf{J}, \tag{3.20}$$

where **X** is the *N*x*N* susceptance coupling matrix which also contains the frequency detunings as diagonal elements

$$\mathbf{X} = \begin{bmatrix} \Delta\omega_1 & X_{1,2} & X_{1,3} & \cdots & X_{1,N} \\ X_{1,2} & \Delta\omega_2 & X_{2,3} & \cdots & X_{2,N} \\ X_{1,3} & X_{2,3} & \Delta\omega_3 & \cdots & X_{3,N} \\ \vdots & \vdots & \vdots & \ddots & \vdots \\ X_{1,N} & X_{2,N} & X_{3,N} & \cdots & \Delta\omega_N \end{bmatrix}, \tag{3.21}$$

V and **J** are the *N*x1 voltage and current arrays respectively

$$\mathrm{V} = \begin{bmatrix} -I_1 / jX_i \\ v_2 \\ v_3 \\ \cdots \\ v_{N-1} \\ -I_2 / jX_o \end{bmatrix}, \qquad \mathrm{J} = \begin{bmatrix} jX_i V_1 \\ 0 \\ 0 \\ \cdots \\ 0 \\ jX_o V_2 \end{bmatrix}. \tag{3.22}$$

The values of the susceptance coupling elements are related to the microrings energy coupling coefficients as given in [60]

$$\mu_{i,j} = X_{i,j},$$

$$\mu_i = X_i\sqrt{2},$$

$$\mu_o = X_o\sqrt{2}. \tag{3.23}$$

Equation 3.20 describes the equivalent circuit network of the 2D coupled microring topology. In the synthesis of the 2D microring network, we can apply microwave filter techniques [62 - 65] to the equivalent circuit.

3.3 Synthesis of the equivalent circuit network

A popular method for synthesizing the equivalent circuit network is the coupling matrix method [63]. Since **X** is a real and symmetric matrix, it can be diagonalized in the form

$$\mathbf{X} = \mathbf{T} \cdot \mathbf{\Lambda} \cdot \mathbf{T}^t, \tag{3.24}$$

where **T** is an orthonormal matrix and the diagonal matrix **Λ** contains the eigenvalues λ_k of **X**. Substituting (3.24) into (3.20) and solving for **V**, we get

$$\mathbf{V} = \mathbf{T} \cdot (\mathbf{sI} - j\,\mathbf{\Lambda})^{-1} \cdot \mathbf{T}^t\,\mathbf{J} = \mathbf{Z}\,\mathbf{J}. \tag{3.25}$$

Here $\mathbf{Z} = \mathbf{T} \cdot (s\mathbf{I} - j\mathbf{\Lambda})^{-1} \cdot \mathbf{T}^t$ is an $N \times N$ impedance matrix of the circuit network whose element $Z_{i,j}$ is given by

$$Z_{i,j} = \sum_{k=1}^{N} \frac{T_{i,k}T_{j,k}}{s - j\lambda_k}. \tag{3.26}$$

From the impedance matrix **Z,** the two-port short-circuit admittance matrix $\mathbf{Y}_{sc}$ of the network can be extracted to give [63],

$$\mathbf{Y}_{sc} = \begin{bmatrix} y_{11} & y_{12} \\ y_{21} & y_{22} \end{bmatrix} = \begin{bmatrix} X_i^2 Z_{1,1} & X_i X_o Z_{1,N} \\ X_i X_o Z_{N,1} & X_o^2 Z_{N,N} \end{bmatrix} = \sum_{k=1}^{N} \frac{1}{s - j\lambda_k} \begin{bmatrix} X_i^2 T_{1,k}^2 & X_i X_o T_{1,k} T_{N,k} \\ X_i X_o T_{N,k} T_{1,k} & X_o^2 T_{N,k}^2 \end{bmatrix}. \tag{3.27}$$

It is noted from the above equation that the eigenvalues λ_k are also the poles of the short circuit admittance parameters of the network. In general, for a N-th order filter, the short-circuit admittance matrix can be expressed in the form [66]

$$\mathbf{Y}_{sc} = \sum_{k=1}^{N} \frac{1}{s - p_k} \begin{bmatrix} \xi_{11}^{(k)} & \xi_{12}^{(k)} \\ \xi_{21}^{(k)} & \xi_{22}^{(k)} \end{bmatrix}, \tag{3.28}$$

where p_k is the k^{th} pole of the admittance parameters and $\xi_{i,j}^{(k)}$ is the residue of admittance $y_{i,j}$ at the pole p_k. Comparing equations 3.27 and 3.28 shows that $p_k = j\lambda_k$, which forms the diagonal of the eigenvalue matrix $\mathbf{\Lambda}$ in equation 3.24. In the next section we show how the short circuit admittance parameters, specifically their poles and residues, can be obtained from the optical transfer function of the microring network to be synthesized.

3.3.1 Determination of the short circuit admittance matrix $\mathbf{Y_{sc}}$

From equation 3.16 we can express the transmission response of a 2D coupled microring filter in the general form:

$$S_t(s) = \frac{\prod_{k=1}^{M} (s - z_k)}{\prod_{k=1}^{N} (s - p_k)} = \frac{P(s)}{Q(s)}, \tag{3.29}$$

where p_k and z_k are the poles and zeroes of the filter respectively, N is the number of poles and $M \leq N$-2 is the number of zeros. The above transmission response can have symmetric or asymmetric shape with respect to the center frequency. For asymmetric spectral shapes p_k and z_k appear as unpaired complex numbers whereas for symmetric spectral shapes they appear in complex conjugate pairs. Given a target filter response of

the form in equation 3.29 we can obtain the reflection response of the filter from the energy conservation for a lossless network:

$$\left|S_r(s)\right|^2 + \left|S_t(s)\right|^2 = 1. \tag{3.30}$$

Letting $S_r(s) = R(s)/Q(s)$, where $R(s)$ is an N^{th}-degree polynomial, the above equation gives

$$\left|P(s)\right|^2 + \left|R(s)\right|^2 = \left|Q(s)\right|^2, \tag{3.31}$$

or

$$R(s)R(-s) = Q(s)Q(-s) - P(s)P(-s). \tag{3.32}$$

To determine the polynomial $R(s)$, the roots of the polynomial on the right side of equation 3.32 are first obtained, which can be divided into two sets of values that are the negative of each other. The polynomial $R(s)$ can be formed from either set of the roots. We can see that the choice of the roots of $R(s)$ is not unique, so that more than one filter design is possible for a given transfer function.

The input impedance Z_{in} of the electrical network is obtained from the reflection response $S_r(s)$ as

$$Z_{in}(s) = \frac{1 + S_r(s)}{1 - S_r(s)} = \frac{Q(s) + R(s)}{Q(s) - R(s)}. \tag{3.33}$$

Let the polynomials $P(s)$, $Q(s)$ and $R(s)$ be expressed in terms of their complex coefficients a_k, b_k and c_k as

$$\begin{aligned} Q(s) &= \sum_{k=0}^{N} a_k s^k, \\ P(s) &= \sum_{k=0}^{N-2} b_k s^k, \\ R(s) &= \sum_{k=0}^{N} c_k s^k. \end{aligned} \tag{3.34}$$

Using the above expressions, the input impedance in 3.33 can then be expressed as

$$Z_{in}(s) = \frac{m(s) + n(s)}{Q(s) - R(s)}, \tag{3.35}$$

where $m(s)$ and $n(s)$ are the complex-odd and complex-even polynomials constructed from the coefficients a_k and c_k of $Q(s)$ and $R(s)$, respectively, as given below

$$m(s) = \mathrm{Re}\{a_0 + c_0\} + j\,\mathrm{Im}\{a_1 + c_1\}s + \mathrm{Re}\{a_2 + c_2\}s^2 + j\,\mathrm{Im}\{a_3 + c_3\}s^3 + \ldots,$$

$$n(s) = j\,\mathrm{Im}\{a_0 + c_0\} + \mathrm{Re}\{a_1 + c_1\}s + j\,\mathrm{Im}\{a_2 + c_2\}s^2 + \mathrm{Re}\{a_3 + c_3\}s^3 + \ldots \tag{3.36}$$

As shown in [64], the elements of the short circuit admittance matrix $\mathbf{Y_{sc}}$ can then be obtained as

$$y_{11}(s) = y_{22}(s) = \begin{cases} n(s)/m(s), & \text{if } N \text{ is even,} \\ m(s)/n(s), & \text{if } N \text{ is odd,} \end{cases} \tag{3.37}$$

$$y_{12}(s) = y_{21}(s) = \begin{cases} P(s)/m(s), & \text{if } N \text{ is even,} \\ P(s)/n(s), & \text{if } N \text{ is odd.} \end{cases} \tag{3.38}$$

By expressing y_{11}(s) and y_{12}(s) in partial fraction expansion as in equation 3.28, the poles λ_k and residues $\xi_{11}^{(k)} = \xi_{22}^{(k)}$ and $\xi_{12}^{(k)} = \xi_{21}^{(k)}$ can be obtained.

3.3.2 Determination of the coupling matrix

The coupling matrix X can be determined once the eigenmatrix Λ and the orthonormal matrix T in equation 3.24 are known. The matrix Λ is constructed from the poles of the admittance parameters. The matrix T can be constructed as follows. First, by summing over the admittance residues $\xi_{11}^{(k)}$ and $\xi_{22}^{(k)}$, the input and output coupling coefficients μ_i and μ_o are obtained [63] as

$$\sum_{k=1}^{N} \xi_{11}^{(k)} = \sum_{k=1}^{N} X_i^2 T_{1,k}^2 = X_i^2 \sum_{k=1}^{N} T_{1,k}^2 = X_i^2 = \mu_i^2 / 2, \tag{3.39}$$

$$\sum_{k=1}^{N} \xi_{22}^{(k)} = \sum_{k=1}^{N} X_o^2 T_{N,k}^2 = X_o^2 \sum_{k=1}^{N} T_{N,k}^2 = X_o^2 = \mu_o^2/2 . \tag{3.40}$$

In the above expressions we have used the results $\sum_{k=1}^{N} T_{1,k}^2 = \sum_{k=1}^{N} T_{N,k}^2 = 1$ since matrix **T** is orthonormal. Comparing equations 3.27 and 3.28, the elements in the first and last rows of the matrix **T** can be determined as

$$T_{1,k} = \frac{\sqrt{\xi_{11}^{(k)}}}{X_i} \tag{3.41}$$

$$T_{N,k} = T_{1,k} \operatorname{sgn}\left\{ \operatorname{imag}\left\{ \xi_{12}^{(k)} \right\} \right\}. \tag{3.42}$$

The orthonormal nature of matrix **T** allows us to determine the remaining rows by a procedure called Gram-Schmidt orthogonalization.

Once matrix **T** is generated and with the knowledge of matrix **Λ,** the coupling matrix **X** can be determined from $\mathbf{X} = \mathbf{T} \cdot \mathbf{\Lambda} \cdot \mathbf{T}^t$. The energy coupling matrix **M** of the microring filter is equal to the coupling matrix **X** of the electrical network**,** since $X_{i,j} = \mu_{i,j}$ as per equation 3.23. The energy coupling coefficients determined above are those of the prototype filter with center frequency $\omega_0 = 0$ rad/s and cut-off frequency $\omega_c = 1$ rad/s. To transform it to a bandpass filter with bandwidth *B,* frequency scaling is applied to get [60],

$$\tilde{\mu}_i = \mu_i \sqrt{B/2} ,$$

$$\tilde{\mu}_o = \mu_o \sqrt{B/2} ,$$

$$\tilde{\mu}_{i,j} = \mu_{i,j} (B/2) . \tag{3.43}$$

Finally the energy coupling coefficients (μ) can be related to the field coupling coefficients (κ) as:

$$\kappa_{i,j} = \frac{\mu_{i,j}}{\sqrt{FSR_i FSR_j}},$$

$$\kappa_i = \frac{\mu_i}{\sqrt{FSR_1}},$$

$$\kappa_o = \frac{\mu_o}{\sqrt{FSR_N}}. \qquad (3.44)$$

where FSR_i and FSR_j are the FSRs of microring i and j respectively.

3.3.3 Optimization of the coupling matrix

The coupling matrix **M** obtained using the above procedure is not the only unique solution for a given filter transfer function. Many times **M** could correspond to a coupling topology where a microring is required to couple to too many other microrings. Such a topology may not be a practical realization of the filter due to layout constraints. Another coupling topology that could lead to a potential problem is a microring triplet formation as shown in Figure 3.3(a). In general, a circular loop formation by an odd number of microring resonators as shown in Figure 3.3(b) is an undesirable coupling topology. Since the microrings are travelling wave resonators, these circular loop structures would lead to coupling between the clockwise and counter-clockwise

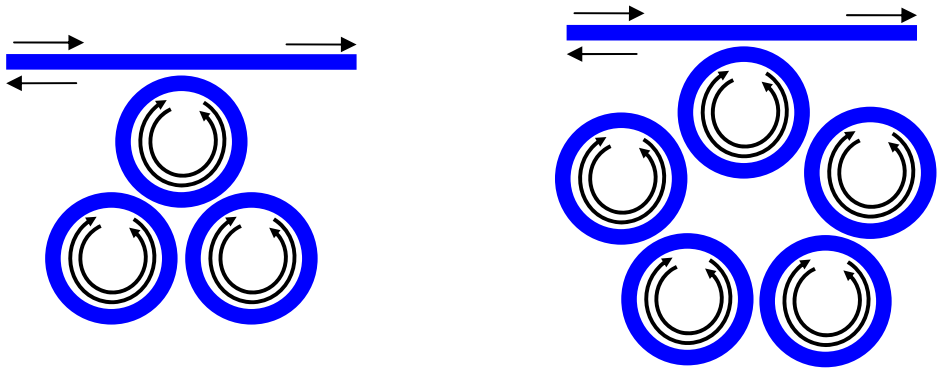

(a) (b)

Figure 3.3. Examples of microring topologies which lead to coupling between counter-propagation waves: (a) a triplet configuration; (b) an odd number of microring resonators arranged in a circular loop.

propagating modes in the microrings, resulting in a reflected signal at the input port which is not desirable.

To convert a non-realizable coupling matrix **M** into a realizable one, one could apply similarity transformations such as Jacobi rotations to the original matrix **M** to transform it into a new coupling matrix. Such a transformation would preserve the original eigenvalues of **M** so that the filter response is unchanged [63]. During each Jacobi rotation performed on **M**, a new coupling matrix **M′** is obtained as given by

$$\mathbf{M}' = \mathbf{R}(\theta_r) \cdot \mathbf{M} \cdot \mathbf{R}^t(\theta_r), \tag{3.45}$$

where $\mathbf{R}(\theta_r)$ is an $N \times N$ Jacobi rotation matrix and θ_r is the rotation angle which is specifically chosen to annihilate an unrealizable coupling element in the original coupling matrix **M**. By applying a sequence of such rotations as described in [64, 65], a new practically realizable coupling matrix **M** can be obtained. As mentioned before there are many possible coupling topologies (i.e. matrices) synthesizable for a single filter transfer function. Out of all possible coupling topologies for a given spectral response, an optimum device topology in terms of ease of fabrication would be the one which has a minimum number of coupling elements. Given a spectral response, one can apply successive matrix rotations to annihilate undesired coupling elements and minimize the number of coupling elements.

Also it is well-known that a direct-coupled cavity filter with transmission zeros on the imaginary frequency axis will require negative coupling elements. One way to realize negative coupling elements in microring resonators is to use racetracks with long straight waveguide sections for coupling. Since the evanescent power coupling between two adjacent waveguides is $\kappa = \sin(\kappa_c L_{coup})$ where κ_c is the power coupling per unit length, a negative coupling element will require a coupling length L_{coup} such that $3\pi/2 < \kappa_c L_{coup} < 2\pi$. Since it is generally more difficult to realize negative coupling elements than positive coupling elements, it is desirable to minimize the number of negative elements in the coupling matrix **M**. This can be achieved by applying a series of reflection operations to invert the signs of the rows and columns of the matrix.

3.4 Numerical filter design examples

In this section several numerical examples are presented to illustrate the application of the coupling matrix technique to synthesize and optimize filters based on 2D direct-coupled microrings. The first example shows a sixth-order symmetric elliptic filter with two transmission zeros with various optimized structures to minimize the number of negative couplings. The second example is a seventh-order asymmetric filter to illustrate the synthesis of microring filters with unpaired complex transmission zeros in the transfer function. The third example illustrates an advanced application of the 2D microring coupling topology with the design of a linear phase filter with flat-top spectral responses in both the amplitude and group delay. The fourth example demonstrates the use of predistortion technique discussed in section 3.1 to recover a sixth-order elliptic filter response in the presence of loss.

3.4.1 A sixth-order symmetric elliptic filter

This example illustrates the synthesis and optimization procedure of a 6th order elliptic filter with two transmission zeros. The filter specifications include:

- 25 GHz bandwidth,
- 0.05-dB passband ripple,
- 30-dB rejection level in the stopband.

Using an appropriate filter approximation method [64], we obtain the following transfer functions of the prototype filter which satisfy the above specifications:

$$S_t(s) = \frac{s^2 + 1.651225}{[s^6 + 1.7985s^5 + 3.289s^4 + 3.305s^3 + 2.6776s^2 + 1.3528s + 0.392]}, \tag{3.46}$$

$$S_r(s) = \frac{s^6 + 1.6716s^4 + 7452s^2 + 0.0589}{[s^6 + 1.7985s^5 + 3.289s^4 + 3.305s^3 + 2.6776s^2 + 1.3528s + 0.392]}. \tag{3.47}$$

The transmission transfer function has 6 poles located at -0.078±j1.062 , -0.301±j 0.884, -0.517±j 0.357 and 2 zeros located at ±j1.285 in the complex s-plane. In the synthesis procedure, we first determine the input impedance Z_{in} of the equivalent network from

equation 3.35. Using Z_{in} and equations 3.37 and 3.38 the short-circuit admittance matrix elements $y_{11} = y_{22}$ and $y_{21} = y_{12}$ can be determined. The computed poles and residues of the resulting short-circuit admittance matrix $\boldsymbol{Y}_{sc}$ are listed in Table 3.1. From the residues ξ_{11} and ξ_{22}, we calculate the input and output coupling elements X_i and X_o to be 0.9483 based on equations 3.39 and 3.40. Using equations 3.41 and 3.42 the first and the final rows of the **T** matrix can be calculated. The remaining rows of **T** are obtained using Gram-Schmidt orthogonalization procedure. The resulting matrix **T** is:

$$\mathbf{T} = \begin{bmatrix} 0.2692 & 0.2692 & 0.4263 & 0.4263 & 0.4957 & 0.4957 \\ 0 & 0.9247 & -0.2483 & 0 & 0 & -0.2887 \\ 0 & 0 & 0.7582 & 0 & 0 & -0.6520 \\ -0.2878 & 0 & 0 & 0.7978 & -0.5298 & 0 \\ -0.8788 & 0 & 0 & 0 & 0.4773 & 0 \\ -0.2692 & 0.2692 & 0.4263 & -0.4263 & -0.4957 & 0.4957 \end{bmatrix} \tag{3.48}$$

From the poles of y_{11} in Table 3.1, the diagonal matrix $\boldsymbol{\Lambda}$ in equation 3.24 is obtained as

$$\Lambda = \begin{bmatrix} 1.1336 & 0 & 0 & 0 & 0 & 0 \\ 0 & -1.1336 & 0 & 0 & 0 & 0 \\ 0 & 0 & 1.0120 & 0 & 0 & 0 \\ 0 & 0 & 0 & -1.0120 & 0 & 0 \\ 0 & 0 & 0 & 0 & 0.4140 & 0 \\ 0 & 0 & 0 & 0 & 0 & -0.4140 \end{bmatrix} \tag{3.49}$$

Poles of y_{11} and y_{12}	$\xi_{11} = \xi_{22}$	$\xi_{12} = \xi_{21}$
j 1.1336	0.0652	j 0.2777
$-j$ 1.1336	0. 0652	$-j$ 0.2777
j 1.0120	0. 1635	j 0.6962
$-j$ 1.0120	0. 1635	$-j$ 0. 6962
j 0.4140	0.2210	j 0.9413
$-j$ 0. 4140	0.2210	$-j$ 0. 9413

Table 3.1. Poles and residues of the short-circuit admittances of the 6th-order elliptic filter.

With matrices **T** and **Λ** known, the coupling matrix $X = M = \mathbf{T} \cdot \mathbf{\Lambda} \cdot \mathbf{T}^t$ can be obtained as:

$$M = \begin{bmatrix} 0 & -0.3301 & 0.4609 & -0.5407 & -0.1703 & 0 \\ & -0.9414 & -0.2684 & 0 & 0 & -0.3301 \\ & & 0.4056 & 0 & 0 & -0.4609 \\ & & & -0.4339 & 0.1820 & 0.5407 \\ & & & & 0.9697 & 0.1703 \\ & & & & & 0 \end{bmatrix} \tag{3.50}$$

Equation 3.50 shows only the upper half of the matrix since **M** is symmetric. It can be seen that the synthesized coupling matrix requires each microring to be coupled with several other microrings which is not physically realizable. In order to reduce the number of coupling elements to obtain a realizable coupling matrix, Jacobian rotations are applied to reduce the matrix into a simpler matrix $\mathbf{M_1}$

$$\mathbf{M}_1 = \begin{bmatrix} 0 & 0.8017 & 0 & 0 & 0 & 0 \\ & 0 & 0.5512 & 0 & 0.2031 & 0 \\ & & 0 & 0.7338 & 0 & 0 \\ & & & 0 & -0.5512 & 0 \\ & & & & 0 & 0.8017 \\ & & & & & 0 \end{bmatrix}. \tag{3.51}$$

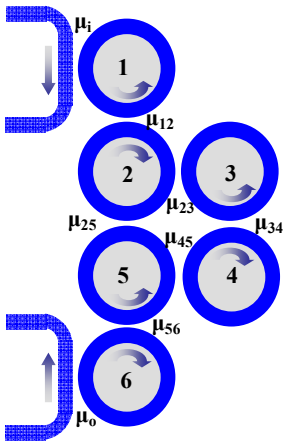

Figure 3.4. Folded coupling topology of a 6th-order elliptic microring filter with coupling matrix given by equation 3.51.

The above matrix has only 6 non-zero coupling elements whose coupling topology is shown in Figure 3.4. Also the number of negative couplings in the original matrix (equation 3.50) has been reduced to one, which is significant since it is difficult to realize negative coupling elements. By performing further similarity transformations on $\mathbf{M_1}$, alternative coupling topologies that could provide new layout possibilities can be obtained. One such topology with a new layout and a minimum number of negative couplings is shown in figure 3.5 whose coupling matrix $\mathbf{M_2}$ is given by:

$$\mathbf{M}_2 = \begin{bmatrix} 0 & 0.8017 & 0 & 0 & 0 & 0 \\ & 0 & 0 & 0 & 0.5874 & 0 \\ & & 0 & 0.7727 & 0 & -0.7523 \\ & & & 0 & 0.5027 & 0 \\ & & & & 0 & 0.2772 \\ & & & & & 0 \end{bmatrix} \tag{3.52}$$

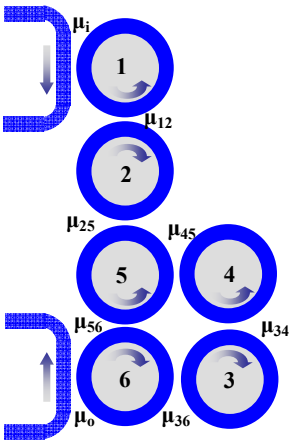

Figure 3.5. Alternative coupling topology of the 6th-order elliptic microring filter with coupling matrix given by equation 3.52.

The matrix $\mathbf{M_1}$ in equation 3.51 is for the prototype filter with a bandwidth of 1 rad/s. After scaling to the 25 GHz bandwidth using equation 3.43, we obtain $\tilde{\mu}_i = \tilde{\mu}_o = 11.88$

$$\tilde{\mathbf{M}} = \begin{bmatrix} 0 & 62.97 & 0 & 0 & 0 & 0 \\ & 0 & 43.29 & 0 & 15.94 & 0 \\ & & 0 & 58.03 & 0 & 0 \\ & & & 0 & -43.29 & 0 \\ & & & & 0 & 0.62.97 \\ & & & & & 0 \end{bmatrix}. \tag{3.53}$$

Using equations 3.15 and 3.16, the transmission response (solid gray) and reflection response (dashed gray) of the 25 GHz bandpass filter are computed and plotted in Figure 3.6. The black dots represent the plots of the target filter responses

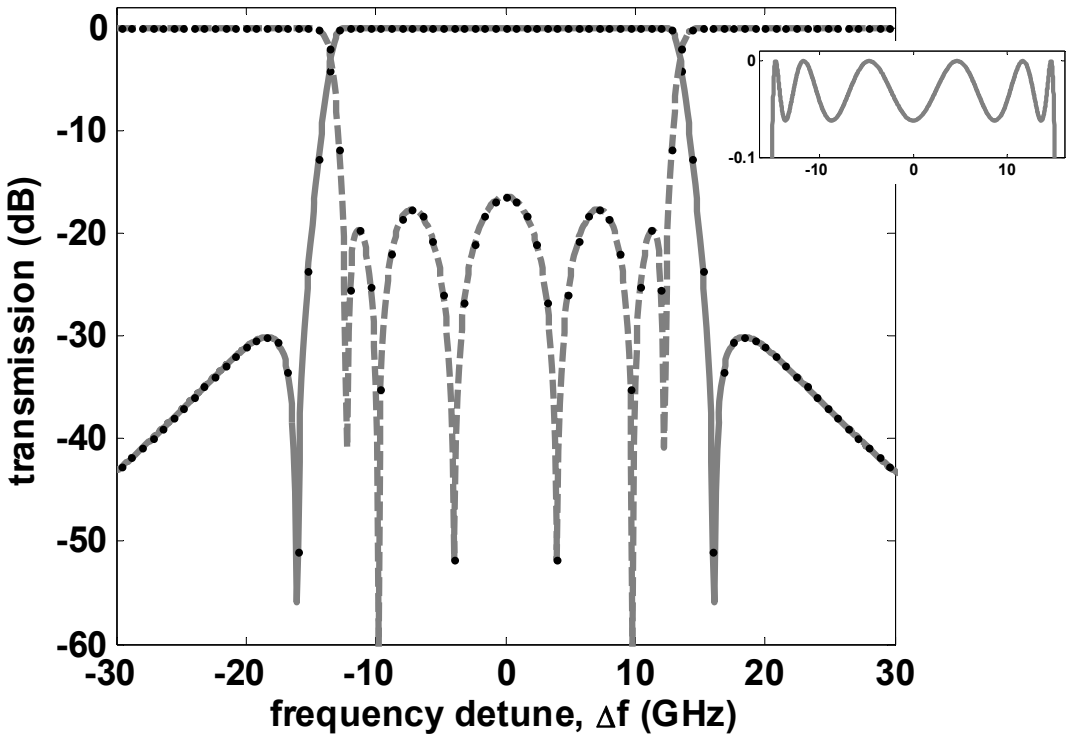

Figure 3.6. Synthesized transmission response (solid gray line) and reflection response (dashed gray line) of a 6th-order 25GHz-bandwidth elliptic filter. The dots represent the target filter responses. The inset shows a close-up view of the passband.

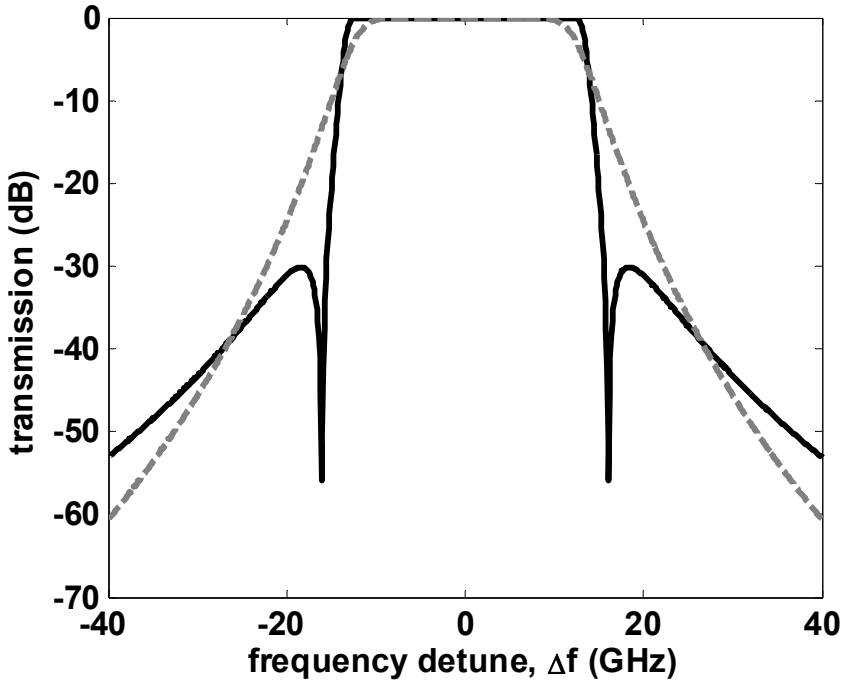

Figure 3.7. Synthesized transmission response of a 6th-order 25GHz-bandwidth elliptic filter (solid black line) along with a transmission response of 6th order Butterworth filter (dashed gray line).

which are in good agreement with the synthesized filter responses. In Figure 3.7 the transmission response of the elliptic filter (solid black line) is compared to that of a 6th order 25 GHz Butterworth filter (dashed gray line). The Butterworth filter can be realized with six serially coupled microring resonators as shown in Figure 2.8. It can be seen that in terms of adjacent channel isolation and band transition (roll off characteristic) the elliptic filter offers a better performance.

3.4.2 A seventh order asymmetric elliptic filter

This example considers the design of a 25 GHz bandwidth asymmetric 7th order microring filter with 3 transmission zeros. The filter is designed to have two zeros to be positioned close to the right band edge (on the high-frequency side of the passband) to achieve a very steep roll-off and an out-of-band rejection level of −55dB. The third transmission zero is placed on the left-hand side (low frequency side) of the passband to achieve a minimum out-of-band rejection of −65dB. The poles and zeros of the filter transfer function are listed in Table 3.2 [67]. It can be noted that the poles and zeros do

not appear in conjugate pairs due to the asymmetry of the transmission response of the filter. The poles of the short-circuit admittances, y_{11} and y_{12}, and their residues, ξ_{11} and ξ_{12}, as obtained from the transfer function are listed in Table 3.2.

Similar to the case of a symmetric filter in the previous example, the residues $\xi_{11} = \xi_{22}$ of the asymmetric filter are real while $\xi_{12} = \xi_{21}$ are imaginary. However, the poles and residues of the short-circuit admittances do not appear in complex conjugate pairs. Application of the coupling matrix synthesis procedure yields the following energy coupling matrix:

$$\mathbf{M} = \begin{bmatrix} 0.0114 & -0.7600 & 0 & 0 & 0 & 0 & 0 \\ & 0.0129 & -0.5706 & 0 & 0 & 0.0481 & 0 \\ & & 0.0184 & -0.3772 & -0.4382 & 0.0089 & 0 \\ & & & -0.7474 & 0.3713 & 0 & 0 \\ & & & & 0.0047 & 0.5706 & 0 \\ & & & & & 0.0129 & 0.7600 \\ & & & & & & 0.0114 \end{bmatrix}. \quad (3.53)$$

Filter poles, p_k	Filter zeros, z_k	Poles of y_{11} and y_{12}	$\xi_{11} = \xi_{22}$	$\xi_{12} = \xi_{21}$
$-0.0956 - j1.0472$	$-j2.0000$	$-j1.1206$	0.0695	$j0.0695$
$-0.2825 - j0.8047$	$j1.2153$	$j1.0716$	0.0473	$j0.0473$
$-0.4121 - j0.3358$	$j1.4030$	$j1.0279$	0.0911	$-j0.0911$
$-0.0363 + j1.0201$		$-j0.9279$	0.1522	$-j0.1522$
$-0.1343 + j0.9311$		$j0.7625$	0.1199	$j0.1199$
$-0.2807 + j0.6843$		$-j0.3922$	0.1757	$j0.1757$
$-0.4079 + j0.2278$		$j0.2543$	0.1690	$-j0.1690$

Table 3.2. The poles and zeros of the filter transfer function, and the poles and residues of the short-circuit admittances of a 7th-order asymmetric filter.

The above coupling matrix corresponds to the microring topology shown in Figure 3.8, which consists of triplet formations as shown by the triangles in the figure. As mentioned in section 3.3, the triplets will lead to coupling between counter-propagating modes, resulting in the generation of a reflected wave at the input port. To overcome this problem, we have made use of the matrix reduction procedure called cross-pivot annihilation given in [65] to generate the following reduced matrix $\mathbf{M_1}$.

$$\mathbf{M}_1 = \begin{bmatrix} 0.0114 & 0.5374 & 0 & 0 & 0 & 0.5374 & 0 \\ & 0.0611 & 0.5661 & 0 & 0 & 0 & 0.5374 \\ & & -0.4267 & 0 & 0 & 0 & 0 \\ & & & -0.7474 & 0.5293 & 0 & 0 \\ & & & & 0.4498 & 0.5751 & 0 \\ & & & & & -0.0352 & -0.5374 \\ & & & & & & 0.0114 \end{bmatrix} \tag{3.54}$$

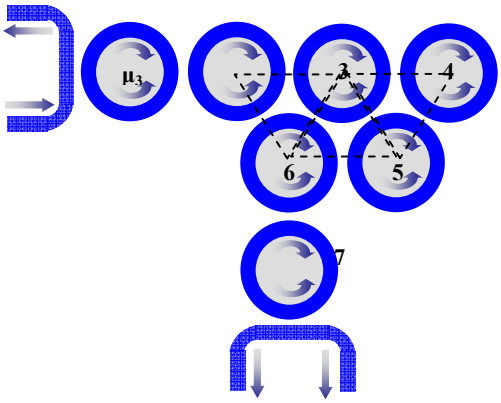

Figure 3.8. Triplet formation in the 7th order asymmetric microring filter with coupling matrix in equation 3.53.

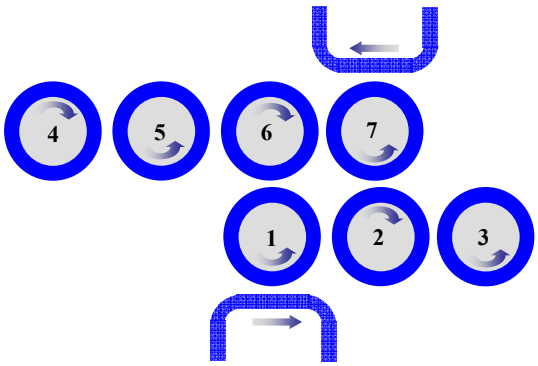

Figure 3.9. Cul-de-sac coupling topology of the 7th order asymmetric filter with coupling matrix in equation 3.54.

Figure 3.9 shows the coupling topology corresponding to the above coupling matrix, which is known as the "cul-de-sac" configuration in microwave filter design [65]. This filter topology has the important advantage that it requires only one negative coupling element in the entire network as long as the number of transmission zeros is less than $N-2$. It is noted that the diagonal elements in the coupling matrix are non-zero, indicating that the microrings are detuned from the center frequency ω_0 of the filter passband.

Next the coupling matrix $\mathbf{M_1}$ is scaled to obtain the coupling parameters for the 25 GHz bandpass filter. This yields $\widetilde{\mu}_i = \widetilde{\mu}_o = 11.3816$ and the scaled matrix

$$\widetilde{\mathbf{M}} = \begin{bmatrix} 0.8923 & 42.2088 & 0 & 0 & 0 & 42.2088 & 0 \\ & 4.7966 & 44.4642 & 0 & 0 & 0 & 42.2088 \\ & & -33.5104 & 0 & 0 & 0 & 0 \\ & & & -58.6984 & 41.5723 & 0 & 0 \\ & & & & 35.3269 & 45.1662 & 0 \\ & & & & & -2.7650 & -42.2088 \\ & & & & & & 0.8923 \end{bmatrix}. \tag{3.55}$$

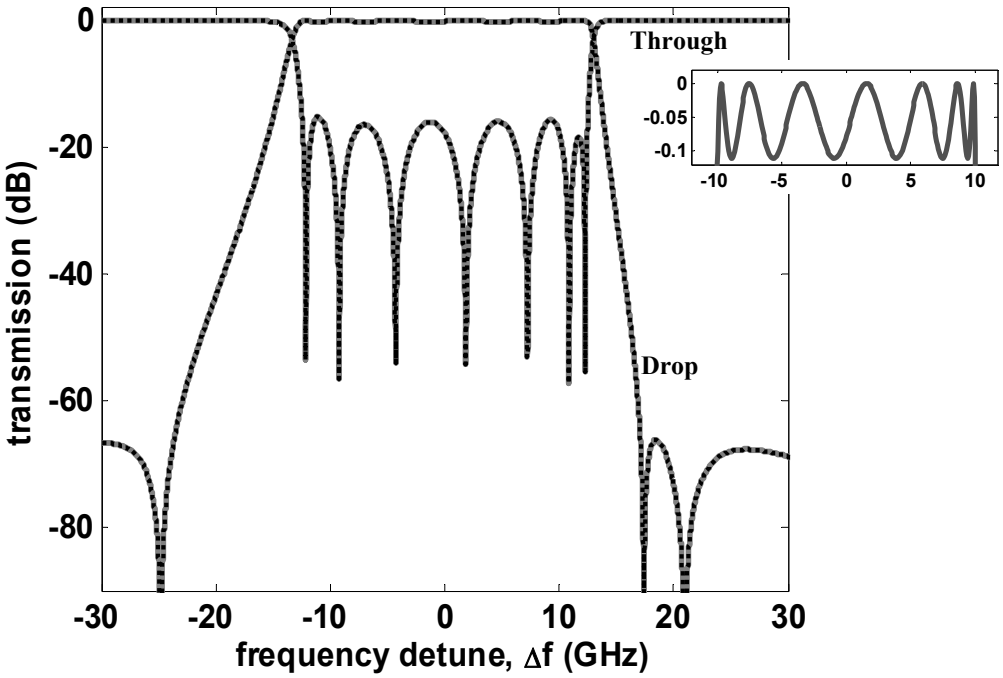

Figure 3.10. Synthesized transmission response and reflection responses (solid gray line) of a 7th-order 25GHz-bandwidth asymmetric elliptic filter. The dots represent the target filter responses. The inset shows a close-up view of the passband.

In Figure 3.10 the transmission and reflection responses (solid grey line) at the drop port and through port, respectively, of the synthesized filter are plotted against the responses of the target filter transfer functions (dotted black line). It is seen that the placement of two transmission zeros on the right-hand side of the passband results in a much steeper roll-off on that side compared to the left-hand side. In Figure 3.11 the transmission response of the 7^{th}-order asymmetric filter (solid black line) is compared to that of a conventional 7^{th}-order Butterworth filter (dashed grey line) having the same bandwidth of 25GHz. The Butterworth filter response was obtained from 7 microrings arranged in a serial coupling topology. The superior performance of the asymmetric filter is apparent from the much sharper band transitions and higher isolation levels compared to the all-pole symmetric Butterworth filter.

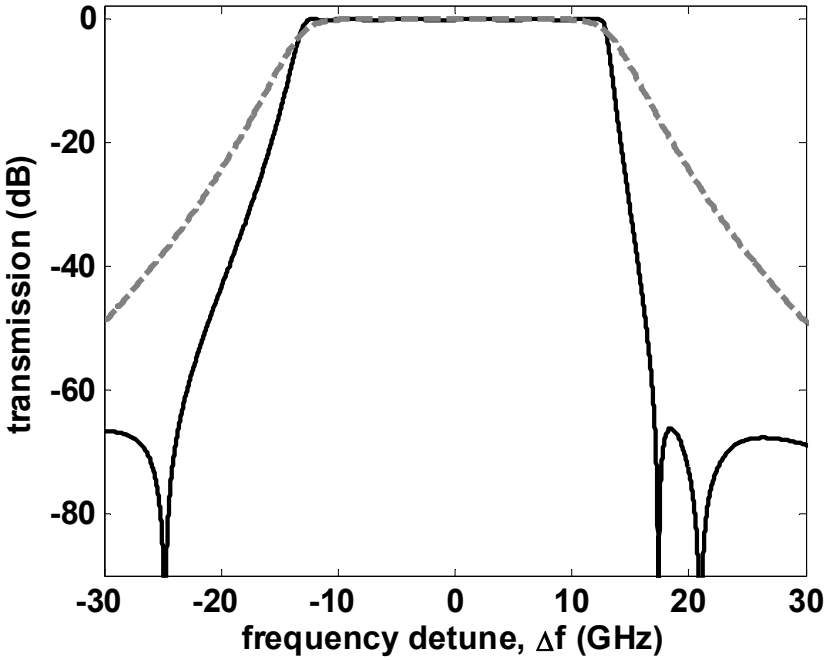

Figure 3.11 Synthesized transmission response (solid black line) of a 7th-order 25GHz-bandwidth asymmetric elliptic filter as against a 7th order Butterworth filter response (dashed grey line).

3.4.3 A sixth order linear phase maximally flat filter

In light of the recent interest in optical slow wave structures for applications in optical buffering [44], we consider the application of the 2D coupled microring network for realizing low-dispersion optical buffers. The example given is a sixth order, 25 GHz bandwidth linear phase optical filter having flat top responses in both amplitude and group delay. The transfer functions for linear phase filters have been derived for microwave filters [68], from which we obtain the following polynomials for the prototype filter:

$$P(s) = 6s^4 - 72s^2 + 450,$$

$$Q(s) = 4s^6 + 36s^5 + 162s^4 + 456s^3 + 828s^2 + 900s + 450. \qquad (3.56)$$

The above transfer function has six poles at $\{-0.8729 \pm j2.3434, -1.6797 \pm j1.2959, -1.9474 \pm j0.4525\}$, and four complex zeros at $\{\pm 2.7074 \pm j1.1533\}$. Applying the polynomial factorization in equation 3.32 we obtain the polynomial *R(s)* of the reflection response S_r as:

$$R(s) = 4s^6 \tag{3.57}$$

Following the synthesis procedure, the short-circuit admittance matrix $\boldsymbol{Y}_{sc}$ is derived whose poles and residues are listed below in Table 3.3. The reduced coupling matrix $\mathbf{M_1}$ is next obtained to give:

$$\mathbf{M}_1 = \begin{bmatrix} 0 & 2.7487 & 0 & 0 & 0 & 0.1667 \\ & 0 & 1.4239 & 0 & 0.3775 & 0 \\ & & 0 & 0.9559 & 0 & 0 \\ & & & 0 & 1.4239 & 0 \\ & & & & 0 & 2.7487 \\ & & & & & 0 \end{bmatrix}. \tag{3.58}$$

It is seen that the optimized matrix contains 7 coupling elements. Moreover, all coupling elements are positive since the filter transfer function does not have transmission zeros on the imaginary axis. The corresponding microring coupling topology is shown in Figure 3.12

Poles of y_{11} and y_{12}	$\xi_{11} = \xi_{22}$	$\xi_{12} = \xi_{21}$
j 3.4706	0.7737	j 0.7737
$-j$ 3.4706	0.7737	$-j$ 0.7737
j 2.7550	0.9799	j 0.9799
$-j$ 2.7550	0.9799	$-j$ 0.9799
j 0.7844	0.4963	j 0.4963
$-j$ 0.7844	0.4963	$-j$ 0.4963

Table 3.3. The poles and residues of the short-circuit admittances of the 6th-order linear phase filter.

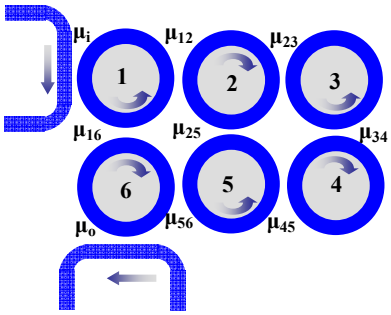

Figure 3.12. Folded coupling topology of the 6th-order linear phase microring filter with coupling matrix given by equation 3.58.

To obtain a filter bandwidth of 25GHz, the energy coupling coefficients are scaled accordingly to give $\tilde{\mu}_i = \tilde{\mu}_o = 26.5868$ and

$$\tilde{\mathbf{M}} = \begin{bmatrix} 0 & 215.8900 & 0 & 0 & 0 & 13.0900 \\ & 0 & 111.8300 & 0 & 29.6449 & 0 \\ & & 0 & 75.0748 & 0 & 0 \\ & & & 0 & 111.8300 & 0 \\ & & & & 0 & 215.8900 \\ & & & & & 0 \end{bmatrix}. \quad (3.59)$$

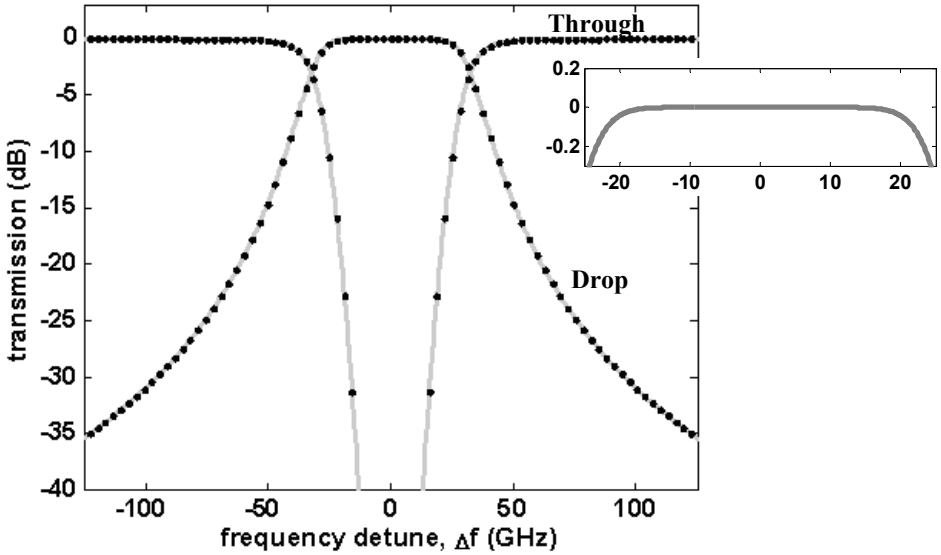

Figure 3.13. Synthesized transmission and reflection spectral responses (solid gray line) of a 6th-order linear phase microring filter with a 25GHz flat-top bandwidth. The dots represent the target filter responses. The inset shows a close-up view of the passband.

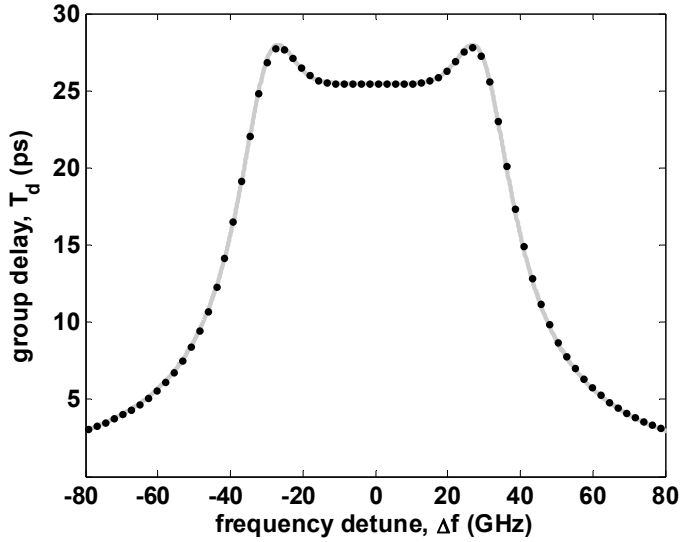

Figure 3.14. Synthesized group delay response of the linear phase microring filter (solid gray) along with the target response (black dots).

The transmission and reflection responses at the drop port and through port of the synthesized filter are plotted (solid grey line) against the responses of the target filter transfer functions (black dots) in Figure 3.13. The transmission response is seen to exhibit a flat top passband. The group delay response at the drop port is shown in Figure 3.14, which shows a flat top group delay in the pass band with a constant group delay of 25ps over the 25GHz bandwidth.

3.4.4 A predistorted sixth-order elliptic filter

To illustrate the predistortion technique discussed in section 3.1, we consider the design of a 6th-order elliptic microring filter with 30GHz bandwidth, 0.1dB in-band ripple and 40dB out-of-band rejection. The prototype filter transfer function which meets the above specifications has six poles at p_k = {–0.0744 ± j1.0609, –0.2961 ± j0.9154, –0.6059 ± j0.4103} and four zeros at z_k = {± j1.3153, ± j1.6900}. Following the synthesis procedure, the coupling parameters of the filter for lossless case are determined to be μ_i = μ_o = 13.5664, and the coupling matrix is given by:

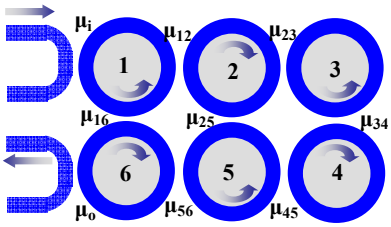

Figure 3.15. Folded coupling topology of a 6th-order elliptic microring filter with coupling matrix given by equation 3.60.

$$\tilde{\mathbf{M}} = \begin{bmatrix} 0 & 77.3661 & 0 & 0 & 0 & 5.4460 \\ & 0 & 50.8295 & 0 & -26.7689 & 0 \\ & & 0 & 73.7010 & 0 & 0 \\ & & & 0 & 50.8295 & 0 \\ & & & & 0 & 77.3661 \\ & & & & & 0 \end{bmatrix}. \tag{3.60}$$

The microring filter topology corresponding to the above coupling matrix is shown in Figure 3.15. Figures 3.16(a) and 3.16(b) shows the spectral responses of the filter at the drop port and through port, respectively, in the absence of resonator loss (dashed gray lines). It can be seen from Figure 3.16(a) inset that the lossless design conforms with the target specifications for the filter passband, exhibiting a ripple of only 0.1dB over the entire 30GHz bandwidth. Next the effect of uniform resonator loss on the responses of the lossless design was examined. For this purpose we assume that the microring waveguides are realized on a high-index material system such as silicon-on-insulator, with a propagation loss of 3.0dB/cm and a group index n_g of 4.5. The corresponding energy loss γ_L calculated from equation 2.16 is 0.0244. The drop-port and through-port spectral responses of the lossy filter are computed and plotted as solid gray lines in Figures 3.16(a) and 3.16(b), respectively. It can be seen that loss in the microrings causes the filter passband to become rounded at the edges, resulting in as much as 2.5dB ripple across the 30GHz bandwidth. In addition, the filter also exhibits an in-band insertion loss of 0.7dB. By contrast, the through-port response remains less affected by the resonator loss.

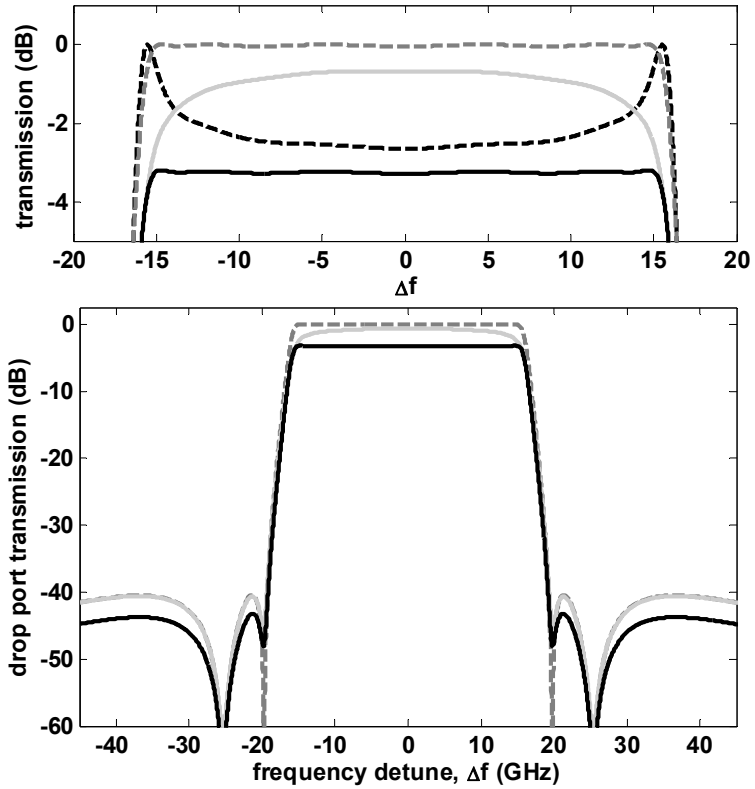

(a)

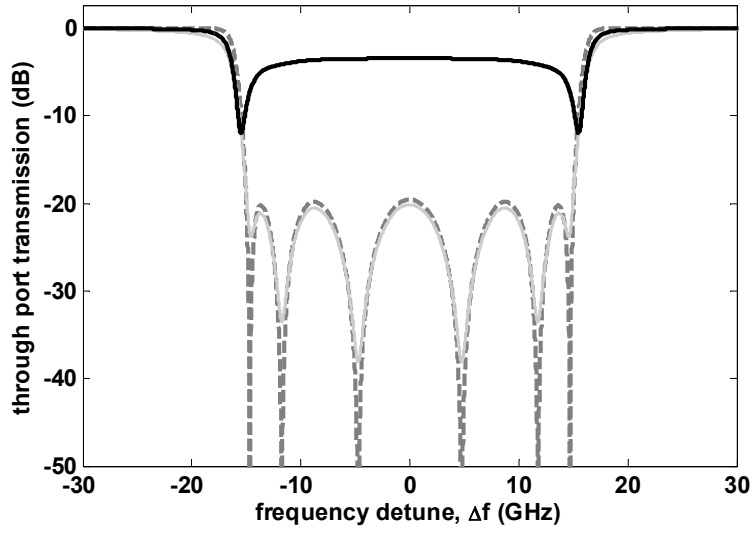

(b)

Figure 3.16. (a) Drop-port response and a close-up view of the passband (upper panel), and (b) through-port response of a 6th-order, 30GHz-bandwidth elliptic microring filter. Dashed gray lines and solid gray lines are the responses of the undistorted filter design in the absence of loss and when the normalized energy loss is $\gamma_L = 0.0244$, respectively. Dashed black lines and solid black lines are the responses of the predistorted filter with no loss and when $\gamma_L = 0.0244$, respectively.

To recover the flat-top passband of the filter in the presence of loss, the filter poles are shifted by an amount equal to γ_L to obtain the new values $p'_k = \{-0.0499 \pm j1.0609,\ -0.2717 \pm j0.9154,\ -0.5815 \pm j0.4103\}$. Synthesis of the predistorted filter yields the new optimum coupling coefficients $\mu_i = 5.9481$, $\mu_o = 17.4666$, and coupling matrix

$$\widetilde{\mathbf{M}} = \begin{bmatrix} 0 & 69.8519 & 0 & 0 & 0 & 6.6677 \\ & 0 & 47.7532 & 0 & -27.1056 & 0 \\ & & 0 & 72.6505 & 0 & 0 \\ & & & 0 & 57.2706 & 0 \\ & & & & 0 & 102.7142 \\ & & & & & 0 \end{bmatrix}. \qquad (3.61)$$

The elements of the new coupling matrix are slightly different from those in equation 3.60 but the coupling topology is unchanged. The drop-port and through-port responses of the predistorted filter in the presence of a normalized loss of $\gamma_L = 0.0244$ are shown by the solid black lines in Figures 3.16(a) and 3.16(b), respectively. In the upper panel of Figure 3.16(a) we also plot the drop-port response of the predistorted filter when there is no loss (dashed black line). The lossless predistorted filter has a spectral shape with transmission peaks at the band edges to compensate for the edge-rounding effect of resonator loss. When loss is introduced, the predistorted filter is seen to completely recover its flat passband, with the in-band ripple reduced to 0.1dB across the entire 30GHz bandwidth although the insertion loss is now increased to 3.25dB. This extra loss at the drop port of the filter is a result of the optical signal at frequencies near the band center being redirected to the through port in order to generate a flat passband at the drop port. From Figure 3.16(b), it is seen that the through-port transmission of the predistorted filter (solid black line) is indeed much higher than that of the undistorted design (solid gray line). Note that although the predistorted filter design suffers from an increased in-band insertion loss compared to the undistorted filter, its in-band ripple is also drastically reduced from the 2.5dB value exhibited by the lossy undistorted filter. In this respect, the

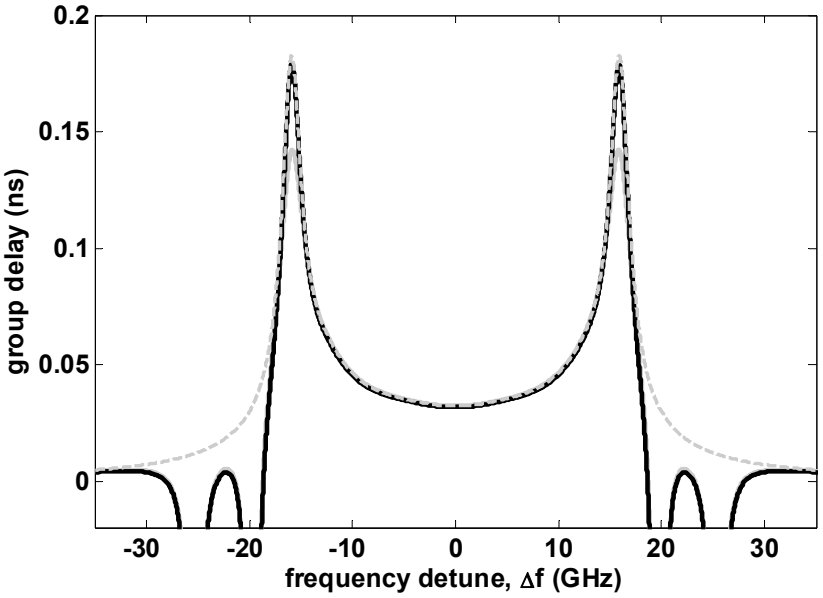

Figure 3.17. Group delay response of a 6th-order 30GHz-bandwidth elliptic microring filter. The inset shows a close-up view of the peak on the right. Dashed gray line and solid gray line are the responses of the undistorted filter design in the absence of loss and when the energy loss is γ_L = 0.0244, respectively. Solid black line is the response of the predistorted filter when γ_L = 0.0244.

predistorted design provides a more optimum elliptic filter response since it meets the target specifications of the filter passband.

In Figure 3.17 we plot the group delay response at the drop port of the undistorted filter design for the cases when there is no loss (dashed gray line) and when the normalized loss is γ_L = 0.0244 (solid gray line). The effect of loss is seen here as a reduction in the group delay at the band edges. For comparison, the group delay response of the predistorted filter in the presence of loss (solid black line) is also shown. The predistorted filter is seen to have identical in-band group delay characteristics as those of the undistorted, lossless filter. Thus the predistortion technique also yields excellent recovery of the in-band phase characteristics of the filter in the presence of loss.

3.5 Summary

A new microring filter architecture based on a two-dimensional array of direct-coupled microring resonators was proposed which can realize advanced filter responses with transmission zeros. A synthesis method was also developed for the filter architecture based on an equivalent electrical circuit network. Several filter examples were presented

to demonstrate the capability of the 2D topology in realizing a variety of complex high order optical filter responses, such as elliptic filters, asymmetric filter responses, flat top group delay filters. It was also shown that for the same prescribed transfer function, several alternative filter topologies can be realized, from which an optimum design with respect to ease of layout and fabrication can be chosen. The use of predistortion technique to recover both magnitude and group delay responses in the presence of loss was also presented.

Chapter 4

Generalized Parallel-Cascaded Microring Networks

The general 2D array of coupled microrings proposed in chapter 3 has a disadvantage in that it requires negative coupling elements for the realization of filters with transmission zeros on the imaginary frequency axis. Although it is possible to reduce the number of negative coupling elements, from the fabrication perspective it is desirable to avoid negative coupling elements altogether. Recently a new architecture based on microring doublets arranged in a parallel cascaded configuration was proposed [69] as shown in Figure 4.1. This architecture, which is also referred to as the microring ladder filter, has differential π-phase shift elements ψ in between the stages as shown in the figure. Each

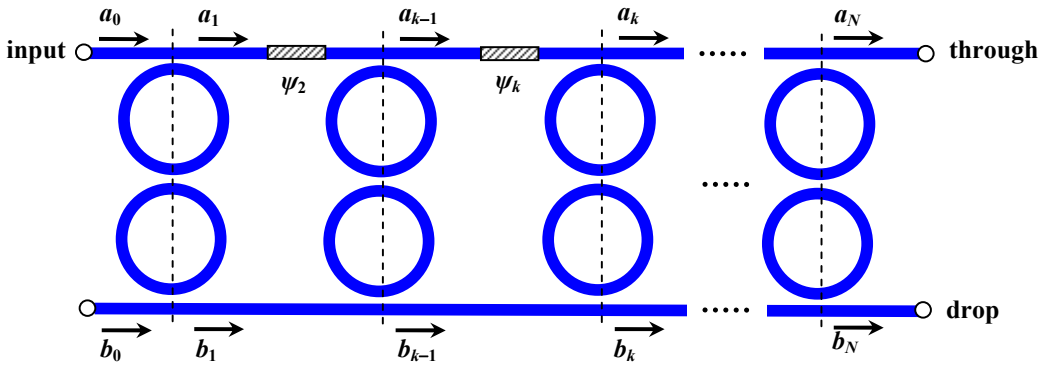

Figure 4.1. Schematic of a double-microring ladder filter.

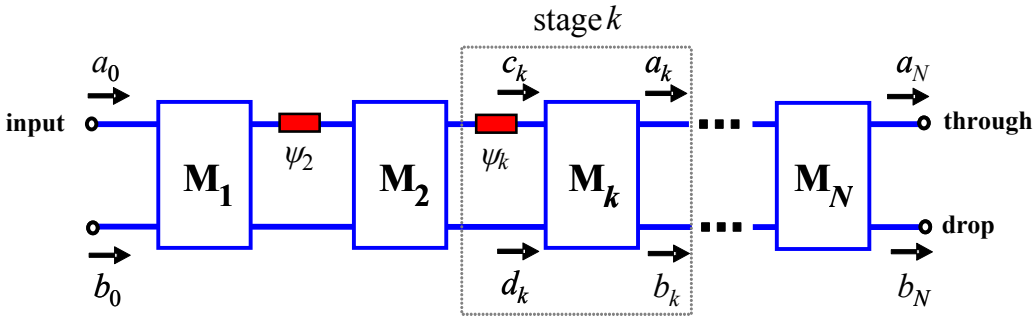

Figure 4.2. Schematic of a generalized parallel-cascaded array of N two-port microring networks.

microring stage consists of a simple symmetric and synchronous microring doublet. The advantage of this architecture is that it requires only positive coupling elements to realize filter transfer functions with transmission zeros located on or symmetrically distributed about the imaginary axis of the complex frequency plane. Also each stage of the ladder network can be independently optimized which makes the device amenable to a modular design approach.

In this chapter we extend this ladder architecture to a more general form as shown in Figure 4.2. In this form the architecture consists of a generalized ladder array of N symmetric two-port microring networks. The networks are connected via two parallel bus waveguides, which are assumed to have identical lengths L_k in each stage k except for a possible differential phase shift $\psi_k = e^{-j\theta_k}$ in the upper branch. Such a cascaded array architecture is potentially attractive for realizing very high order microring filters in a much more compact layout than the double-microring ladder. However, this architecture retains all the advantages of the double-microring ladder such as all-positive coupling elements, modular design approach etc.

4.1 Generalized parallel-cascaded microring topology

In this section we provide a detailed description of the generalized microring ladder array and derive the transfer functions of the architecture based on the transfer matrix formalism of two port microring networks. Consider the parallel-cascaded array of two-port microring networks in Figure 4.2. Here each k^{th} two-port network in the array is assumed to consist of n_k direct-coupled microring resonators. The microrings 1 and n_k of

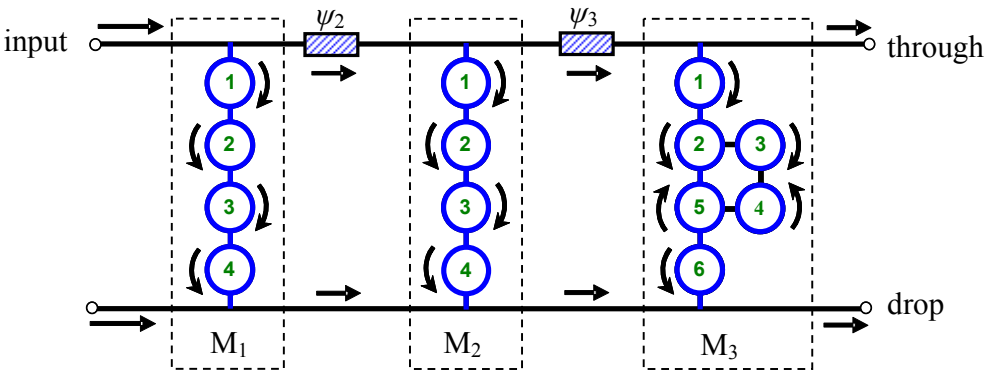

Figure 4.3. A three stage parallel-cascaded array of feed forward network.

the two port network are also coupled to the upper and lower bus waveguides, respectively. To better visualize this, an example of a three stage ladder array is shown in Figure 4.3. The first 2 stages are composed of $n_1 = n_2 = 4$ microrings, in which microrings 1 and 4 are coupled to the upper and lower bus waveguides, respectively. The 3rd stage is a two port network of $n_3 = 6$ microrings where microrings 1 and 6 are connected to the upper and lower bus waveguides. There are no restrictions on the coupling topology of microrings within each two port network except that the output signals at the drop port and through port of each network must propagate in the forward direction along the bus waveguides to the next stage. This condition restricts the analysis to arrays of feed-forward microring networks as shown in Figure 4.3, and excludes arrays of feed-back networks, such as arrays of single microring resonators [53] or the network shown in Figure 4.4, in which the drop port and through port signals propagate in opposite directions in the two bus waveguides. Such feed-back network arrays exhibit additional resonances, or poles, associated with the connecting bus waveguides and

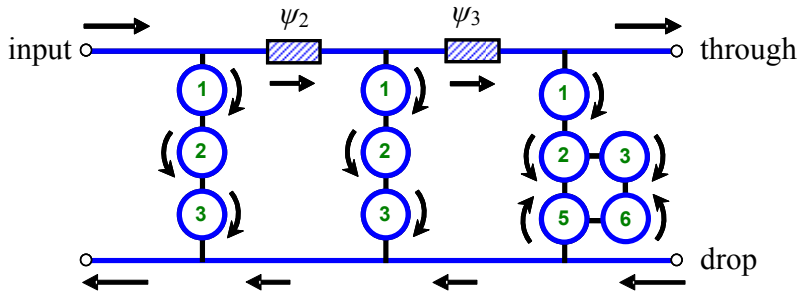

Figure 4.4. A three stage parallel-cascaded array of feed back network.

generally requires a numerical optimization approach [53] to design them. Additionally, each microring resonator in the feed forward network is assumed to support only either a clockwise or counter-clockwise propagating mode, so that coupling topologies resulting in counter-propagating waves in the microrings (See Figure 3.3) are also excluded. To simplify the following analysis, the microring resonators are assumed to be lossless and synchronously tuned.

4.1.1 Transfer matrix analysis of the generalized microring ladder array

In chapter 3 it was shown that any arbitrary 2D coupled microring resonator network may be modeled by a lossless reciprocal network of coupled LC oscillators. Referring to Figure 4.2, the transfer matrix $\mathbf{M}_k$ of the k^{th} two-port network has the form:

$$\begin{bmatrix} a_k \\ b_k \end{bmatrix} = \mathbf{M}_k \begin{bmatrix} c_k \\ d_k \end{bmatrix} = \frac{1}{G_k(s)} \begin{bmatrix} F_k(s) & -jH_k(-s)\sigma_k \\ jH_k(s) & -F_k(-s)\sigma_k \end{bmatrix} \begin{bmatrix} c_k \\ d_k \end{bmatrix} \tag{4.1}$$

where $s = j(\omega - \omega_0)$, ω_0 is the center frequency of the filter, $\sigma_k = \pm 1$, $F_k(s)$, $H_k(s)$ and $G_k(s)$ are polynomials of the transfer functions of the microring network. In particular $F_k(s)$ and $G_k(s)$ have degree n_k and $H_k(s)$ has degree $m_k \leq n_k - 2$. Since the microrings are synchronously tuned, the coefficients of F_k, H_k and G_k are real, with the leading coefficient of G_k assumed to be normalized to 1. For a lossless network the matrix $\mathbf{M}_k$ is para-unitary, so that the following power conservation relation is satisfied [70].

$$F_k(s)F_k(-s) + H_k(s)H_k(-s) = G_k(s)G_k(-s)\,. \tag{4.2}$$

Also the reciprocity condition of the two port microring network requires that

$$\mathbf{M}_k(2, 1) = \mathbf{M}_k(1, 2),$$

or

$$H_k(s) = -H_k(-s)\sigma_k\,. \tag{4.3}$$

In the above condition, σ_k is either −1 or +1 corresponding to whether H_k polynomial is even or odd-ordered. The two parallel bus waveguides in each k^{th} stage along with the differential phase shift factor ψ_k can be represented by the transfer matrix $\mathbf{\Lambda}_k$

$$\mathbf{\Lambda}_k = e^{-j\beta L_k}\begin{bmatrix} \psi_k & 0 \\ 0 & 1 \end{bmatrix} \tag{4.4}$$

where β is the propagation constant of the waveguides, L_k is the length of the two parallel bus waveguides in each k^{th} stage. The total transfer matrix $\mathbf{S}_k$ of each stage k which comprises of the two-port network and the parallel waveguides is given as

$$\mathbf{S}_k = \mathbf{M}_k\mathbf{\Lambda}_k. \tag{4.5}$$

The total transfer matrix $\mathbf{T}_N$ of the generalized array of N cascaded microring networks is obtained by multiplying the individual transfer matrices of all N stages

$$\begin{bmatrix} a_N \\ b_N \end{bmatrix} = \mathbf{T}_N\begin{bmatrix} a_0 \\ b_0 \end{bmatrix} = \mathbf{S}_N\mathbf{S}_{N-1}\cdots\mathbf{S}_1\begin{bmatrix} a_0 \\ b_0 \end{bmatrix}. \tag{4.6}$$

Performing the above matrix multiplication starting with $\mathbf{S}_1 = \mathbf{M}_1$, it can be shown that $\mathbf{T}_N$ can be expressed in the general form

$$\mathbf{T}_N = \frac{1}{Q_N(s)}\begin{bmatrix} R_N(s) & -jP_N(-s)\psi'_N\sigma'_N \\ jP_N(s) & -R_N(-s)\psi'_N\sigma'_N \end{bmatrix} \tag{4.7}$$

where $\sigma'_N = \pm 1$, $\psi'_N = \prod_{k=2}^{N}\psi_k$, and $P_N(s)$, $R_N(s)$and $Q_N(s)$ are polynomials satisfying the recursive relations

$$P_k(s) = \psi_k H_k(s)R_{k-1}(s) - \sigma_k F_k(-s)P_{k-1}(s), \tag{4.8}$$

$$R_k(s) = \psi_k F_k(s)R_{k-1}(s) + \sigma_k H_k(-s)P_{k-1}(s), \tag{4.9}$$

$$Q_k(s) = G_k(s)Q_{k-1}(s), \tag{4.10}$$

for $k = 2, 3, \ldots N$. From equation 4.7 the transfer functions at the through port and drop port of the cascaded microring network array can be obtained as

$$S_t(s) = \frac{a_N}{a_0} = \frac{R_N(s)}{Q_N(s)} \quad , \tag{4.11}$$

$$S_d(s) = \frac{b_N}{a_0} = \frac{jP_N(s)}{Q_N(s)} . \tag{4.12}$$

For filters with symmetric responses, the transfer functions $S_t(s)$ and $S_d(s)$ have real coefficients. This condition restricts the phase shift factor γ_k in equations 4.8 and 4.9 to be either 1 or −1 so that $P_k(s)$ and $R_k(s)$ have real coefficients. This implies that the differential phase shifts θ_k in all the stages of the microring array must be either 0 or π for the filter to have symmetric spectral responses. By applying $\psi_k = \pm 1$ in equations 4.8, 4.9 and 4.10, it can then be shown that the polynomials $R_N(s)$ and $Q_N(s)$ have degree

$$N_N = \sum_{k=1}^{N} n_k \tag{4.13}$$

while polynomial $P_N(s)$ has a degree of

$$M_N \le N_N - \min(n_k - m_k) , \tag{4.14}$$

where $k = 1$ to N and $m_k \le n_k - 2$ is the degree of $H_k(s)$. Since the maximum value of m_k is $n_k - 2$, the maximum degree of $P_N(s)$ is $N_N - 2$. Thus a generalized cascaded microring network array of N stages can realize a filter transfer function $S_t(s)$ with N_N poles and a maximum of $N_N - 2$ transmission zeros. It is also noted from equation 4.10 that the poles of the array, which are the roots of Q_N, are comprised of the poles of the individual microring networks, which are the roots of the G_k polynomials.

For a symmetric filter response, $\mathbf{M}_k(1, 1) = \mathbf{M}_k(2, 2)$, or $F_k(s) = -F_k(-s)\sigma_k$ in equation 4.1. Although both even and odd-ordered symmetric microring networks can satisfy the condition $F_k(s) = -F_k(-s)\sigma_k$, odd-symmetric microring networks are either of the feed-back type or require coupling topologies that give rise to counter-propagating

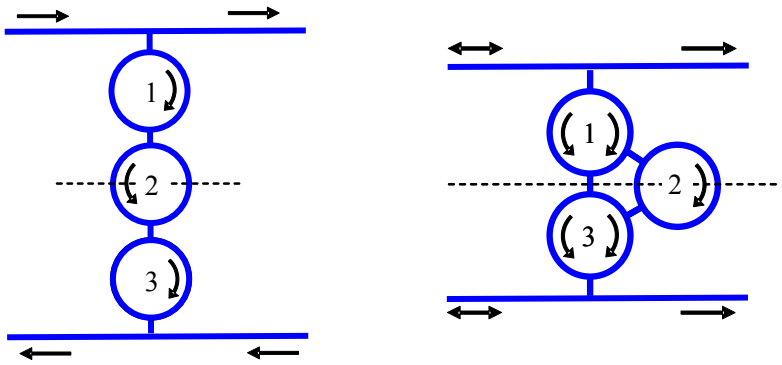

(a) (b)

Figure 4.5. Examples of odd-symmetric microring networks: (a) feed-back network; (b) network with coupling topology that gives rise to coupling between counter-propagating waves.

waves in the microrings, as illustrated in Figure 4.5. Thus in a parallel cascaded network array with symmetric spectral response, all the microring networks must be even ordered, i.e., contain an even number of resonators.

4.2 Synthesis of the generalized microring ladder array

We consider the problem of synthesizing a generalized cascaded microring network array to realize target filter transfer functions $S_t(s)$ and $S_d(s)$ as specified by the polynomials $P_N(s)$, $R_N(s)$ and $Q_N(s)$. Given the number of stages N in the array and the order n_k of the microring network in each stage, the synthesis procedure developed will provide a systematic way of extracting the microring coupling coefficients of each network k, and the interstage phase shifts $\psi_k = \pm 1$. The general approach of the synthesis procedure is summarized below.

1) First the transfer matrix $\mathbf{T}_N$ of the array is factored into the product $\mathbf{T}_N = \mathbf{S}_N\mathbf{T}_{N-1}$ using equation 4.10.
2) From the matrix $\mathbf{S}_N = \mathbf{M}_N\,\mathbf{\Lambda}_N$, the polynomials $H_N(s)$ and $F_N(s)$ along with the phase shift ψ_N of stage N can be extracted.
3) Once H_N, F_N and G_N of the two port microring network N are known, using the general 2D microring filter synthesis procedure described in chapter 3, the coupling topology and the coupling parameters of the network can be determined.

4) Steps 1 to 3 are repeated with the factorization of the remaining transfer matrix, $\mathbf{T}_{N-1}$, and the parameter extraction of the next two-port network, $\mathbf{M}_{N-1}$. This process is continued stage by stage in this manner until the first stage is reached.

4.2.1 Factorization of matrix $\mathbf{T}_k$

At each stage k, the above synthesis procedure involves factorizing the matrix $\mathbf{T}_k$ into a product $\mathbf{T}_k = \mathbf{S}_k\mathbf{T}_{k-1}$. Factorization of transfer matrices of lossless two port networks has been considered in [71] for the most general case where the polynomials F_k , H_k , R_{k-1} , P_{k-1} have degrees of n_k, maximum of n_k, N_{k-1} and maximum of N_{k-1} respectively. Given the polynomials P_k and R_k at stage k, the factorization procedure results in a *homogeneous* linear system of $N_{k-1} + n_k$ equations with $N_{k-1} + n_k + 2$ unknowns, which are the coefficients of F_k and R_{k-1}. The system of equation obtained is underdetermined and thus allows an infinite number of solutions, from which the desired solution which satisfies the power conservation condition in equation 4.2 can be chosen.

For cascaded microring networks, the polynomials H_k and P_{k-1} have degrees of at most $n_k - 2$ and $N_{k-1} - 2$, respectively. Application of the matrix factorization technique in [71] leads to a *homogeneous* linear system of $N_{k-1} + n_k$ equations with $N_{k-1} + n_k$ unknowns. Since the system is in general non-singular, there is no non-trivial solution to the factorization problem. Thus it is impossible to factor out the transfer matrices of individual microring stages from the total matrix $\mathbf{T}_N$, and the synthesis procedure cannot be carried forward. However an exception to the above problem is when the microring networks are even-symmetric which means the polynomials H_k, F_k, P_{k-1} and R_{k-1} are even-ordered so there are fewer unknowns and also fewer equations to satisfy. In the following, we show that in the case of even-symmetric networks, the matrix factorization of $\mathbf{T}_k$ leads to an *inhomogeneous* and determinate system, for which a non-trivial and unique solution always exists. In this case direct synthesis of the cascaded microring array is possible.

At each stage k the symmetric transfer matrix $\mathbf{T}_k$ is known with polynomials $P_k(s)$, $R_k(s)$ and $Q_k(s)$, where $P_k(s)$ and $R_k(s)$ are even-ordered. The degrees of $R_k(s)$, $Q_k(s)$ are N_k and the degree of $P_k(s) \leq N_k - 2$. We would like to determine the polynomials F_k, H_k

and G_k of the transfer matrix $\mathbf{M}_k$, and the polynomials P_{k-1}, R_{k-1} and Q_{k-1} of matrix $\mathbf{T}_{k-1}$. From equation 4.10, given the polynomial $Q_k(s)$, a polynomial $G_k(s)$ of degree n_k can be constructed from a subset of n_k conjugate-paired roots of $Q_k(s)$. The remaining roots of $Q_k(s)$ are used to construct the polynomial $Q_{k-1}(s)$ of degree $N_{k-1} = N_k - n_k$ such that $Q_k(s) = G_k(s)Q_{k-1}(s)$.

Next the even ordered polynomials $H_k(s)$ and $F_k(s)$ are determined as follows. From equations 4.8 and 4.9 we solve for P_{k-1} and R_{k-1} to get:

$$P_{k-1}(s) = \frac{F_k(s)P_k(s) - H_k(s)R_k(s)}{F_k^2(s) + H_k^2(s)} = \frac{D_k(s)}{G_k(s)G_k(-s)}, \tag{4.15}$$

$$R_{k-1}(s) = \psi_k^{-1} \frac{H_k(s)P_k(s) + F_k(s)R_k(s)}{F_k^2(s) + H_k^2(s)} = \frac{E_k(s)}{G_k(s)G_k(-s)}, \tag{4.16}$$

where the para-unitary property in equation 4.2 of the transfer matrix $\mathbf{M}_k$ is used in the denominators of the above expressions. In equation 4.15, since degree of $D_k(s) = N_k + n_k - 2$ and degree of $G_k(s)G_k(-s) = 2n_k$, $D_k(s)$ is required to be exactly divisible by $G_k(s)G_k(-s)$ in order to obtain a polynomial P_{k-1} of degree $N_k - n_k - 2 = N_{k-1} - 2$. In other words, the remainder of the polynomial division $D_k(s)/G_k(s)G_k(-s)$ is required to be zero. Let us express the even-ordered polynomials $H_k(s)$ and $F_k(s)$ as

$$F_k(s) = \sum_{i=0}^{n_k/2} a_{2i} s^{2i} \tag{4.17}$$

$$H_k(s) = \sum_{i=0}^{m_k/2} b_{2i} s^{2i} \tag{4.18}$$

where $m_k = n_k - 2$ and the coefficients a_{2i} and b_{2i} are to be determined. First note that since

degree of $F_k(s)$ = degree of $G_k(s)$ > degree of $H_k(s)$,

and the leading coefficient of G_k is 1, the condition in equation 4.2 requires that the leading coefficient a_{n_k} of $F_k(s)$ is ±1. Substituting equations 4.17 and 4.18 into equation 4.15 gives us

$$P_{k-1}(s) = \sum_{i=0}^{n_k/2} a_{2i} \frac{s^{2i} P_k(s)}{G_k(s)G_k(-s)} - \sum_{i=0}^{m_k/2} b_{2i} \frac{s^{2i} R_k(s)}{G_k(s)G_k(-s)}. \tag{4.19}$$

Let $A_{2i}(s)$ and $U_{2i}(s)$ be the quotient and remainder, respectively, of the polynomial division $s^{2i}P_k(s)/G_k(s)G_k(-s)$, and $B_{2i}(s)$ and $V_{2i}(s)$ be the quotient and remainder, respectively, of $s^{2i}R_k(s)/G_k(s)G_k(-s)$. These two polynomial divisions can be written as

$$\frac{s^{2i} P_k(s)}{G_k(s)G_k(-s)} = A_{2i}(s) + \frac{U_{2i}(s)}{G_k(s)G_k(-s)}, \; i = 0, 1, 2, \ldots n_k/2 \tag{4.20}$$

and

$$\frac{s^{2i} R_k(s)}{G_k(s)G_k(-s)} = B_{2i}(s) + \frac{V_{2i}(s)}{G_k(s)G_k(-s)}, \; i = 0, 1, 2, \ldots m_k/2 \tag{4.21}$$

where

degree of $U_{2i}(s) \leq$ degree of $G_k(s)G_k(-s) - 2 = 2n_k - 2$,

and degree of $V_{2i}(s) \leq$ degree of $G_k(s)G_k(-s) - 2 = 2n_k - 2$.

Substituting equations 4.21 and 4.20 into equation 4.19 gives

$$P_{k-1}(s) = \sum_{i=0}^{n_k/2} A_{2i}(s) - \sum_{i=0}^{m_k/2} B_{2i}(s) + \frac{W(s)}{G_k(s)G_k(-s)}, \tag{4.22}$$

where

$$W(s) = \sum_{i=0}^{n_k/2} a_{2i} U_{2i}(s) - \sum_{i=0}^{m_k/2} b_{2i} V_{2i}(s). \tag{4.23}$$

The polynomial $W(s)$ is the remainder polynomial of $D_k(s)/G_k(s)G_k(-s)$ in equation 4.15. For $D_k(s)$ to be divisible by $G_k(s)G_k(-s)$, $W(s)$ must be zero, that is, all the coefficients of $W(s)$ have to be 0. Denoting $u_{2i,j}$ and $v_{2i,j}$ as the jth-power coefficients of $U_{2i}(s)$ and $V_{2i}(s)$, respectively, and letting $a_{n_k} = 1$, the coefficients of $W(s)$ are equated to 0 to get

$$\sum_{i=0}^{m_k/2} a_{2i} u_{2i,j} - \sum_{i=0}^{m_k/2} b_{2i} v_{2i,j} = -u_{2i,n_k}, j = 0, 2, 4, \ldots, 2n_k - 2. \tag{4.24}$$

The above equations form an inhomogeneous linear system of n_k equations in n_k unknowns. Here the unknown variables are the coefficients $a_0, a_2, \ldots, a_{m_k}$ and $b_0, b_2, \ldots, b_{m_k}$ of the polynomials $F_k(s)$ and $H_k(s)$, respectively. The linear system in equation 4.24 is in general non-singular, so a non-trivial solution always exists to give a unique matrix factor $\mathbf{S}_k$.

The polynomials $H_k(s)$, $F_k(s)$ and $G_k(s)$ give the transfer functions of the microring network in stage k. Using the coupled-microring filter synthesis procedure from chapter 3 the energy coupling coefficients and the coupling topology of the microring network in stage k can be then determined.

If $D_k(s)$ is divisible by $G_k(s)G_k(-s)$, then it can be shown that $E_k(s)$ in equation 4.16 is also divisible by $G_k(s)G_k(-s)$ using similar arguments to those presented in [71]. The polynomials P_{k-1} and R_{k-1} can then be determined from equations 4.15 and 4.16 while Q_{k-1} is obtained from equation 4.10. The phase shift factor ψ_k in equation 4.16 is chosen to be either 1 or −1 such that, along with a proper choice of G_{k-1}, the matrix decomposition of the next stage, $\mathbf{T}_{k-1} = \mathbf{S}_{k-1}\mathbf{T}_{k-2}$, results in a microring network $\mathbf{M}_{k-1}$ which can be realized with all-positive coupling elements. The above matrix factorization procedure is repeated until the transfer matrices of all stages are obtained and the microring networks synthesized.

4.2.2 Reduction of the differential phase shift elements

In Section 4.1.1 it was shown that in order for a cascaded array of microring networks to have transfer functions with real coefficients, the differential phase shift factors ψ_k must be either 1 or –1, so that the phase shift transfer matrices are simply $\mathbf{\Lambda}_k = \text{diag}[\pm 1, 1]$. For symmetric microring networks, the transfer matrices $\mathbf{M}_k$ are symmetric with identical diagonal elements. In this case $\mathbf{M}_k$ can be shown to have the commutative property

$$\mathbf{M}_k \mathbf{\Lambda}_k \mathbf{M}_{k-1} = \mathbf{\Lambda}_k (\mathbf{M}_{k-1} \mathbf{\Lambda}_k \mathbf{M}_k) \mathbf{\Lambda}_k . \tag{4.25}$$

Specifically, if $\psi_k = 1$, then $\mathbf{\Lambda}_k$ is simply the 2×2 identity matrix $\mathbf{I}$, and the above relation gives $\mathbf{M}_k \mathbf{M}_{k-1} = \mathbf{M}_{k-1} \mathbf{M}_k$. Thus, if two symmetric microring networks are connected by bus waveguides with no differential phase shift, then the order of the two networks can be interchanged without affecting the responses of the array. On the other hand, if two symmetric microring networks are connected by waveguides with a differential π-phase shift, then $\mathbf{\Lambda}_k = \text{diag}[-1, 1]$. In this case the order of the two stages can be interchanged if a π-phase shift is also added before and after the two stages. Thus, except for a possible difference in the phase shifts between adjacent stages, the orders of the microring networks in a cascaded array can be interchanged without affecting the transfer functions of the array. Consequently, the order in which the matrix $\mathbf{T}_N$ is decomposed into the factors $\mathbf{S}_1$, $\mathbf{S}_2$, … $\mathbf{S}_N$ does not affect the device architecture, except for a possible permutation of the stage order and a difference in the phase shifts between adjacent stages. As a final step in the synthesis procedure, the commutative property of the $\mathbf{M}_k$ matrices in equation 4.25 is used to reduce the number of π-phase shift elements in the array to simplify the device architecture as shown in [72].

4.3 Numerical filter design example

Here we consider the design of an 8$^{\text{th}}$-order generalized Chebyshev filter with 6 transmission zeros using the cascaded microring network architecture. The filter specifications include

- less than 0.1dB in-band ripple
- −50dB out-of-band rejection

- a 7.5% transition width (measured as a percentage of the bandwidth).

The filter approximation procedure in [64] is used to generate the corresponding transfer functions with all the above specifications for a prototype filter with a cut-off frequency ω_c of 1rad/s. The filter polynomials are given as [72]

$$P_N(s) = 0.037085s^6 + 0.208456s^4 + 0.367288s^2 + 0.207403, \tag{4.26}$$

$$R_N(s) = s^8 + 2.366164s^6 + 1.850965s^4 + 0.511754s^2 + 0.028058, \tag{4.27}$$

$$\begin{aligned} Q_N(s) = {} & s^8 + 1.740980s^7 + 3.881669s^6 + 4.402764s^5 + 4.782464s^4 \\ & + 3.489324s^3 + 2.102237s^2 + 0.835997s + 0.209292. \end{aligned} \tag{4.28}$$

The above transfer functions have eight poles at p_k = {–0.0279 ± j1.0205, –0.1091 ± j0.9610, –0.2681 ± j0.7739, –0.4654 ± j0.3217}, six drop port zeros on the imaginary axis at z_k = {± j1.19, ± j1.19, ± j1.67}, including a double zero pair at z_k = ± j1.19. There are also eight through port zeros located on the imaginary axis at r_k = {± j0.9932, ± j0.9120, ± j0.6900, ± j0.2680}. Figure 4.6 shows the pole-zero diagram of the filter.

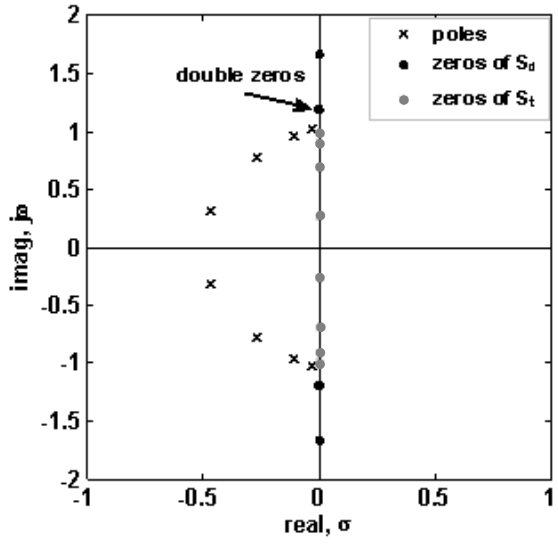

Figure 4.6. Pole-zero diagram of the 8th-order Chebyshev filter with six transmission (drop port) zeros (black dots) located on the imaginary axis. The gray dots are the zeros of the through port transfer function.

Let $\{n_1, n_2, n_3, \ldots, n_N\}$ denote, in sequential order, the number of poles in each of the N microring networks in a cascaded array. Since the order of the desired filter is $N_N = 8$, the possible array configurations that can realize the prescribed transfer functions are $\{6, 2\}$, $\{4, 4\}$, $\{4, 2, 2\}$ and $\{2, 2, 2, 2\}$, plus any permutation of each array configuration. The synthesis procedure developed in the previous section is applied to obtain the design parameters for each of the above configurations. For each stage k, the polynomial G_k was constructed from a set of n_k conjugate-paired poles of Q_k, which was then used to factor the transfer matrix $\mathbf{T}_k$ into $\mathbf{S}_k$ and $\mathbf{T}_{k-1}$. From the polynomials H_k, F_k and G_k obtained, the microring network of stage k was synthesized to determine the coupling parameters and the coupling topology. Note that since more than one choice of

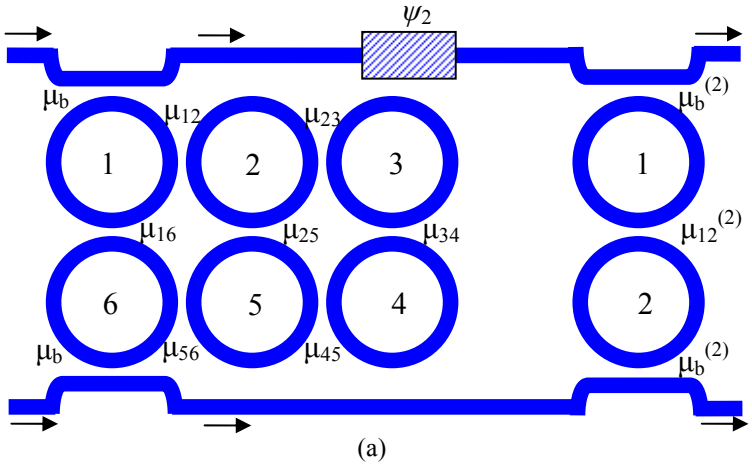

(a)

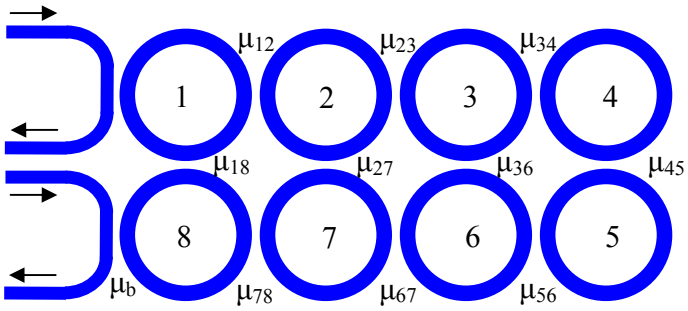

(b)

Figure. 4.7. Synthesized layouts of the 8th-order generalized Chebyshev filter: (a) configuration {6, 2} consisting of a cascade of a 6th-order microring network with a 2nd-order network; (b) configuration with 8 direct-coupled microring resonators.

G_k is possible, the matrix decomposition and hence the coupling topology of the microring network in stage k is not unique. In Figure 4.7 examples of the physical layouts of the coupling topologies are shown for the microring networks in configuration {6, 2} and configuration {8}.

Array configurations	Stage number	Poles of $G_k(s)$	Bus-to-ring energy coupling coefficients, μ_b	Ring-to-ring coupling energy coefficients, $\mu_{i,j}$	phase shift, ψ_k
{8}	Stage 1	all poles of $Q_N(s)$	1.3195	$\mu_{12} = \mu_{78} = 0.7711$ $\mu_{23} = \mu_{67} = 0.5577$ $\mu_{34} = \mu_{56} = 0.3971$ $\mu_{18} = 0.0213$, $\mu_{27} = -0.1321$ $\mu_{36} = 0.4700$, $\mu_{45} = -0.8709$	
{6, 2}	Stage 1	p_1, p_1^*, p_2, p_2^*, p_4, p_4^*	1.2340	$\mu_{12} = \mu_{56} = 0.6634$, $\mu_{23} = \mu_{45} = 0.1466$, $\mu_{34} = 0.9748$, $\mu_{25} = 0.3846$ $\mu_{16} = 0.1133$	
	Stage 2	p_3, p_3^*	0.4671	$\mu_{12} = 0.9610$	–1
{4, 4}	Stage 1	p_1, p_1^*, p_3, p_3^*	1.0719	$\mu_{12} = \mu_{34} = 0.3371$, $\mu_{14} = 0.4431$, $\mu_{23} = 0.8396$	
	Stage 2	p_2, p_2^*, p_4, p_4^*	0.7695	$\mu_{12} = \mu_{34} = 0.1126$, $\mu_{14} = 0.7971$, $\mu_{23} = 0.9972$	–1
{4, 2, 2}	Stage 1	p_1, p_1^*, p_2, p_2^*	1.2112	$\mu_{12} = \mu_{34} = 0.6349$, $\mu_{14} = 0.0788$, $\mu_{23} = 0.3734$	
	Stage 2	p_4, p_4^*	0.2363	$\mu_{12} = 1.0205$	1
	Stage 3	p_3, p_3^*	0.4671	$\mu_{12} = 0.9610$	–1
{2, 2, 2, 2}	Stage 1	p_1, p_1^*	0.9648	$\mu_{12} = 0.3217$	
	Stage 2	p_3, p_3^*	0.4671	$\mu_{12} = 0.9610$	1
	Stage 3	p_2, p_2^*	0.7323	$\mu_{12} = 0.7739$	–1
	Stage 4	p_4, p_4^*	0.2363	$\mu_{12} = 1.0205$	1

Table 4.1. Possible configurations of cascaded microring array architectures and their design parameters for an 8th-order generalized Chebyshev filter.

Table 4.1 lists the possible array configurations along with the design parameters of the microring networks and the inter-stage differential phase shift factors ψ_k. Also shown in the table for comparison is configuration {8}, which corresponds to the design of a single-stage filter with 8 direct-coupled microring resonators. For each array configuration, the poles p_k used to construct the polynomial G_k are given. The design of each microring network is specified in terms of the bus-to-ring energy coupling coefficient μ_b and the ring-to-ring coupling coefficients $\mu_{i,j}$, which denote the energy coupling between microrings i and j in the network.

In Figure 4.8 and 4.9 the amplitude and group delay responses are plotted, respectively, of the microring device configuration {4, 4} (solid black lines). The responses of the synthesized device are seen to be identical to the target transfer functions (gray dashed lines). All the other device configurations in Table 4.1 also yielded identical spectral responses. It can be noted from Table 4.1, however, that configuration {8} requires two negative ring-to-ring coupling elements, whereas all the microring networks in the cascaded array architectures have only positive coupling coefficients, which are much simpler to implement. Also, as more stages are used in an

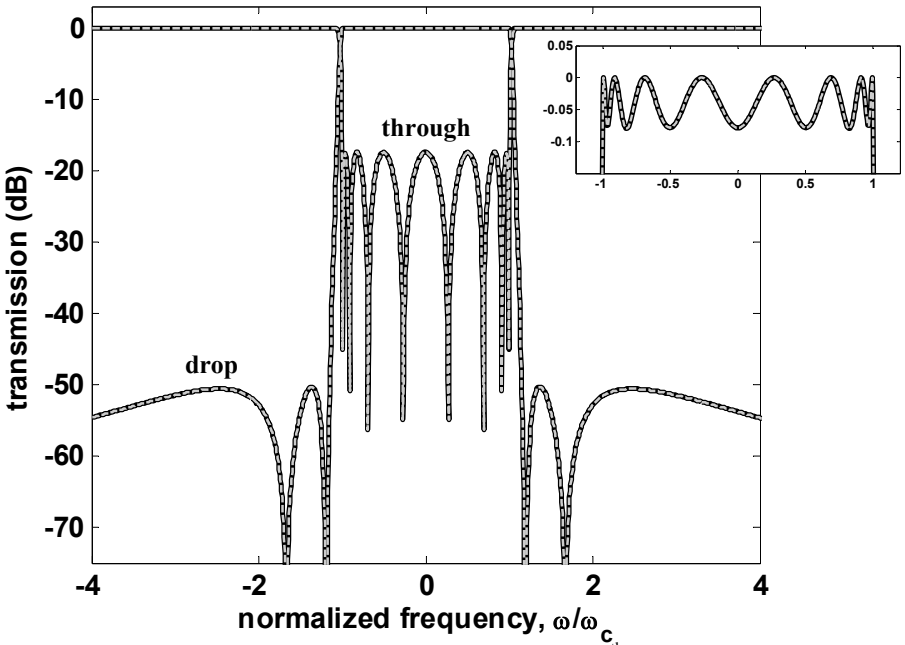

Figure 4.8. Spectral responses at the drop port and through port of the 8th-order Chebyshev filter. Gray dashed lines are the target filter responses; solid black lines are the synthesized responses. The inset shows a close-up view of the passband.

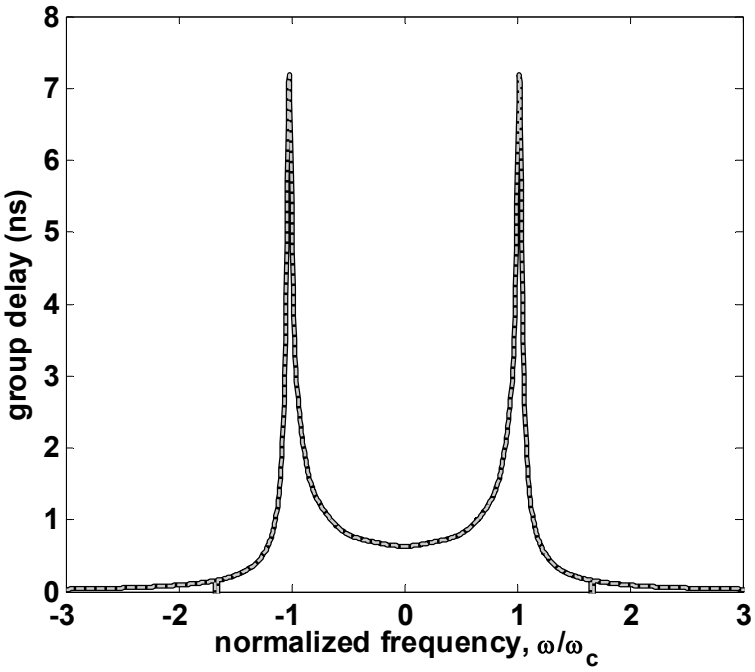

Figure 4.9. Group delay response of the 8th-order Chebyshev filter. Gray dashed lines are the target filter responses; solid black lines are the synthesized responses.

array, the microring networks become simpler, suggesting a trade off between the complexity of the networks and the number of stages in the array. Note that the array configurations {4, 2, 2} and {2, 2, 2, 2} in Table 4.1 have been reduced to the optimum forms, which contain only one π-phase shift element as indicated by the value $\psi_k = -1$.

4.4 Summary

In this chapter parallel cascaded microring networks were proposed as a generalized architecture for realizing very high order filters. A synthesis procedure was developed for designing even-symmetric microring networks with symmetric spectral responses. The advantage of the parallel cascaded microring architecture is that it can realize transmission zeros without the need for negative coupling elements. It was also shown that the inter-stage differential phase shift elements can be reducible to at most one. From the implementation point of view, the parallel cascade architecture allows for a very high order filter function to be decomposed in to multiple microring network stages, where each stage can be separately designed and optimized.

Chapter 5

Fabrication and Experimental Demonstration of Silicon Microring Filters

In this chapter we experimentally realize and demonstrate microring add-drop filters in the silicon-on-insulator (SOI) material system. First we discuss the development and optimization of the microring fabrication process flow for SOI at the University of Alberta Nanofabrication facility. As part of this fabrication process development, several compact SOI microrings were made and characterized. In particular, attempts were made to scale down the microring device footprints by reducing the radii of the microrings down to the order of the optical wavelength at 1.55 μm. Utilizing the process flow developed, a fourth order microring filter based on the parallel cascaded architecture developed in Chapter 4 is demonstrated. To facilitate this demonstration, thermal control of individual microrings was required, which necessitated the development of additional process flow to fabricate micro sized Titanium/Tungsten (TiW) heaters on top of the microrings.

5.1 Development of silicon-on-insulator fabrication process

The fabrication process begins with the choice of the SOI wafer. SOI wafers are commercially available to be readily purchased and used. However, many varieties of SOI wafers are available, and knowledge of the SOI wafer technology

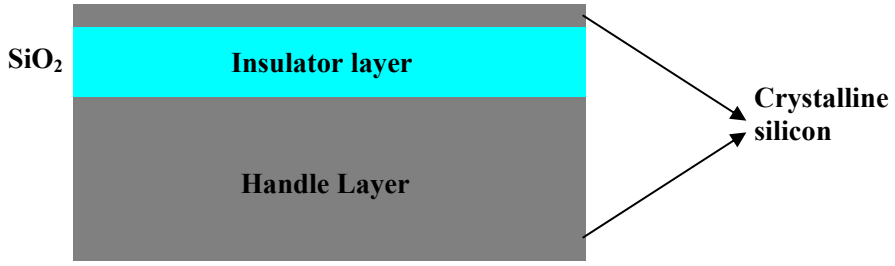

Figure 5.1. Side view of a silicon-on-insulator wafer.

and corresponding application requirements must be considered before making a selection. Originally introduced by IBM for low power operation in the CMOS IC process, SOI wafers have become an important material system for integrated photonics due to its potential for integration with CMOS electronics.

In general, a SOI wafer contains three layers as depicted in Figure 5.1. The top layer is a thin crystalline silicon layer with thickness in the range of hundreds of nanometers to one micrometer and the bottom layer is the substrate made of bulk crystalline silicon. Sandwiched between these two layers is the buffer oxide (BOX) layer made of SiO_2 with thickness in the order of a few micrometers. The thin silicon slab bounded by air on the top surface and oxide at the bottom forms a high index contrast hetero-structure in the vertical direction that can confine light due to total internal reflection.

The silicon slab thickness for optical wave guidance usually varies between 200 to 400 nm where the upper limit is to ensure single mode operation and the lower limit is to ensure strong mode confinement. The BOX layer thickness typically ranges between 3 to 1 μm to prevent mode leakage to the bulk silicon substrate. Of the various process technologies to make SOI wafers, oxygen ion beam implantation [73] and wafer bonding process [74] are the prominent methods. However, the oxide thicknesses achievable by these methods are usually less than a micrometer. Later, the French firm SOITEC created a proprietary process called “smartcut” [75] which combines both ion implantation and wafer bonding processes. The smartcut process was able to provide oxide layer thicknesses in the order of micrometers and a thin crystalline silicon layer (200-400 nm) on top which is well suited for photonic applications. After various

considerations SOITEC SOI wafers with the following specifications were selected for use in our microring device fabrication:

- Top silicon Thickness: 340 nm ± 40 nm
- Buffer Oxide Thickness: 1000 nm
- Handle wafer: 450 μm
- Active and Handle wafer: 100 mm diameter P-type <100>.

5.1.1 Fabrication process steps

The goal of this fabrication process is to realize microring structures with waveguides whose cross-sectional dimensions are in the sub-micrometer range. Another crucial feature to be realized is the coupling gap which is typically less than 200 nm. Such sub-micrometer features require high resolution patterning and hence electron beam lithography (EBL) was chosen to realize these features. The fabrication process steps are shown in Figure 5.2 and are explained below:

1) ***Dicing***: The first step is to dice a 4" SOI wafer into 1x1 cm^2 chips for processing using a wafer dicer. To clean the debris due to dicing on the chip surface, the individual chips are immersed in an ultrasonic bath.

2) ***Piranha clean***: To further clean the surface of the chips from organic residues, the chip is immersed into a 1:3 mixture of hydrogen peroxide (H_2O_2) and sulphuric acid (H_2SO_4) bath, which is also known as Piranha solution, for about 15 minutes. Piranha cleaning was followed by washing with de-ionized (DI) water and nitrogen blow drying to eliminate surface moisture. The diced and cleaned chip is illustrated in Figure 5.2 (a).

3) ***Resist coating***: The next step is to coat a layer of the electron beam lithography resist poly-methyl-methacrylate (PMMA) 950K A2 onto the chip using a resist spinner. To remove any surface moisture, the chips are prebaked at 100 ^oC on a hot plate. Given the small size of the chip, the spread cycle of a conventional spin coating process was

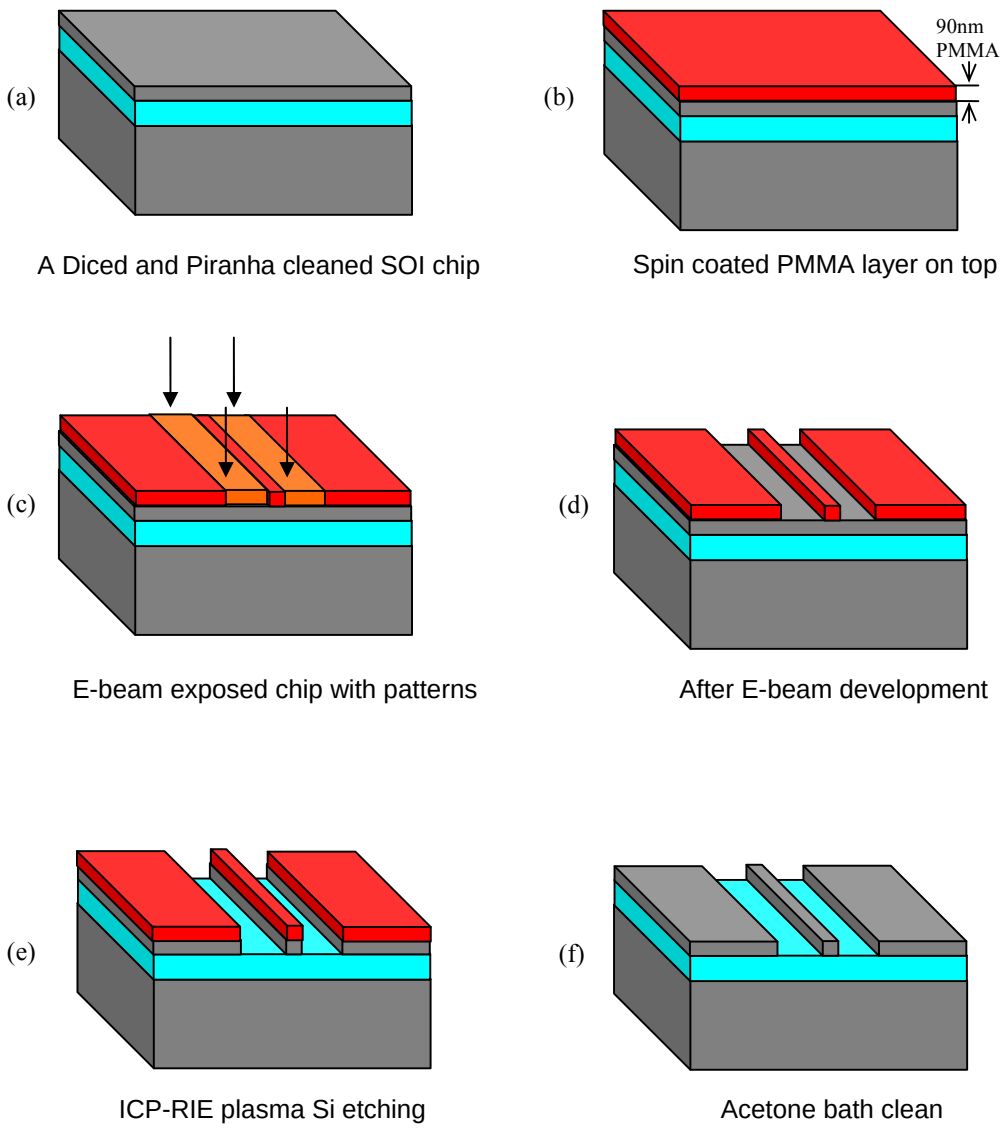

Figure 5.2. Silicon-on-insulator fabrication process for realizing optical waveguides and microrings.

eliminated. Also it was found that the long durations for ramp time lead to drying of the resist before the spin cycle, which lead to non-uniform resist thickness. Therefore ramp durations were reduced to 2 seconds. The spin coating was then performed at 4000 rpm for 40 seconds. The resist layer was measured to be approximately 90 nm thick as illustrated in Figure 5.2 (b). Post baking at 180 ^{o}C for approximately 10 minutes was done to remove any residual solvent from the resist.

4) ***Electron beam lithography (EBL)***: The electron beam lithography system used in our fabrication process is the 30 kV Raith 150 system. As mentioned before electron beam lithography can produce patterns at high resolution, allowing sub 500 nm features to be accurately defined. Also, given the 5 nm beam diameter of the electron beam, it is possible to achieve very smooth sidewalls for the waveguides. In general the achievable resolution largely depends on the resist as well as the interaction of electrons with the resist. The EBL resist chosen is one of the highest resolution resists available in the market, so the pattern quality achievable mainly depends on the electron dynamics with the resist, which is controlled by the parameters chosen on the EBL system. When an electron beam is shot at the resist, it generates back-scattered electrons in the neighbouring areas which effectively expands the exposed area. This is called proximity effect. It can be overcome in two ways: 1) by creating patterns with a predetermined bias to compensate for the expansion of the exposed area, 2) to reduce the dosage of electrons accordingly. Low energy exposure is also known to help reduce proximity effects [76, 77]. Initial experimentations were conducted with a very low energy exposure at 2 kV acceleration voltage and 35 $\mu C/cm^2$ electron dosage. However, this reduced the pattern generation speed greatly which increased the risk of long write times and the associated errors occurring in the pattern due to variations in the machine environment like temperature etc. After experimenting with the EBL parameters, the optimum parameters were determined to be: 100 $\mu C/cm^2$ electron dosage, 20 μm aperture and 10 kV acceleration voltage.

Although EBL is good for high resolution patterns, the serial writing process makes it unattractive for large non-critical features such as long input/output waveguides that were up to 2 mm. In the conventional writing process the EBL system divides the entire pattern into small blocks called write fields and performs a raster-scan type beam movement within each block to write the patterns. There is another mode of writing called "fixed beam moving stage" (FBMS) [78] where the electron beam circles at a fixed location while the stage holding the chip moves to define the required pattern. The FBMS mode was found to be a good approach for non-critical, long waveguide sections which serve as input/output waveguides. FBMS also eliminated the stitching errors in the patterns which usually occur at the

write field boundaries in the conventional writing process. The final optimized EBL process involved a combination of the conventional electron beam write mode and the FBMS write process. The EBL pattern generation on the chip is illustrated in Figure 5.2 (c).

5) ***Resist development***: PMMA is a positive EBL resist, i.e. the exposed portion of the resist becomes soluble to the resist developer. After an EBL exposure, the resist was developed in methyl isobutyl ketone (MIBK):iso-propyl alcohol (IPA) developer in the ratio of 1:3 for 30 seconds, followed by a rinse in IPA for 15 seconds and a rinse in de-ionized water for 15 seconds. This was followed by a nitrogen blow drying to eliminate any moisture. The chip at this stage looks as depicted in Figure 5.2 (d).

6) ***Inductively Coupled Plasma Reactive Ion etching (ICP-RIE)***: In this step the goal was to transfer the developed high-resolution pattern generated by EBL accurately and smoothly on to the silicon layer as depicted in Figure 5.2 (e). This is accomplished by dry etching the exposed areas of the silicon layer, with the undeveloped PMMA serving as the mask layer. It is desirable that the etched side walls of the waveguides be as vertical and smooth as possible. To achieve these etch characteristics, the Stanford Technical System's inductively-coupled plasma reactive ion etching (ICP-RIE) machine was chosen to perform the required anisotropic etch. ICP-RIE is a dry etching process where removal of material occurs due to both chemical and physical (sputtering) processes. The chemical etching could be controlled by adjusting the flow rates of the gases used in the chamber. The physical etching due to vertical ion bombardment can be controlled by adjusting the energy of the ions. By precisely controlling these physical and chemical etch rates, the desired etch characteristics can be achieved. The chemistry used in the chamber was based on SF_6/C_4F_8 gases which is similar to the Bosch process [79, 80] for deep silicon etching. However, instead of the switching between etch and passivate cycles in the Bosch process, only the etch cycle was performed. Gas flows of 40 sccm of SF_6 and 55 sccm of C_4F_8 were introduced in the chamber simultaneously whose pressure was held at 5 mTorr. Plasma was generated by supplying an ICP power of 600 watts and

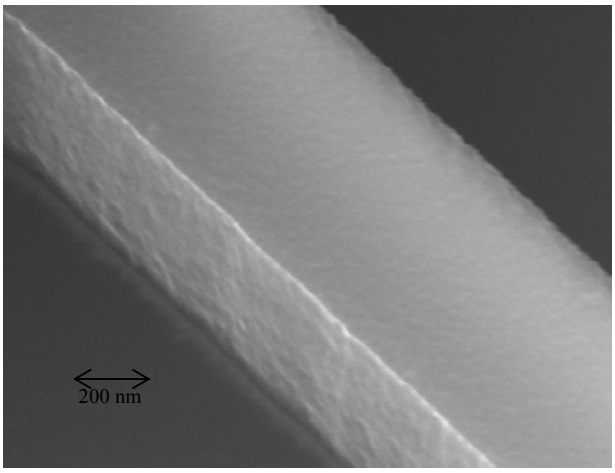

(a)

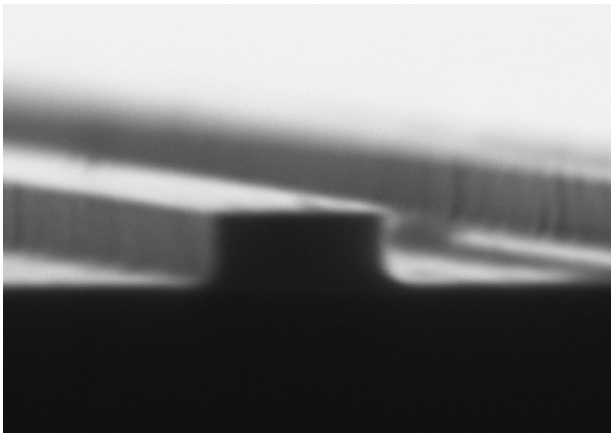

(b)

Figure 5.3. a) SEM image of a fabricated SOI bus waveguide (400x340 nm^2) with minimal surface roughness; b) SEM image of the cleaved edge showing a waveguide facet.

RF forward power of 20 watts. The fluorine free radicals generated in the plasma performs the silicon etching while the C_4F_8 coats a protective fluropolymer in the side walls, which helps produce the vertical sidewall. The energy of the ions transferred to the chip tends to raise the temperature of the silicon surface and to prevent this, the back of the substrate is cooled by liquid helium whose flow needs to be held constant. The 340 nm etch depth through the top silicon layer of the SOI chip required an etching duration of 27 seconds. An SEM picture of the etched side wall of an optical

waveguide is shown in Figure 5.3(a), where the overall surface roughness achieved through the etching process can be seen to be fairly small.

7) ***Post-etch processing***: The remaining PMMA resist was then removed in an acetone bath under ultrasonic vibrations. The final fabricated and cleaned chip looks as illustrated in Figure 5.2(f). The final step is to cleave the device to expose the waveguide facets for butt-coupling from the fibre to the strip waveguide for measurements. An SEM picture of a cleaved waveguide facet can be seen in Figure 5.3(b).

5.2 Fabrication of single microring add-drop filters

Using the fabrication process developed above, a single microring resonator with a 5.0 μm radius in the add-drop configuration was fabricated. The waveguide width and the coupling gap were designed to be 450 nm and 200 nm respectively. Figure 5.4 shows the simulated transverse electric (TE) and transverse magnetic (TM) modes of the 450 nm x 340 nm SOI waveguide at the 1.55 μm wavelength. The eigenmodes were obtained using a finite difference mode solver. For both polarizations, the waveguide was single moded and the modes were strongly confined within the waveguide.

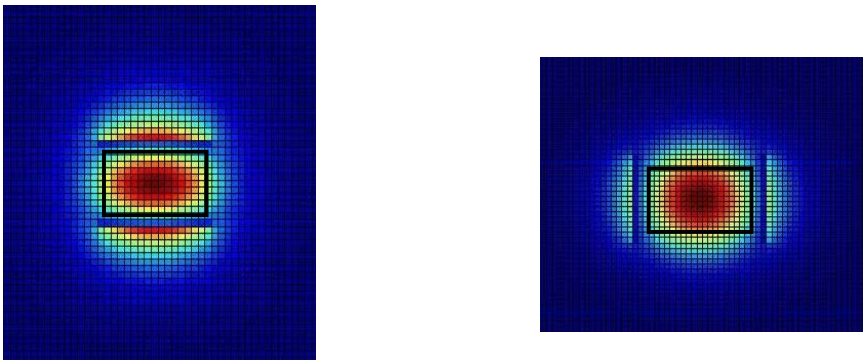

(a) (b)

Figure 5.4. Mode profile of a 450x340 nm^2 waveguide in (a) TM polarization and (b) TE polarization.

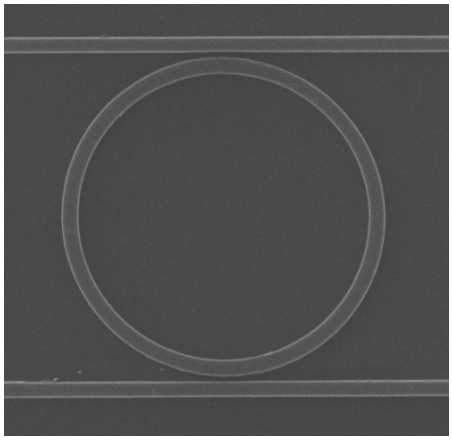

Figure 5.5. SEM image of a silicon add-drop microring with 5.0 μm radius.

With the waveguide height fixed at 340 nm, we found that the waveguide width of 450 nm is very close to the limit of the single mode regime, beyond which the waveguide becomes multimode. To prevent multimode operation in the event the waveguide width expanded due to possible fabrication errors, it was decided to lower the waveguide width in the range of 300-350 nm for future devices. From the mode profiles it was confirmed that the field leakage to the substrate through the 1μm thick buffer oxide layer is negligible.

Figure 5.5 shows a top view SEM image of the fabricated SOI microring. For both the ring and bus waveguides, the widths of the waveguides were measured to be 440 ± 5 nm. The coupling gaps between the microring and the bus waveguides were measured to be 200 ± 5 nm. The spectral characteristics of the microring device were

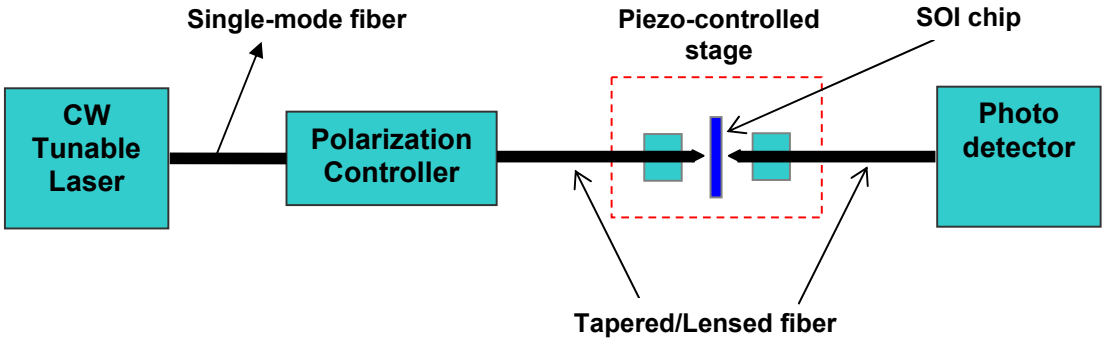

Figure 5.6. Measurement setup for coupling the laser to an SOI microring.

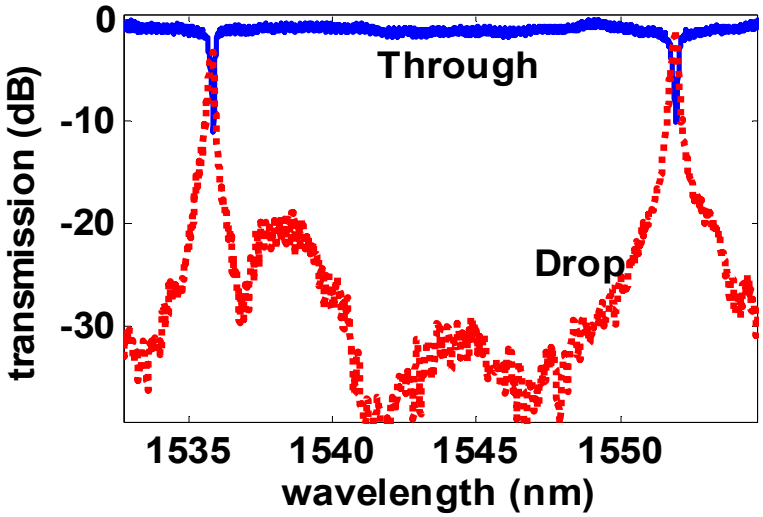

Figure 5.7. The measured drop and through port characteristics of the microring.

measured using the experimental setup shown in Figure 5.6. A Santec TSL-210V continuous-wave tunable laser with wavelength range between 1510 nm and 1630 nm was used as the light source. Although the straight waveguide supported both TE and TM polarizations, the microring had no observable resonances for the TE polarization, so the polarization state from the light source was adjusted to TM mode using a Thorlabs loop-fibre polarization controller. The light was butt coupled into the input waveguide via a tapered lensed fibre from Oz-Optics which had an anti-reflection coating at the tapered end to minimize coupling loss. The tapered fibre was mounted on a 3-axis piezo-controlled translation stage with nanometer precision movement, which was used to align the fibre to the cleaved edge of the silicon waveguide. The output light from the device was collected by another tapered fibre, which was then fed into a Newport InGaAs photo detector. The spectral response of the device was obtained by sweeping the laser wavelength at a chosen step while the transmitted power at each wavelength was recorded sequentially. Figure 5.7 shows the measured through and drop port spectral responses of the 5 μm radius microring. The bandwidth, FSR, and Q-factor of the device were determined to be 0.2 nm, 16.5 nm and 7800, respectively. The device had an insertion loss of ~ 1 dB and an out-of-band extinction ratio > 20 dB.

5.2.1 Miniaturization of silicon microring resonators

The successful design and characterization of the single SOI microring add-drop filter with a 5 μm radius initiated further exploration into the feasibility of realizing extremely compact microring resonators. The motivation for reducing the microring radius comes from the fact that the footprint of a microring resonator scales with the square of its radius and hence decreasing the radius would enable denser device integration. There is an added benefit that the free spectral range of the device also increases, which allows the filter to accommodate more WDM channels within one FSR. However, the downside of reducing the radius is that the bending loss becomes more pronounced leading to degraded filter performance. Because of the high bending loss, attempts to miniaturize microring resonators [81 - 84] until now have been restricted to bending radii of around 1.5 μm.

To explore the potential for further miniaturization of silicon microring resonators, numerical simulations were performed to assess the theoretical limits imposed by the bending loss. The usual approach for determining the bending loss of a curved waveguide is to compute the complex propagation constant of the eigenmode of interest. We numerically solved the full-wave vectorial Helmholtz equation in the local cylindrical coordinate system [85] to determine the complex propagation constant of the microring waveguide. Two SOI waveguide dimensions were considered: waveguide cross-

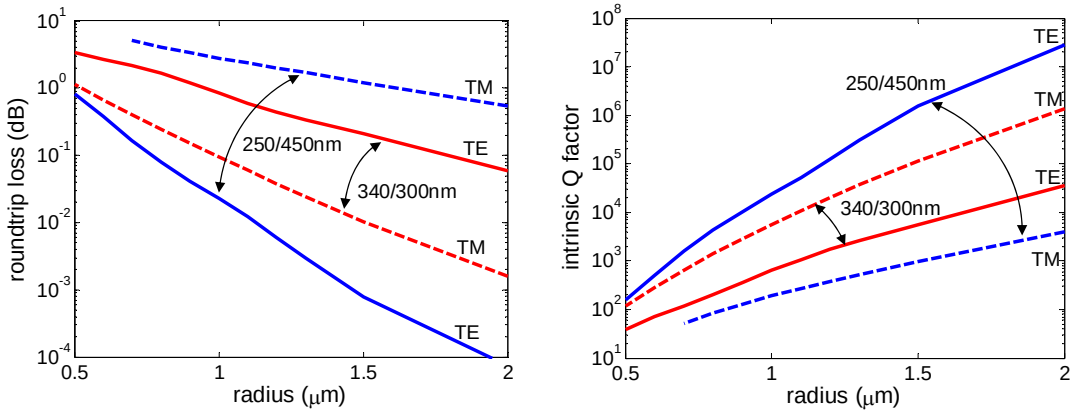

(a) (b)

Figure 5.8. (a) Dependence of the roundtrip bending loss and (b) theoretical intrinsic Q-factor on the ring radius at 1.55 μm wavelength.

section of 300x340 nm^2 [84] which was used in our work and waveguide cross-section 250x450 nm^2 [83] used by many other research groups. Figure 5.8 (a) shows the plot of the roundtrip bending loss in a microring as a function of bending radii for both TE and TM modes. The bending loss is seen to exhibit an exponential dependence on the microring radius. It is also seen that there is a strong dependence of the bending loss on the waveguide aspect ratios as well as the polarization. The 300x340 nm^2 waveguide has a lower bending loss for the TM polarization while the 250x450 nm^2 waveguide has a lower bending loss for the TE polarization. Figure 5.8 (b) shows the plot of the theoretical intrinsic Q-factor versus the bending radius. The intrinsic Q-factor was computed assuming that bending loss was the only source of intrinsic loss in the microring. At a bending radius of 1 μm, Figure 5.8 (b) shows that a microring made of 300x340 nm^2 waveguide can have a theoretical intrinsic Q-factor of 5600 in the TM mode while a microring with the 250x450 nm^2 waveguide can have a Q-factor up to 23000. These numerical simulations show that with the appropriate choice of the polarization and waveguide aspect ratio, one can achieve theoretical intrinsic Q factors limited by bending loss in the order of several thousands even for a 1 μm-radius microring.

To experimentally validate the simulation results, a set of ultra compact SOI add-drop microring resonators with radii of 1.5, 1.4, 1.3, 1.1, and 1.0 μm were fabricated. The waveguide width was 300 nm and the coupling gaps between the bus and ring waveguides were fixed at 200 nm. In all the fabricated devices, the ring waveguide widths were measured to be 310 ± 5 nm and the coupling gaps between the microring and

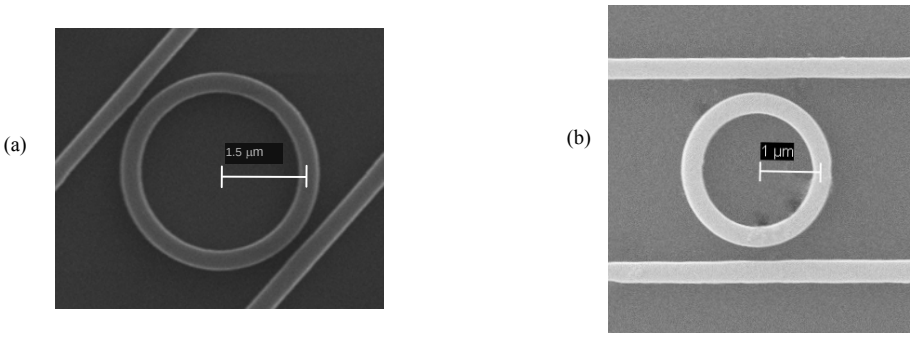

Figure 5.9 SEM image of a silicon add-drop microring resonator (a) with 1.5 μm radius (b) with 1.0 μm radius.

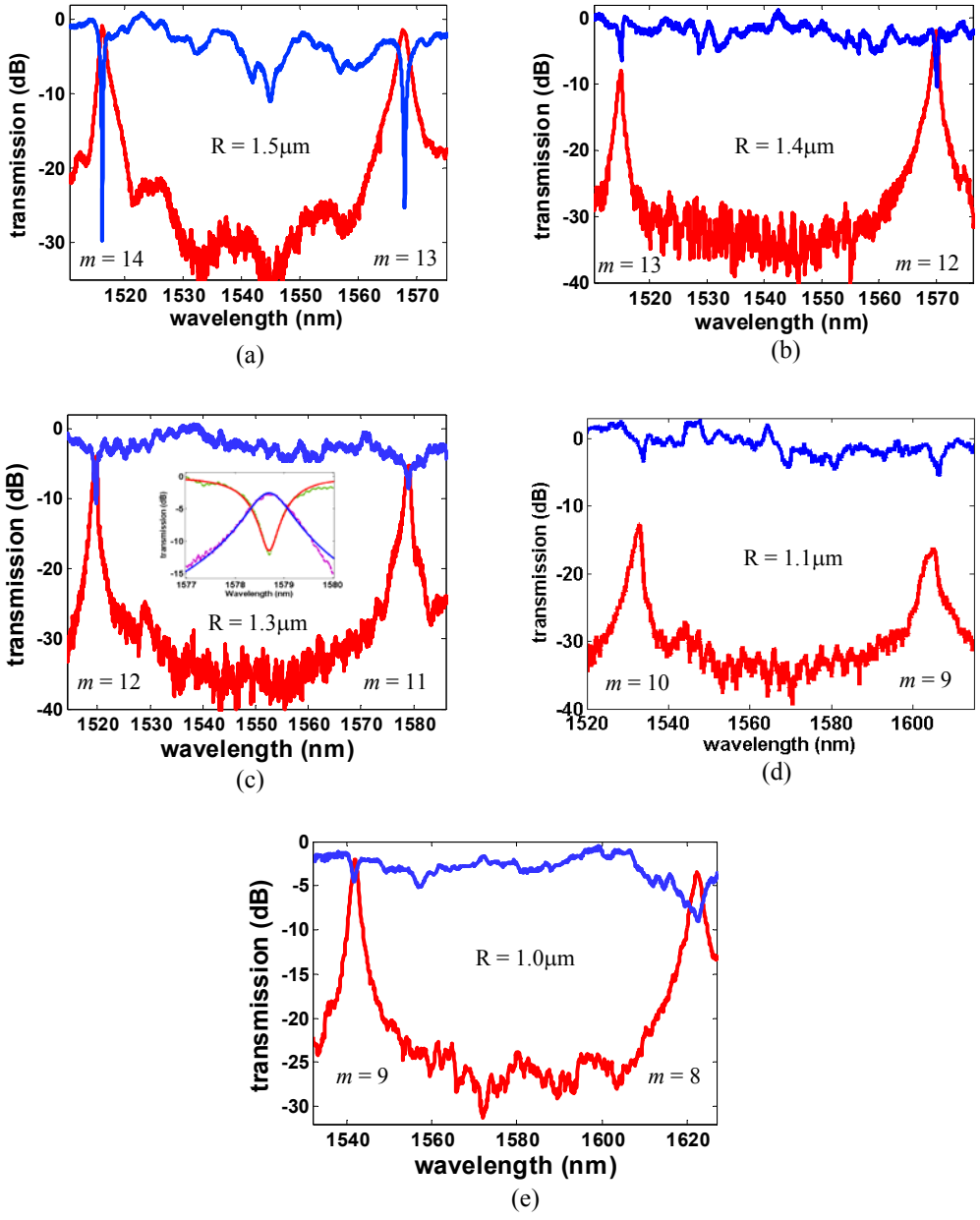

Figure 5.10. Measured spectral responses at the drop port (red) and through port (blue) of microring resonators with radius of (a) 1.5 μm, (b) 1.4 μm, (c) 1.3 μm, (d) 1.1 μm, (e) 1.0 μm. The number *m* indicates the cavity mode number. The inset in (c) shows a theoretical curve fit of the resonance spectrum at 1580 nm of the 1.3 μm microring.

the bus waveguides were 200 ± 5 nm. The SEM images of the 1.5 and 1.0 μm devices are shown in Figure 5.9. With TM polarized input light, the spectral responses measured at the through port and drop port of the microrings with radii 1.5 - 1.0 μm are plotted in Figure 5.10.

Radius (μm)	FSR (nm)	Bandwidth (nm)	Insertion Loss (dB)	Coupling coefficient κ	Roundtrip loss (dB)	Intrinsic Q factor
1.5	52	1.2	0.95	0.076	0.11	23,280
1.4	55	1.0	1.9	0.034	0.045	40,280
1.3	59.6	1.0	2.1	0.070	0.079	26,430
1.1	71.7	3.0	15	0.047	0.52	1,920
1.0	80.5	3.3	0.85	0.073	0.35	5460

Table 5.1. Measured and extracted device parameters for SOI microring resonators with radii between 1.0μm–1.5 μm.

From the spectral measurements, the 3 dB bandwidth, FSR and peak insertion loss of each device were obtained and the results are tabulated in Table 5.1 [86]. The results show that for the smallest microring with 1.0 μm radius, an extremely wide FSR of 80.5 nm was obtained with an insertion loss of only ~1 dB. The excessive insertion loss observed in the 1.1 μm-radius microring was most likely due to fabrication anomaly which affected the coupling junctions. By performing curve fitting on the measured spectral responses, the ring-bus coupling coefficient and the roundtrip loss of each microring were extracted. A typical curve fit is shown in the inset of Figure 5.10(c) for the 1.3 μm-radius microring at the 1580 nm resonant wavelength. The extracted field coupling coefficient κ and the total roundtrip loss for each device are also listed in Table 5.1. Note that the roundtrip loss values in Table 5.1 represent the total roundtrip loss, which includes the bending loss, coupling junction loss, and surface roughness scattering loss.

To assess the loss contribution due to coupling junction scattering, 3D finite difference time domain (FDTD) simulations of the coupling junctions between a straight waveguide and bent waveguides of radii from 1.0 to 1.5 μm were performed. The coupling gap was fixed at 200 nm. The simulated roundtrip coupling loss is plotted as a function of the microring radius (black dashed line) in Figure 5.11 (a). The coupling loss varies inversely with the radius, which is expected since a small bend radius represents a more abrupt change in the coupling junction. Subtracting the coupling loss from the measured total roundtrip loss, we obtained the experimental intrinsic loss of the fabricated microrings. In Figure 5.11 (a) the extracted experimental intrinsic loss (red diamonds) is plotted against the theoretical intrinsic loss due to

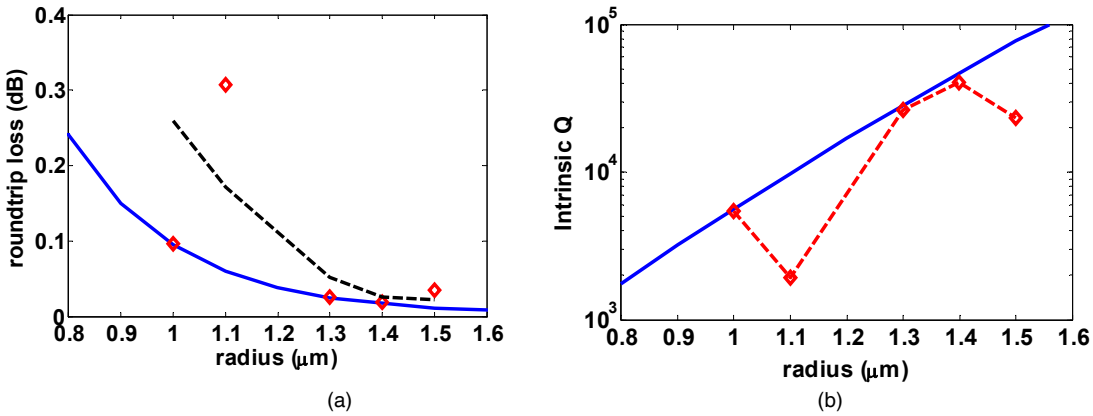

Figure 5.11. (a) Theoretical roundtrip bending loss (blue line), coupling junction loss (dashed black line) and measured intrinsic roundtrip loss (red diamonds) of microring resonators as function of radius. (b) Experimental values (red diamonds) and theoretical limit (blue line) of intrinsic Q factors of microring resonators as function of radius.

bending (blue line). The extracted and theoretical values are in good agreement except for the 1.1 μm-radius microring which was affected by fabrication anomaly. It is noted that as the microring radius approaches 1.0 μm, the coupling junction loss has a significant contribution to the total roundtrip loss, while the bending loss seems to play a less dominant role.

Using the experimental intrinsic loss values in Figure 5.11(a), the intrinsic Q factors of the fabricated devices were computed. The results are shown in Table 5.1 and are also plotted in Figure 5.11(b) (red diamonds). For comparison, the theoretical Q factors due to bending loss alone, which represent the theoretical limit of achievable intrinsic Q values, are plotted in Figure 5.11(b) (blue line). The excellent match between the experimental and theoretical values show that the intrinsic Q factors of our fabricated microring resonators (in particular, the 1.0, 1.3, and 1.4 μm devices) are very close to the theoretically achievable limit.

Finally, the group index n_g of the SOI microrings were also computed from the measured FSR values of the resonators using the relation $FSR_\lambda \approx \lambda^2 / 2\pi R n_g$, where λ = 1550 nm. Figure 5.12 shows the group index as a function of the microring radius. It is noted that the group index decreases from ~4.95 for R = 1.4, 1.5 μm to 4.75 for R = 1.0μm. The decrease in the group index with decreasing R can be explained by the fact that as R decreases, the mode in the microring waveguide becomes

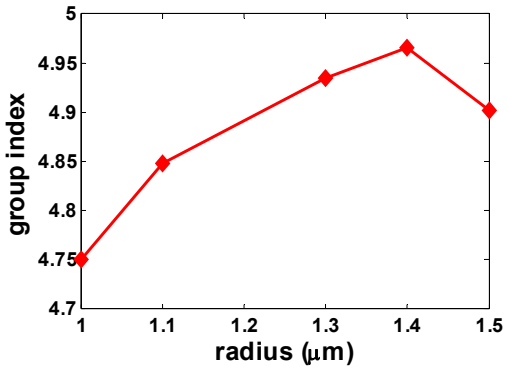

Figure 5.12. Measured group index of ultra-compact microring resonators as function of the radius.

more loosely bound so the strong dispersive effect normally associated with the silicon waveguide core becomes less dominant. The drop in the group index of the 1.5 μm device (as well as its Q-factor in Figure 5.11(b)) is most likely due to proximity effect in the lithography process which may have caused a slight reduction of the coupling gap compared to the other devices.

In summary we showed that ultra-compact microring add-drop filters with relatively low insertion loss are achievable for microring radii as small as 1 μm. Theoretical simulations also indicated that the microring bending loss can be significantly improved by choosing an appropriate aspect ratio for the ring waveguide. We also showed that for ultra-compact microring add-drop filters, the dominant source of loss comes from scattering at the coupling junctions rather than the bending loss.

5.3 Realization of a parallel cascaded microring ladder filter

After validating the developed fabrication process with the demonstration of ultra compact single microring filters, we next attempted to realize high-order SOI microring filters based on the ladder architecture. In particular we would like to realize a 4^{th}-order elliptic optical filter with the following specifications:

- 25 GHz bandwidth,
- < 0.05 dB ripple in the passband,
- out-of-band rejection of –40 dB.

The transmission and reflection transfer functions of the prototype fourth-order filter are given as

$$T_t(s) = \frac{P(s)}{Q(s)} = \frac{0.24064s^2 - 1.4017}{s^4 + 2.1307s^3 + 3.2975s^2 + 2.886s + 1.4086}, \tag{5.1}$$

$$T_r(s) = \frac{R(s)}{Q(s)} = \frac{s^4 + 1.0276s^2 + 0.13926}{s^4 + 2.1307s^3 + 3.2975s^2 + 2.886s + 1.4086}, \tag{5.2}$$

where the normalized 3 dB bandwidth frequency is ω_c = 1 rad/s. The transmission response has four poles at p_k = {-0.2706 ± j1.1923, -0.7947 ± j0.5575}, and two transmission zeros at z_k = {± j 2.4135} on the imaginary axis. The reflection transfer function T_r has four imaginary transmission zeros at r_k = {± j 0.9311, ± j 0.4008}. Figure 5.13 shows the amplitude spectral responses computed from the filter transfer functions.

Using the parallel-cascaded microring filter synthesis procedure in Chapter 4, the above filter transfer functions were synthesized using a double-microring ladder structure with two cascaded stages and a differential π-phase shift. Note that the transfer functions in equations 5.1 and 5.2 can be synthesized either with the 2D coupled architecture or the parallel cascaded architecture. However, the parallel-cascaded microring topology

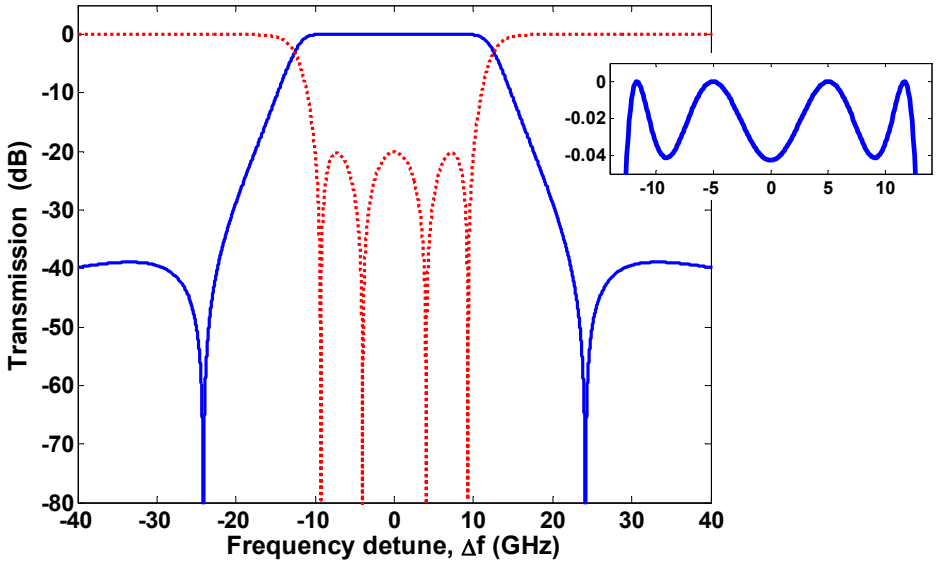

Figure 5.13. Amplitude responses of the transmission (solid) and reflection transfer function (dotted) of the 4th-order 25 GHz-bandwidth elliptic filter. The inset shows a close-up view of the passband.

was chosen over the 2D microring topology because it is much simpler to implement a single π phase shift element connecting two stages than realizing a negative coupling coefficient required in the latter architecture. Figure 5.14 illustrates the layout of the designed parallel cascaded double-microring filter. The microring and bus waveguide width W is 300 nm. The radius of the microring is 8μm and the center-to-center distance between the 2 microring stages is L = 25 μm. Table 5.2 shows the field coupling coefficients and the corresponding coupling gaps of the filter design. The designed coupling gaps in Table 5.2 were determined using the coupled-mode theory [87].

The π-phase shift connecting the two microring stages was realized with a taper waveguide structure as shown in Figure 5.14. The taper phase shift element was chosen to simplify the mask layout. Here the π-phase shift between the upper bus taper waveguide and the lower bus waveguide is achieved by introducing an effective index difference between them. Based on 2D-FDTD numerical simulations, we chose the upper bus waveguide width W_c of the π-phase shift section to be 600 nm. To connect the 600 nm waveguide section with the 300 nm waveguides without any abrupt changes, tapered waveguides of length L_t = 5 μm were introduced on both sides of the 600 nm waveguide. From simulations, the required length of the wide waveguide section of the π-phase shift was found to be L_c=1.65 μm.

	Stage 1			Stage 2		
Field coupling coefficients	κ_0 = 0.27	κ_1 = 0.05	κ_2 = 0.27	κ_3 = 0.14	κ_4 = 0.11	κ_5 = 0.14
Designed coupling gaps	g_0 = 200	g_1 = 340	g_2 = 200	g_3 = 265	g_4 = 265	g_5 = 265
Measured coupling gaps	265 ±10	432 ±10	267 ± 10	335 ±10	339 ±10	333 ±10

Table 5.2: Field coupling coefficients and the corresponding designed and measured coupling gaps of a 4th-order elliptic microring ladder filter with 2 stages. All the coupling gaps are in nm.

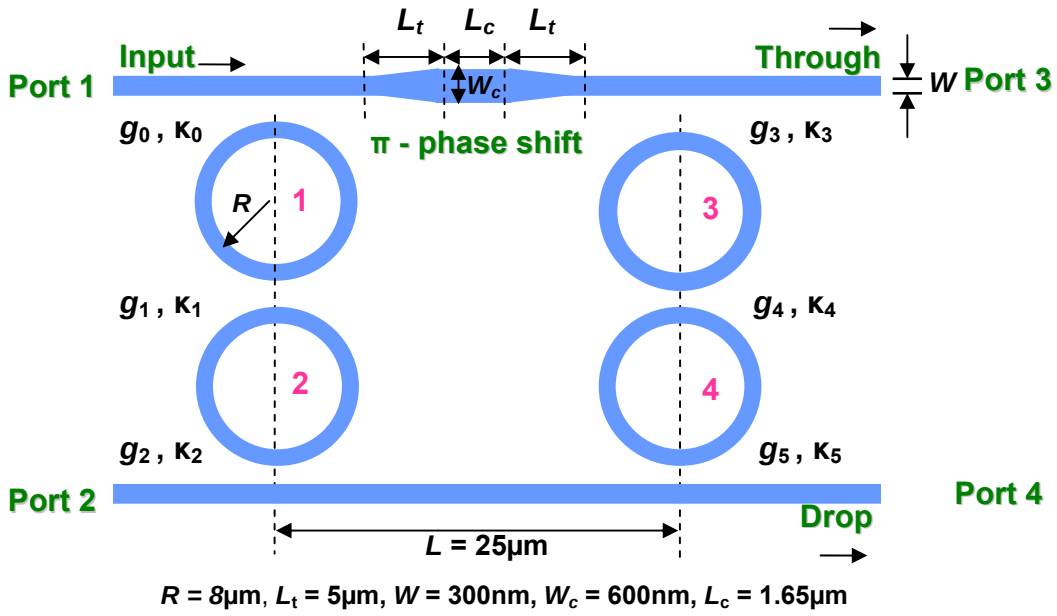

Figure 5.14. Schematic of the fourth-order double-microring ladder filter.

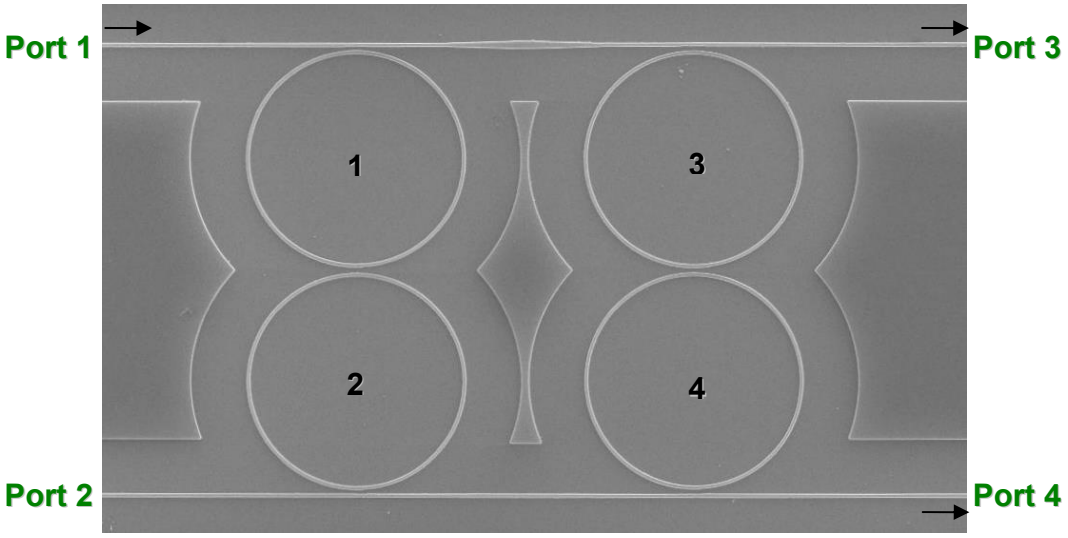

Figure 5.15. SEM image of the fourth-order double-microring ladder filter.

Figure 5.15 shows an SEM image of the fabricated SOI double-microring ladder filter. The measured coupling gaps of the device are also listed in Table 5.2. The measured waveguide widths and radii of the rings are 265±10 nm and 8 μm, respectively. It is seen that for this device, the fabricated waveguide widths and coupling gap values

are largely mismatched from the designed values. This is mainly due to exposure dosage variation within the particular EBL writing job which caused a narrowing of the waveguide widths and a corresponding increase in the coupling gaps.

The chip was then cleaved and the device was measured. The measured spectral responses with input light in TM polarization at port 1 and port 2 (defined in Figure 5.13) are shown in Figure 5.16 (a) and (b) respectively. It can be seen that the port 3 response (dotted red) with input at port 1, and port 4 response (dotted red) with input at port 2 are different from one another. The resonance dips in the port 3 response shown in Figure 5.16 (a) are due to microrings 1 and 3, while microrings 2 and 4 induce

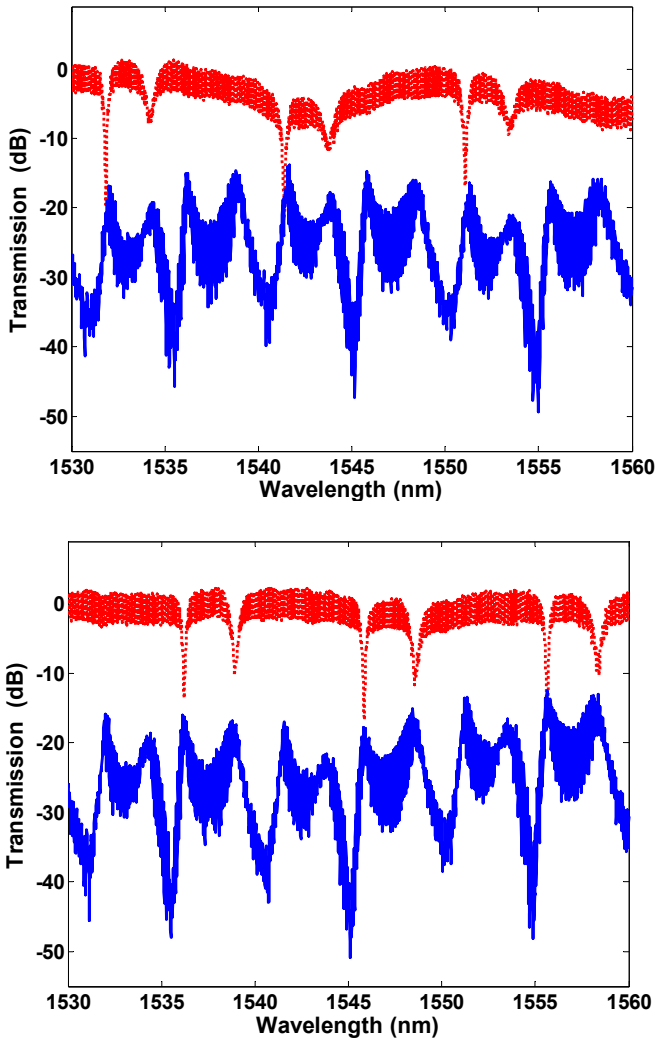

Figure 5.16. (a) Measured spectral responses at the port 3 (dotted red line) and port 4 (blue line) of the microring doublet with input in port 1 (b) Measured spectral responses at the port 4 (dotted red line) and port 3 (blue line) of the microring doublet with input in port 2.

the resonance dips in the port 4 response shown in Figure 5.16 (b). On the other hand, the port 4 response (blue) with input at port 1 and port 3 response (blue) with input at port 2 are similar because, in both the cases, the light goes through all four microrings before exiting at the drop port. It is clear from the measured responses that all four microring resonators are detuned from each other, resulting in the measured filter response being drastically different from the theoretical response in Figure 5.13. The detuned microrings are attributed mainly to fabrication variations in the device dimensions. In order for the device to work as designed, it is clear that a post-fabrication method for adjusting the microring resonances is needed to correct for the resonance mismatch.

5.4 Thermal tuning of silicon microring resonators

In the previous section we saw that due to imperfections introduced during the fabrication process, the physical dimensions of the fabricated microrings deviate from the designed values. This leads to unintended shifts in the microring resonances. One way to control this is by performing post fabrication resonance tuning for each microring, for example, by causing a small change in the refractive index of the silicon microring to correspondingly shift its resonance. To achieve a change in the refractive index one can use the thermo-optic effect in silicon by applying localized heating at each microring. This requires micro scale heaters to be installed precisely on top of each microring. Thin metal wires with micrometer scale dimensions can act as heater elements due to the resistance of the wires and the corresponding joule heating. In this section we describe our work on developing a process for fabricating micro heaters to achieve thermal tuning of silicon microrings.

5.4.1 Design of micro heaters

The micro heaters were to be positioned on top of the microrings as illustrated in the schematic shown in Figure 5.17. Figure 5.18 depicts the cross-sectional view of a chip with a heater element. The micro heaters are made of a thin metal film such as Gold (Au) or Titanium (Ti) fabricated into a serpentine shape which covers the top of the microrings. These thin metal films have high resistivity given their small dimensions so

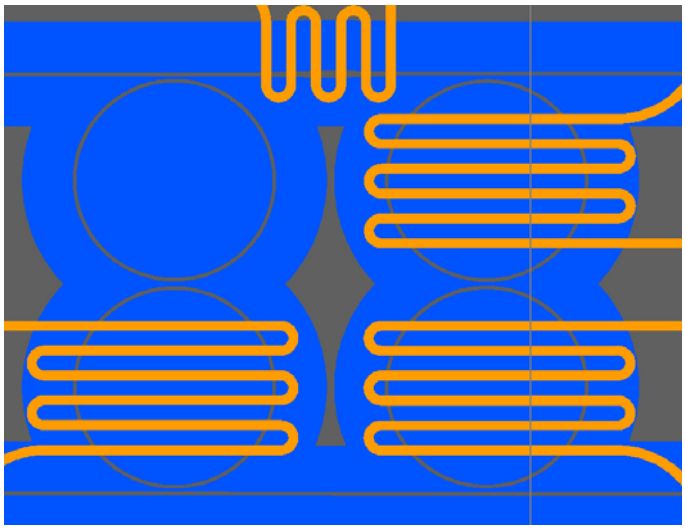

Figure 5.17. Top view of the heater elements to be fabricated on top of the microrings.

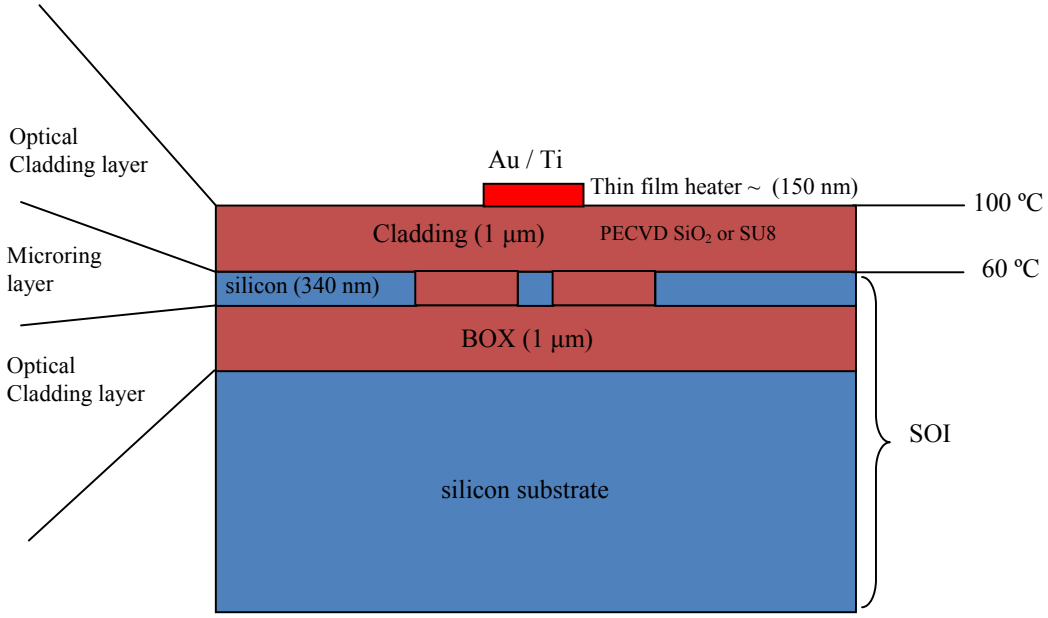

Figure 5.18. Cross sectional view of the heater elements to be fabricated on top of the microrings.

that when a DC current is passed through them, the power dissipation due to I^2R losses in the thin film leads to a temperature rise in the cladding region immediately below the heater. This temperature rise then diffuses down through the cladding layer and heats the silicon waveguide, causing its refractive index to decrease. The serpentine shape of the micro heater is used to achieve longer length of the heating element over a smaller

surface area. The long heater length gives a higher resistance and requires less DC current to achieve a desired power dissipation. The top SiO_2 cladding layer serves two purposes. It provides optical isolation for the waveguide modes in the top vertical direction from the metal layer (heater element). It also eliminates the topography of the silicon layer where the microrings are fabricated and provides a flat surface for the heaters to be fabricated. The design approach used to design the micro heaters is as follows:

1) First the worst case resonance shift required in a microring is determined. From the knowledge of the FSR of the microrings, it can be deduced that the worst case shift ($\Delta\lambda$) is half of the FSR value.

$$\Delta\lambda = \frac{1}{2} FSR \,. \tag{5.3}$$

For an operating wavelength of λ_0 = 1.55 μm, R = 8 μm and n_g = 4.7, the FSR is calculated to be 10.17 nm which gives the worst case wavelength shift $\Delta\lambda$ = 5.085 nm for our device.

2) Given the amount of tuning required ($\Delta\lambda$) for the worst case scenario, the rise in temperature (ΔT) needed at the microring with SiO_2 cladding is given by [88]:

$$\frac{\Delta\lambda}{\Delta T} = \frac{\lambda_0}{n_g}\left(\frac{dn_{eff}}{dT}\right) = \frac{\lambda_0}{n_g}\left(\frac{\Delta n_{eff}}{\Delta n_{core}} . \frac{dn}{dT}_{core(Si)} + \frac{\Delta n_{eff}}{\Delta n_{clad}} . \frac{dn}{dT}_{clad(SiO_2)}\right) \tag{5.4}$$

where n_{eff} is the effective index and $\frac{dn}{dT}$ is the thermo-optic coefficient of the material. Given the thermo-optic coefficients of silicon and SiO_2 as 1.86×10^{-4} K^{-1} and 1.5×10^{-5} K^{-1} respectively, we calculated the tuning sensitivity to be $\frac{\Delta\lambda}{\Delta T}$ = 75 pm.K^{-1}, which gives a worst case temperature rise of 68 K. Converting to celsius and adding the room temperature of 22 °C gives us a temperature of 90 °C to be maintained at the waveguide core. The effects due to thermal expansion were found to be small and negligible.

3) Once the temperature required to be maintained at the waveguide core is calculated, we used a finite difference method to solve the 1D heat diffusion equation to get an approximate estimate of the temperature to be maintained at the top of the cladding layer (T_{top}). Assuming 1μm SiO_2 cladding thickness (t_{clad}), it was estimated that the cladding thermal loss accounts for 40 °C, which makes T_{top} to be 130 °C. Using Fourier's law of heat conduction for 1D in a steady state case, the power P_{top} required to maintain this temperature at the top of the cladding layer is

$$P_{top} = \frac{kA_{surf}(\Delta T)}{t_{clad}}, \tag{5.5}$$

where k = 1.4 W/(m·K) is the thermal conductivity of SiO_2, t_{clad} is the cladding thickness, A_{surf} is the heating surface area on top of the microring. For a A_{surf} = $65\text{x}10^{-12}$ m^2, P_{top} was approximately estimated to be 10 mW.

4) Assuming negligible radiation and convection losses, the power dissipation in the thin film metal heater at a given DC current I_{dc} would be completely transferred to the cladding as P_{top}. Then the amount of thin film resistance R_{thin} required to dissipate this power P_{top} can be calculated as

$$R_{thin} = \frac{P_{top}}{I_{dc}^2}. \tag{5.6}$$

5) Given a particular metal of choice, the dimensions of the heating element can then be calculated from the value of R_{thin} as

$$R_{thin} = \frac{\rho L}{bh}, \tag{5.7}$$

where ρ is the resistivity of the metal used, L is the total length of the heater, b is the width and h is the thickness of the cross section of the heater.

Assuming the heater material to be gold (ρ = 22.14x10^{-9} Ω.m), the thin film resistance required would be 100Ω for a DC current I_{dc} = 10 mA. For a heater cross-section dimensions of b = 500 nm, h = 100 nm, we calculated the required heater length L = 225 μm. The resistivity of the gold thin film can be increased by increasing the thickness of chromium which is usually deposited as an adhesion layer for gold. This results in reduced heater lengths around the range of 100 - 150 nm.

5.4.2 Fabrication of micro heaters

The implementation of heaters on the silicon microring resonators requires additional fabrication steps to be developed. The new fabrication process flow used to install the micro heaters on top of the microrings is shown in Figure 5.19. This process flow assumes that the microrings are already fabricated on the silicon layer and the chip is un-cleaved.

1) ***Cleaning***: Before processing the chip further, an oxygen plasma cleaning was performed to eliminate any resist left from the silicon layer processing. This was followed by a Piranha clean to eliminate any possible organic dust on the surface. A cleaned chip is illustrated in Figure 5.19(a).

2) ***PECVD SiO_2 Deposition and Etch back***: SiO_2 cladding layer of about a micrometer thick was laid on top of the microring layer to provide optical isolation for the waveguide modes from the metal layer as well as to provide a flat surface for the heaters to be fabricated. In order to achieve a good quality cladding layer, SiO_2 deposition based on Plasma Enhanced Chemical Vapour Deposition (PECVD) process was used. The choice of SiO_2 as a cladding layer also compliments the underlying BOX layer providing a uniform refractive index environment around the silicon waveguides. However, simply depositing a 1 μm thick SiO_2 would replicate the topography with all the features from the silicon layer. In order to eliminate the silicon layer topography, a 10 μm thick SiO_2 layer was deposited which filled in and closed all the trenches and left the top surface relatively flat as shown in Figure 5.19(b). The 10 μm thick SiO_2 layer required

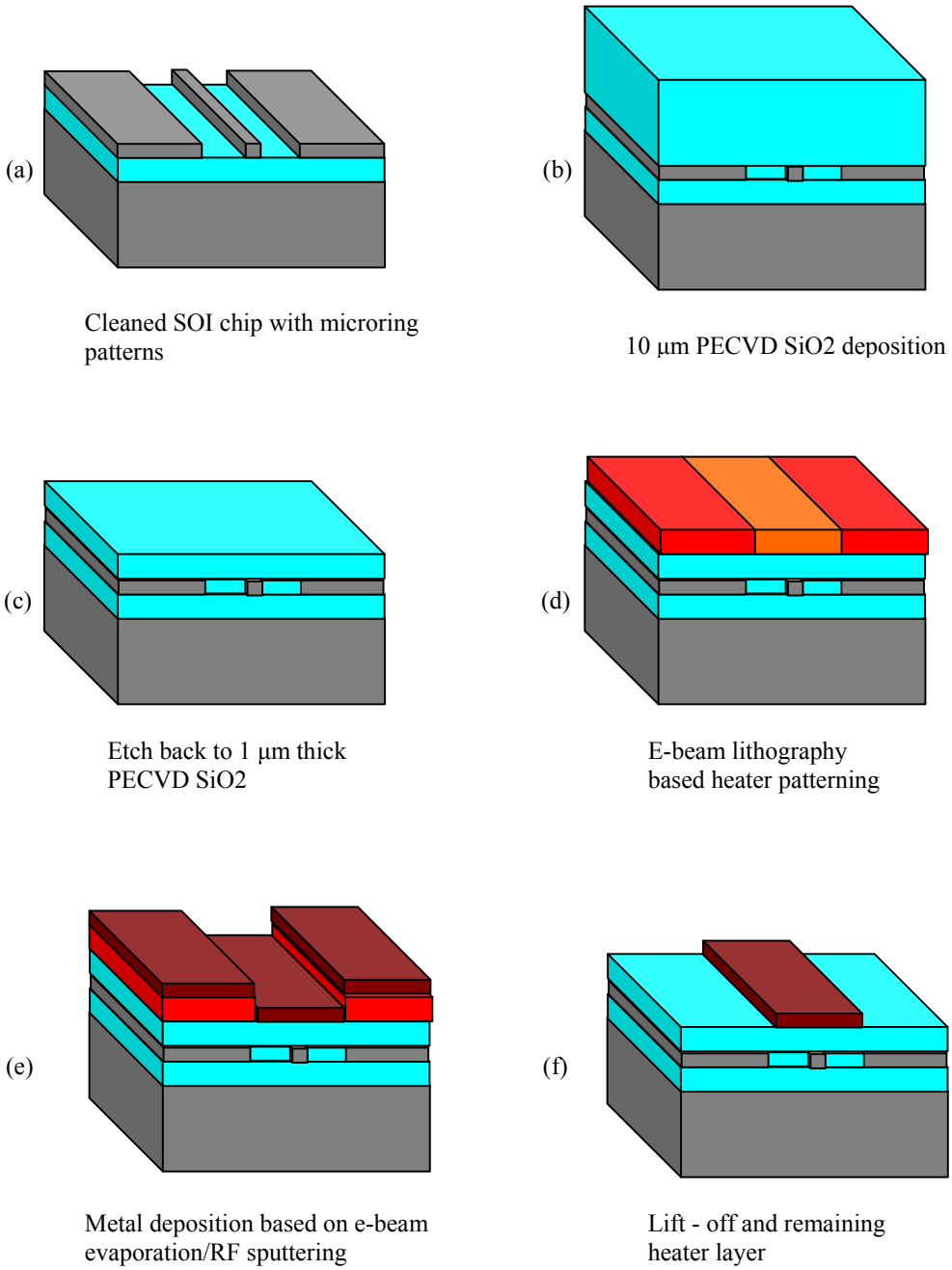

Figure 5.19 Thin film heater fabrication process flow.

multiple cycles of PECVD SiO_2 deposition interspersed with clean cycles at ultrasonic Acetone bath. Using a blanket etch process, 9 micrometers of the cladding layer was etched back leaving a relatively flat 1 µm thick SiO_2 layer ready for heater fabrication as shown in Figure 5.19(c). The SiO_2 blanket etch was performed with the STS reactive ion etching (RIE) machine.

3) ***Electron beam lithography***: Electron beam lithography's overlay process for precise multi-layer patterning was used to align and pattern the heaters precisely on top of the microrings. To achieve the ~ 1 μm sized features of the heater and to meet the requirements of the subsequent lift off process, a thicker EBL resist (PMMA A7) was used which provided a 600 nm thick layer @ 4000 rpm spin speed. The electron beam write process was done in two steps. In the first step the serpentine areas as well as all the features less than 2 μm were written with a 30 kV accelerating voltage at a 30 μm aperture. The remaining big features, which still required electron beam based precision alignment, were written in a de-focused state using a 120 μm aperture. The bigger aperture provided high enough beam current to write large features faster. Also the de-focussed electron beam wrote the features with a big spread which helped in writing large non-critical features. Some of the big features were written using the FBMS mode. The EBL patterned chip is depicted in Figure 5.19(d). The electron beam resist development process uses a similar recipe mentioned in section 5.1.1 except that the development time in MIBK:IPA (1:3) was increased to 1 minute due to the thicker resist.

4) ***Metal layer deposition and lift off***: Gold (Au), titanium(Ti), platinum(Pt), titanium/tungsten(TiW) alloy were all identified as good candidates as heater materials. However the final material of choice for the heater was arrived at based on experiments. Initially Au was chosen as the heater material due to the readily available fabrication recipes and ease of processing. A 150 nm of gold was deposited on top of the developed PMMA A7 resist layer using RF sputtering as illustrated in Figure 5.19(e). The lift off process consisted of immersing the chip in acetone bath for 2 hours and subsequently agitating the chip in an ultrasonic acetone bath for 15 minutes. The outcome of this process is depicted in Figure 5.19(f). A microscope picture of the well defined serpentine

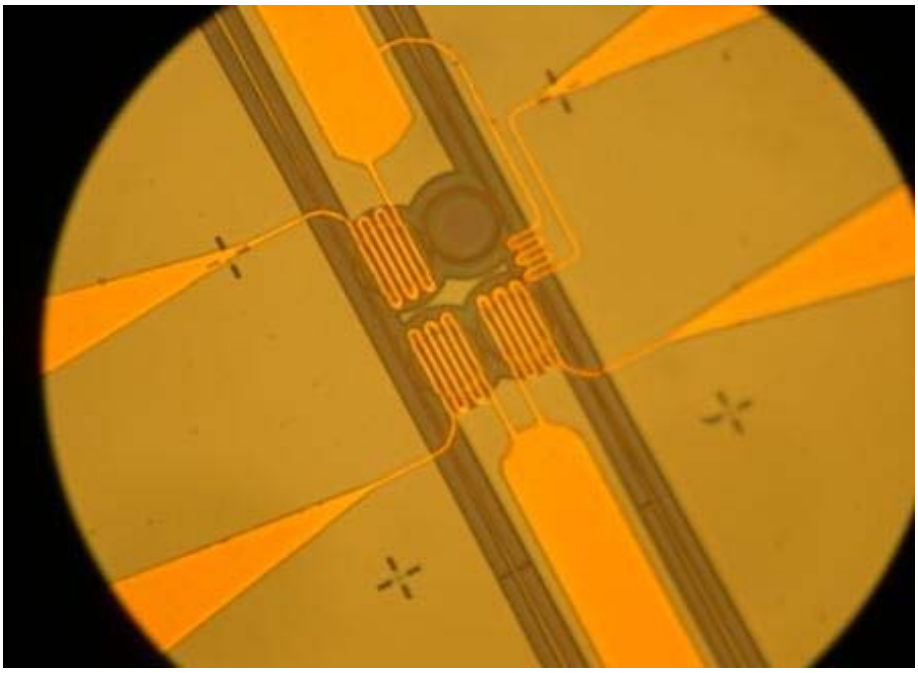

Figure 5.20 Fabricated gold micro heaters.

shape of the gold heaters, precisely aligned on top of the microrings can be seen in Figure 5.20. The gold heater's serpentine section had 800 nm width and provided resistance values up to 150 Ω. However, the low current carrying capacity of the heater design and subsequent issues with electro-migration at higher current densities eliminated gold as a candidate for the heater. Subsequent experiments with Pt, Ti and TiW alloy based heaters led us to finally choose TiW alloy as the heater material because of its relative improvement in durability as well as the simplicity of the fabrication process.

TiW alloy deposition was done using an RF sputtering process. As this is a non-standard material for sputtering, several experimental depositions were done and the optimum deposition pressure and deposition power were found to be 13 mTorr and 200 Watts, respectively. Figure 5.21 shows the fabricated micro heaters based on TiW alloy. The TiW film has a resistivity of 0.58×10^{-6} Ω.m, which is higher than Au and provided resistances in the order of several kΩ.

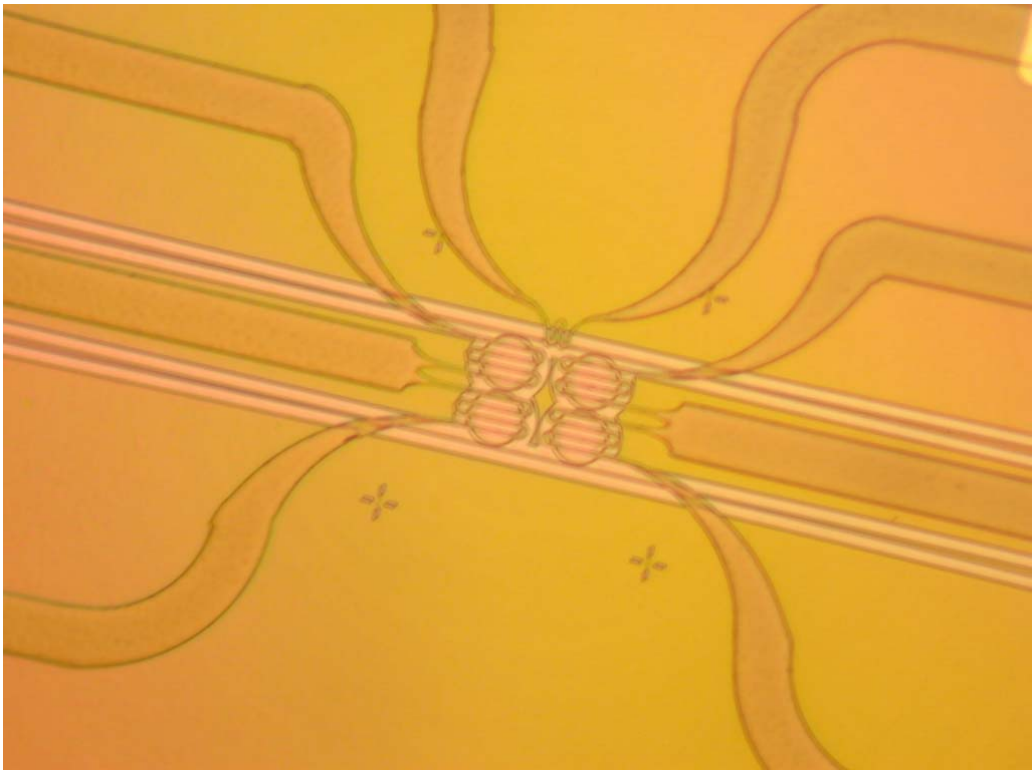

Figure 5.21. TiW alloy based heaters.

5) ***Bonding pads and Wire bonding***: Once the heaters were fabricated they were connected to aluminum(Al) bonding pads. Optical lithography, RF sputtering and lift-off processes were used to define the bonding pads. The chip was then cleaved to expose the optical waveguides for butt coupling with the optical fibres. The cleaved chip was then mounted onto a slot in a custom made printed circuit board (PCB) using an epoxy as shown in Figure 5.22. Thin wires of gauge 26 were used to connect the pads between the PCB and the chip. Electrically conductive silver(Ag) epoxy from MG Chemicals was used to perform the wire bonding between the PCB tracks and the bonding pads on the chip. The wire bonding was manually done under a microscope and the resulting bonds can be clearly seen in Figure 5.22.

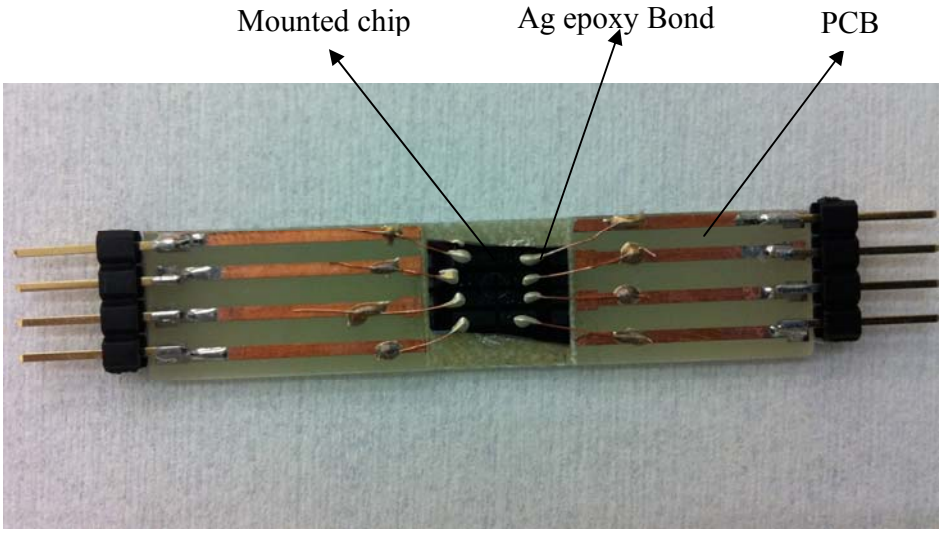

Figure 5.22. The PCB mounted, wire bonded chip.

5.4.3 Thermally tuned microring filter response

To test the thermal tuning of the microring filter response, the chip mounted PCB was connected to multiple DC current sources. Each micro heater element was connected to a LM 334 based variable current control circuitry. The adjustable current source circuits were capable of supplying up to 10 mA of DC current in increments of 100 µA. The TiW micro heaters in Figure 5.23 were measured to have the following resistances:

Micro heater 1 = 5.8 kΩ

Micro heater 2 = 4.2 kΩ

Micro heater 3 = 5.7 kΩ

Micro heater 4 = 4 kΩ

Micro heater 5 = 2 kΩ

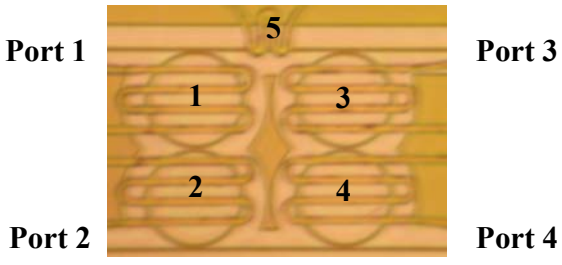

Figure 5.23. TiW heaters with corresponding numbers.

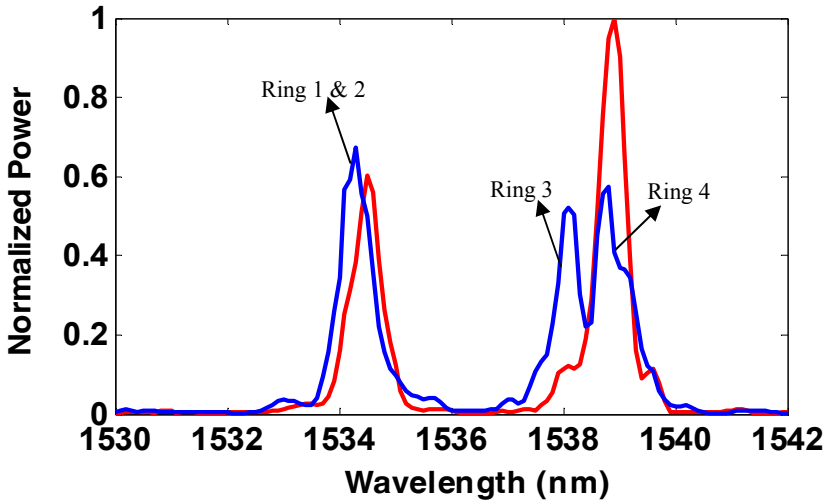

Figure 5.24. Drop port responses with no thermal tuning (blue curve) and response with tuning of heaters 1 and 3 (red curve).

TM polarized CW light was input at port 1 of the device and the drop port transmission response was measured at port 4. Figure 5.24 shows the initial drop port (port 4) spectral response (blue curve) of the fabricated device without thermal tuning. The resonance peak corresponding to each microring is labelled. Initially microheater 1 was tested to assess the performance of the heaters. By applying a DC current in increments, it was observed that the resonance of microring 1 had a red shift at the rate of 0.8 nm/mA. Next we applied 1mA DC current to the micro heaters 1 and 3 which resulted in the drop port spectral response shown by the red curve in Figure 5.24. It can be seen that the resonance of microring 3 has shifted and aligned with resonance of microring 4. The thermal tuning of microring 1 has also shifted the aligned resonance peaks of microrings 1 and 2 slightly.

By adjusting the DC currents flowing through each of the micro heaters, the corresponding resonances of the microrings were tuned until all the resonances were aligned together as shown in Figure 5.25. The thermally aligned peak in Figure 5.25 was attained with micro heaters 1 & 2 maintained at 6.0 mA and micro heaters 3 and 4 maintained at 2.0 mA and 1.0 mA respectively. Further adjustment of this aligned peak by fine tuning the heaters was attempted in order to produce the designed filter response. However, over heating caused micro heaters 1, 2 and 3 to be destroyed and this unfortunately rendered the chip without full thermal tuning capability.

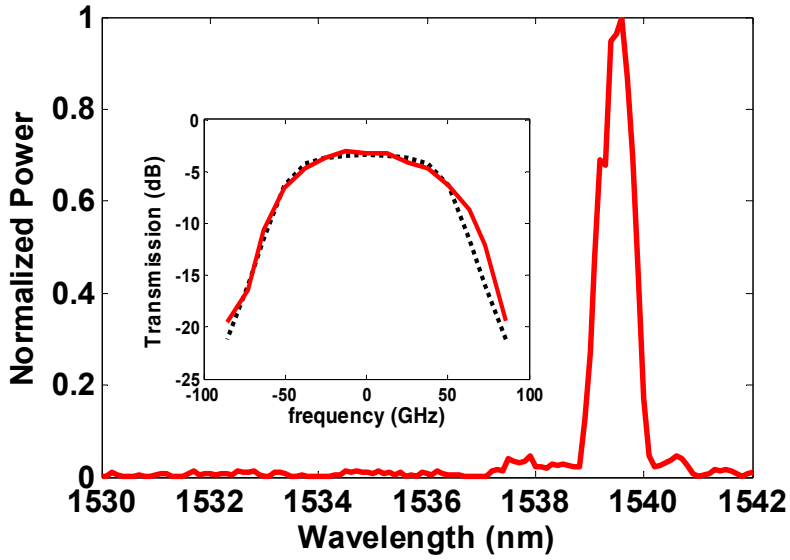

Figure. 5.25. Drop port response with final tuned resonances with appropriate thermal tuning at each micro heater. The Inset shows the curve fit performed on the thermally tuned peak.

Nevertheless the aligned resonance peak obtained in Figure 5.25 could be further analyzed to investigate the response of the ladder filter. From the plot, we obtained a 3dB bandwidth of 100 GHz and an insertion loss of 3.5 dB. The FSR was measured to be 10.5 nm (1.31 THz), which corresponds to a round trip time T_{rt} of 0.764 ps. We next performed a numerical curve fit on the aligned peak using the energy coupling model of the microring ladder filter to extract the device parameters. The result is shown in the inset of Figure 5.25. A good fit was achieved between the measured and the theoretical response. The corresponding extracted energy coupling and field coupling coefficients of the device are shown in Table 5.3.

Energy couplings	Field couplings	Other parameters
$\mu_0 = 12.4\ ns^{-1}$	$\kappa_0 = 0.342$	Loss $\gamma_L = 39.8\ ns^{-1}$
$\mu_1 = 306.2\ ns^{-1}$	$\kappa_1 = 0.234$	Phase shift $\psi = -1$
$\mu_2 = 12.4\ ns^{-1}$	$\kappa_2 = 0.342$	
$\mu_3 = 20.18\ ns^{-1}$	$\kappa_3 = 0.558$	
$\mu_4 = 102.8\ ns^{-1}$	$\kappa_4 = 0.0785$	
$\mu_5 = 20.18\ ns^{-1}$	$\kappa_5 = 0.558$	

Table 5.3. Extracted device parameters from the curve fit.

Although the extracted parameters have largely deviated from the original design parameters, the curve fit validates the fourth order filter response of the fabricated microring ladder structure.

The heater burnout was the primary reason for the inability to further fine tune the filter, to achieve the designed filter response. On inspecting the destroyed heaters it was found that there were unintended sharp bends in the metal due to the localized surface roughness in the PECVD oxide layer. PECVD oxide experiences a process called *flaking* when depositing very thick films. During flaking, the deposited oxide tends to form clumps causing localized surface imperfections of the order of 100 nm. If a surface imperfection is a trench of 100 nm deep, it causes the metal laid on top of it to bend abruptly into this trench. These sharp bends cause higher current density to localize at those locations, causing very high power dissipation and eventual burn out of the heaters. One way to overcome this problem is to use a good quality spin-on-glass (SOG) solution spun on top of the PECVD oxide to smooth out the localized surface roughness, or to completely replace the PECVD oxide layer by a thick SOG layer. Another approach could be to use a chemical mechanical polishing (CMP) process to smooth out the SiO_2 surface.

5.5 Summary

In this chapter we developed the fabrication process to experimentally demonstrate microring add-drop filters in the SOI material system. Initially single microring add-drop filters were demonstrated. We then explored the potential for miniaturization of silicon microrings and showed that ultra-compact microring add-drop filters with insertion loss around 1dB are achievable for microring radii as small as 1μm. We also attempted to demonstrate a fourth order microring ladder filter which highlighted the necessity for post fabrication resonance tuning. Additional fabrication process to install microheaters on top of the microrings was developed and a thermally tuned fourth order microring ladder filter response was demonstrated.

Chapter 6

Conclusions

Although the industry has gone forward with the demonstration of SOI microring based WDM devices, most of those devices are still based on single microring resonators. In a truly dense WDM system single microring devices cannot offer the required spectral characteristics like high adjacent channel isolation and flat top passband. Without using densely packed WDM channels, silicon based optical interconnects would become an overhead rather than being a simple, elegant solution. Therefore, the ability to realize high-order microring filters with advanced spectral characteristics is important for future silicon optical interconnect technology.

Given this background the goal of this research work was to explore, propose and demonstrate new coupled resonator topologies based on compact microring resonators in the SOI material system which can be used to realize advanced optical filters. In this thesis work we have proposed and analyzed two new microring architectures that are capable of realizing complex optical transfer functions. We also developed the synthesis procedures for these architectures.

In order to demonstrate the proposed architectures, we developed a fabrication process flow for the silicon-on-insulator material system at the University of Alberta nanofabrication facility. Several single microring add-drop filter devices were demonstrated during which we also explored the feasibility of realizing extremely

miniaturized microrings. This effort resulted in the successful demonstration of a 1um radius add-drop microring resonator with a low insertion loss.

We attempted to demonstrate a fourth order add-drop microring filter using the proposed parallel-cascaded microring network architecture. Due to fabrication induced resonance mismatch among the microrings, it was found necessary to use a post fabrication microring resonance tuning method. This prompted us to develop additional fabrication processes to install micro sized heaters on top of the microrings. Using these heaters we thermally tuned the microrings and demonstrated a fourth order filter response.

6.1 Key contributions of the thesis work

6.1.1 General 2D coupled microring topology

In this thesis we proposed two microring architectures capable of realizing high-order optical transfer functions containing transmission zeros. The first architecture is based on a 2D array of direct-coupled asynchronous microring resonators. A direct analytical synthesis procedure was developed which allows arbitrary filter shapes to be designed and realized. In order to demonstrate the versatility of the proposed architecture and the synthesis technique, three numerical examples were provided illustrating spectral properties such as symmetric spectral response with transmission zeros, asymmetric filter response and a response with both flat transmission amplitude and group delay. A disadvantage of the proposed architecture is that it requires at least one negative coupling element for filters with transmission zeros on the imaginary axis. Negative coupling requires long coupling lengths which makes the fabrication challenging.

6.1.2 General cascaded microring network topology

To overcome the above disadvantage with the 2D direct-coupled microring topology, a second architecture was proposed based on cascaded microring networks that can realize symmetric filter responses with transmission zeros without the need for any negative coupling elements. Effectively, the new architecture decomposes a 2D microring network containing negative coupling elements to a parallel cascade of smaller networks, each containing only positive coupling elements. A synthesis technique was developed

by which the target optical transfer function is split into multiple stages and each individual stage is then synthesized and optimized separately. Both the 2D coupling topology and cascaded network architecture were shown to provide multiple possible device layouts for the same filter response, from which an optimum design in terms of ease of fabrication can be chosen.

6.1.3 Demonstration of ultra-compact silicon microring resonators

We explored the feasibility of reducing the foot print of silicon microring resonators by reducing the bending radii. Through numerical analysis the impact of bending loss on shrinking the microring radius was analyzed for different microring waveguide aspect ratios and polarizations. It was found that by choosing the right waveguide aspect ratio one can achieve very small microring resonators high quality factors for a given polarization. Bending loss limited theoretical intrinsic Q factor in the order of several thousands was shown to be achievable even for a ring radius as small as 1μm. This was confirmed with experimental demonstrations. For 1μm ring radius, a bending loss limited intrinsic Q-factor of over 5000 was demonstrated, which was found to be in good agreement with the numerical prediction. These demonstrations could pave the way for realizing large scale densely integrated silicon photonic systems in the future.

6.1.4 Demonstration of a silicon microring ladder filter response

A fourth order filter based on the cascaded microring network architecture was fabricated. To correct the resonance mismatch due to fabrication errors, thermo-optical tuning of the microring resonances was employed which required the microrings to be equipped with microheaters on top. By applying some initial thermal tuning to the fabricated microring ladder device, a fourth order spectral response was achieved although the observed spectral characteristics had largely deviated from the target design. Finer tuning to achieve better filter response was not possible due to a breakdown of the microheaters. A better microheater design along with an improved planarization method could provide more stable heaters that would allow finer control over the resonance tuning so that the target filter shape could be achieved.

6.2 Future research directions

6.2.1 Post fabrication tuning of microring devices

The demonstration of the fourth order microring filter illustrated the lingering issues associated with fabrication errors and the corresponding resonance de-tunings that accompany such multiple microring based devices. Thermo-optic tuning has been used as a post-fabrication tuning mechanism in the research arena to achieve the desired filter characteristics. However, it may not be feasible to install micro sized heaters in a dense WDM system with several tens of channels accommodated in it due to the amount of power dissipation required to tune these microrings. For our device a maximum power of 200mW in microheater1 was required for tuning approximately over 5nm of wavelength range. The additional fabrication steps (section 5.4.2) involved in installing the microheaters is a costly overhead. Post fabrication tuning mechanisms that make a permanent correction based on UV based polymer cladding [89, 90] have been proposed to overcome this issue. Recently another potential post fabrication tuning methodology based on femtosecond laser ablation was proposed and demonstrated [91]. Here the resonance of the silicon microring was tuned by shooting a femtosecond laser pulse at it. It was shown that by controlling the amount of energy in the laser pulse shot, the amount of tuning can be controlled. Although more research needs to be done on this, it is a promising technique that could provide a simple low cost alternative.

6.2.2 High-order microring filters

The permanent post fabrication methodologies discussed in the previous section could pave the way for an easier way to realize the proposed high-order microring filters in the future. With a reliable low cost post fabrication tuning method available, a future direction of this research would be to use the proposed microring architectures to demonstrate other advanced optical signal processing functions such as dispersion compensation and maximally flat group delay filters for optical buffering. Also exploring and demonstrating the modularized filter design technique afforded by the cascaded microring network architecture is another direction for this research. Such an approach would allow extremely high order filters (e.g., $N > 10$) to be realized. This would involve decomposing a given transfer function into multiple modules, where each

module may not even need to reside on the same chip. Each module could be realized on a separate chip which then can be optimized individually after fabrication. Finally all the modules could be put together via optical fibre connections to realize the complete filter. Such an implementation strategy would also have high failure tolerance, since in the even that a filter stage fails; only this stage has to be replaced without discarding the entire filter.

Bibliography

1) M. J. Kobrinsky, B. A. Block, J.-F. Zheng, BC Barnett, E. Mohammed, M. Reshotko, F. Robertson, S. List, I. Young, and K. Cadien, “On-chip optical interconnects,” Intel Technology Journal, Vol. 8, No.2, pp.129-143, 2004.

2) IEEE 802.3 Gigabit Ethernet Standard, 1000Base-SX for short wavelength transceivers (850 nm) and multimode fibre.

3) IEEE Std 802.3ae-2002: Amendment: Media Access Control (MAC) Parameters, Physical Layers, and Management Parameters for 10 Gbps Operation.

4) ANSI INCITS 364-2003: Information Technology - Fibre Channel 10 Gigabit (10GFC).

5) Intel Lightpeak white paper - http://techresearch.intel.com/spaw2/uploads/files/Intel Light Peak White Paper_0910.pdf, 2009.

6) O. Rits, M. D. Wilde, G. Roelkens, R. Bockstaele, R. Annen, M. Bossard, F. Marion, and R. Baets, “2D parallel optical interconnects between CMOS ICs,” Proceedings of the SPIE, Optoelectronic Integrated Circuits VIII, 6124, 2001.

7) J. V. Erps, C. Debaes, M. Vervaeke, L. Desmet, N. Hendrickx, G V. Steenberge, H. Ottevaere, P. Vynck, V. Gomez, S. V. Overmeire, Y. Ishii, P. V. Daele, A. Hermanne, and H. Thienpont, “Low-cost micro-optics for PCB-level photonic interconnects,” Proceedings of the SPIE, Optoelectronic Integrated Circuits IX, 6476, 2007.

8) R. A. Soref, "The past, present, and future of silicon photonics," IEEE Journal of Selected Topics in Quantum Electronics, Vol. 12, No. 6, pp. 1678-1687, 2006.

9) B. Jalali and S. Fathpour, “Silicon Photonics,” IEEE/OSA Journal of Lightwave Technology, Vol. 24, No. 12, pp. 4600-4615, 2006.

10) W. Bogaerts, P. Dumon, D. Van Thourhout, D. Taillaert, P. Jaenen, J. Wouters, S. Beckx, and R. Baets, “Compact Wavelength-Selective Functions in silicon-on-Insulator Photonic Wires,” IEEE Journal of Selected Topics in Quantum Electronics, Vol. 12, No. 6, pp. 1394-1401, 2006.

11) N. Izhaky, M. T. Morse, S. Koehl, O. Cohen, D. Rubin, A. Barkai, G. Sarid, R. Cohen, and M. J. Paniccia, “Development of CMOS-compatible integrated silicon photonics devices,” IEEE Journal of Selected Topics in Quantum Electronics, Vol. 12, No. 6, pp. 1688-1698, 2006.

12) A. Liu, R. Jones, L. Liao, D. Samara-Rubio, D. Rubin, O. Cohen, R. Nicolaescu, and M. J. Paniccia., “A high-speed silicon optical modulator based on a metal-oxide-semiconductor capacitor,” Nature, Vol. 427, pp. 615-618, 2004.

13) Q. Xu, B. Schmidt, S. Pradhan, and M. Lipson, “Micrometre-scale silicon electro-optic modulator,” Nature, Vol. 435, pp. 325-327, 2005.

14) W. M. J. Green, M. J. Rooks, L. Sekaric, and Y. A. Vlasov, “Ultra-compact, low RF power, 10 Gb/s silicon Mach-Zehnder modulator,” Optics Express, Vol.15, No. 25, pp. 17106-17113, 2007.

15) P. Dong, S. Liao, D. Feng, H. Liang, D. Zheng, R. Shafiiha, C. C. Kung, W. Qian, G. Li, X. Zheng, A. V. Krishnamoorthy, and M. Asghari, “Low V_{pp}, ultralow-energy, compact, high-speed silicon electro-optic modulator,” Optics Express, Vol.17, No. 25, pp. 22484-22490, 2009.

16) H. Rong, A. Liu, R. Jones, O. Cohen, D. Hak, R. Nicolaescu, A. Fang, and M. J. Paniccia, “An all-silicon Raman laser,” Nature, Vol. 433, pp. 292-294, 2005.

17) Y. A. Vlasov, W. M. J. Green, and F. Xia, “High-throughput silicon nanophotonic wavelength-insensitive switch for on-chip optical networks,” Nature Photonics, Vol. 2, pp. 242-246, 2008.

18) N. Sherwood-Droz, H. Wang, L. Chen, B. G. Lee, A. Biberman, K. Bergman, and M. Lipson, “Optical 4x4 hitless silicon router for optical Networks-on-Chip (NoC),” Optics Express, Vol. 16, No. 23, pp. 15915-15922, 2008.

19) J. V. Campenhout, W. M. J. Green, S. Assefa, and Y. A. Vlasov, “Low-power, 2×2 silicon electro-optic switch with 110-nm bandwidth for broadband reconfigurable optical networks,” Optics Express, Vol. 17, No. 26, pp. 24020-24029, 2009.

20) H. Park, A. W. Fang, S. Kodama, and J. E. Bowers, "Hybrid silicon evanescent laser fabricated with a silicon waveguide and III-V offset quantum wells," Optics Express, Vol. 13, No. 23, pp. 9460-9464, 2005.

21) A. W. Fang, H. Park, O. Cohen, R. Jones, M. J. Paniccia, and J. E. Bowers, “Electrically pumped hybrid AlGaInAs-silicon evanescent laser,” Optics Express, Vol. 14, No. 20, pp. 9203-9210, 2006.

22) A. W. Fang, E. Lively, Y. H. Kuo, D. Liang, and J. E. Bowers, “A distributed feedback silicon evanescent laser,” Optics Express, Vol. 16, No. 7, pp. 4413-4419, 2008.

23) D. Liang, M. Fiorentino, T. Okumura, H. H. Chang, D. T. Spencer, Y. H. Kuo, A. W. Fang, D. Dai, R. G. Beausoleil, and J. E. Bowers, “Electrically-pumped

compact hybrid silicon microring lasers for optical interconnects," Optics Express, Vol. 17, No. 22, pp. 20355-20364, 2009.

24) L. Liu, J. V. Campenhout, G. Roelkens, R. A. Soref, D. Van Thourhout, P. Rojo-Romeo, P. Regreny, C. Seassal, J. M. Fédéli, and R. Baets, "Carrier-injection-based electro-optic modulator on silicon-on-insulator with a heterogeneously integrated III-V microdisk cavity," Optics Letters, Vol. 33, No. 28, pp. 2518-2520, 2008.

25) H. W. Chen, Y. Kuo, and J. E. Bowers, "Hybrid silicon modulators," Chinese Optics Letters, Vol. 7, pp. 280-285, 2009.

26) H. Park, A. W. Fang, R. Jones, O. Cohen, O. Raday, M. N. Sysak, M. J. Paniccia, and J. E. Bowers, "A hybrid AlGaInAs-silicon evanescent waveguide photodetector," Optics Express, Vol. 15, No. 10, pp. 6044-6052, 2007.

27) L. Chen, and M. Lipson, "Ultra-low capacitance and high speed germanium photodetectors on silicon," Optics Express, Vol. 17, No. 10, pp. 7901-7906, 2009.

28) A. Alduino, L. Liao, R. Jones, M. Morse, B. Kim, W. Lo, J. Basak, B. Koch, H. Liu, H. Rong, M. Sysak, C. Krause, R. Saba, D. Lazar, L. Horwitz, R. Bar, S. Litski, A. Liu, K. Sullivan, O. Dosunmu, N. Na, T. Yin, F. Haubensack, I. Hsieh, J. Heck, R. Beatty, H. Park, J. Bovington, S. Lee, H. Nguyen, H. Au, K. Nguyen, P. Merani, M. Hakami, and M. J. Paniccia, "Demonstration of a High Speed 4-Channel Integrated silicon Photonics WDM Link with Hybrid silicon Lasers," Integrated Photonics Research, silicon and Nanophotonics topical meeting, p. PDIWI5, 2010.

29) K. J. Vahala, "Optical microcavities," Nature, Vol. 424, pp. 839-846, 2003.

30) B.E. Little, S. T. Chu,W. Pan, D. Ripin, T. Kaneko, Y. Kokubun, and E. Ippen, "Vertically coupled glass microring resonator channel dropping filters," IEEE Photonic Technology Letters, Vol. 11, No. 2, pp. 215-217, 1999.

31) Y. Yanagase, S. Suzuki, Y. Kokubun, and S. T. Chu, "Box-Like Filter Response and Expansion of FSR by a Vertically Triple Coupled Microring Resonator Filter," IEEE/OSA Journal of Lightwave Technology, Vol. 20, No. 8, pp. 1525-1529, 2002.

32) D. J. W. Klunder, E. Krioukov, F. S. Tan, T. van der Veen, H. F. Bulthuis, G. Sengo, C. Otto, H. J.W.M. Hoekstra, and A. Driessen, "Vertically and laterally waveguide-coupled cylindrical microresonators in Si3N4 on SiO2 technology," Applied Physics B, Vol. 73, pp. 603-608, 2001.

33) T. Barwicz, M. A. Popovíc, P. Rakich, M. Watts, H. Haus, E. Ippen, and H. Smith, "Microring-resonator based add-drop filters in SiN: fabrication and analysis," Optics Express, Vol. 12, No. 7, pp. 1437-1442, 2004.

34) A. Melloni, R. Costa, P. Monguzzi, and M. Martinelli, "Ring-resonator filters in silicon oxynitride technology for dense wavelength-division multiplexing systems," Optics Letters, Vol. 28, No. 17, pp. 1567-1569, 2003.

35) A. Vorckel, M. Monster, W. Henschel, P. H. Bolivar, and H. Kurz, "Asymmetrically coupled silicon-on-Insulator microring resonators for compact add-drop multiplexers," IEEE Photonic Technology Letters, Vol. 15, No. 7, pp. 921-923, 2003.

36) T. Baehr-Jones, M. Hochberg, C. Walker, and A. Scherer, "High-Q ring resonators in thin silicon-on-insulator," Applied Physics Letters, Vol. 85, No. 16, pp. 3346-3347, 2004.

37) D. Rafizadeh, J. P. Zhang, S. C. Hagness, A. Taflove, K. A. Stair, and S. T. Ho, "Waveguide-coupled AlGaAs/GaAs microcavity ring and disk resonators with high finesse and 21.6 nm free spectral range," Optics Letters, Vol. 22, No. 16, pp. 1244-1246, 1997.

38) R. Grover, P. P. Absil, V. Van, J. V. Hryniewicz, B. E. Little, O. King, L. C. Calhoun, F. G. Johnson, and P.-T. Ho, "Vertically coupled GaInAsP--InP microring resonators," Optics Letters, Vol. 26, No. 8, pp. 506-508, 2001.

39) P. Rabiei, W. H. Steier, Z. Cheng, and L. R. Dalton, "Polymer microring filters and modulators," IEEE/OSA Journal of Lightwave Technology, Vol. 20, No. 11, pp. 1968-1975, 2002.

40) W.-Y. Chen, R. Grover, T. A. Ibrahim, V. Van, W. N. Herman, and P.-T. Ho, "High-finesse laterally coupled single-mode benzocyclobutene microring resonators," IEEE Photonic Technology Letters, Vol. 16, No. 2, pp. 470-472, 2004.

41) S. T. Chu, B. E. Little, V. Van, J. V. Hryniewicz, P. P. Absil, F. G. Johnson, D. Gill, O. King, F. Seiferth, M. Trakalo, and J. Shanton, "Compact full C-band tunable filters for 50GHz channel spacing based on high-order micro-ring resonators," Optical Fiber Communication Conference, p.PDP9, 2004.

42) C. K. Madsen, and G. Lenz, "Optical all-pass filters for phase response design with applications for dispersion compensation," IEEE Photonic Technology Letters, Vol. 10, No. 7, pp. 994-996, 1998.

43) C. K. Madsen, S. Chandrasekhar, E. J. Laskowski, M. A. Cappuzzo, J. Bailey, E. Chen, L. T. Gomez, A. Griffin, R. Long, M. Rasras, A. Wong-Foy, L. W. Stulz, J. Weld, and Y. Low, "An integrated tunable chromatic dispersion compensator

for 40 Gb/s NRZ and CSRZ," Optical Fiber Communication Conference, p.FD9-1, 2002.

44) F. Xia, L. Sekaric, and Y. A. Vlasov, "Ultracompact optical buffers on a silicon chip," Nature Photonics, Vol. 1, pp. 65-71, 2007.

45) F. Coppinger, C. K. Madsen, and B. Jalali, "Photonic microwave filtering using coherently coupled integrated ring resonators," Microwave and Optical Technology Letters, Vol. 21, No.2, pp. 90-93, 1999.

46) T. Paloczi, J. Scheuer, and A. Yariv, "Compact Microring-Based Wavelength-Selective Inline Optical Reflector," IEEE Photonic Technology Letters, Vol. 17, No. 2, pp. 390-392, 2005.

47) B.E. Little, S.T. Chu, H.A. Haus, J.S. Foresi, and J.-P. Laine, "Microring resonator channel dropping filters," IEEE/OSA Journal of Lightwave Technology, Vol. 15, No. 6, pp. 998-1005, 1997.

48) V. Van, "Circuit-based method for synthesizing serially-coupled microring filters," IEEE/OSA Journal of Lightwave Technology, Vol. 24, No. 7, pp. 2912-2919, 2006.

49) J. V. Hryniewicz, P. P. Absil, B. E. Little, R. A. Wilson, and P.-T. Ho, "Higher order filter response in coupled microring resonators," IEEE Photonic Technology Letters, Vol. 12, No. 3, pp. 320 – 322, 2000.

50) J. K. S. Poon, L. Zhu, G. A. DeRose, and A. Yariv, "Transmission and group delay of microring coupled-resonator optical waveguides," Optics Letters, Vol. 31, No. 4, pp. 456-458, 2006.

51) S. Xiao, M. H. Khan, H. Shen, and M. Qi, “Highly Compact High-Order Micro-Ring Filters,” Conference on Lasers and Electro-Optics, p.CFQ6, 2007.

52) F. Xia, M. Rooks, L. Sekaric, and Y. A. Vlasov, “Ultra-compact high order ring resonator filters using submicron silicon photonic wires for on-chip optical interconnects,” Optics Express, Vol. 15, No. 19, pp. 11934-11941, 2007.

53) B. E. Little, S. T. Chu, J. V. Hryniewicz, and P. P. Absil, “Filter synthesis for periodically coupled microring resonators,” Optics Letters, Vol. 25, No. 5, pp. 344-346, 2000.

54) S. Y. Cho and R. A. Soref, “Apodized SCISSORs for filtering and switching,” Optics Express, Vol. 16, No. 23, pp. 19078-19090, 2008.

55) R. Grover, V. Van, T. A. Ibrahim, P. P. Absil, L. C. Calhoun, F. G. Johnson, J. V. Hryniewicz, and P.-T. Ho, “Parallel-cascaded semiconductor microring resonators for high-order and wide-FSR filters,” IEEE/OSA Journal of Lightwave Technology, Vol. 20, No. 5, pp. 900-905, 2002.

56) T. Ito and Y. Kokubun, “Fabrication of a 1 x 2 interleaver by parallel-coupled microring resonators,” Electronics and Communication in Japan, Vol. 89, pp. 56-64, 2006.

57) K. Jinguji, “Synthesis of coherent two-port optical delay-line circuit with ring waveguides,” IEEE/OSA Journal of Lightwave Technology, Vol. 14, No. 8, pp. 1882-1898, 1996.

58) C. K. Madsen, “Efficient architectures for exactly realizing optical filters with optimum bandpass design,” IEEE Photonic Technology Letters, Vol. 10, No. 8, pp. 1136-1138, 1998.

59) M. S. Rasras, D. M. Gill, S. S. Patel, K.-Y. Tu, Y.-K. Chen, A. E. White, A. T. Pomerene, D. N. Carothers, M. J. Grove, D. K. Sparacin, J. Michel, M. A. Beals, and L. C. Kimerling, "Demonstration of a fourth-order pole-zero optical filter integrated using CMOS processes," IEEE/OSA Journal of Lightwave Technology, Vol. 25, No. 1, pp. 87-92, 2007.

60) V. Van, "Synthesis of elliptic optical filters using mutually-coupled microring resonators," IEEE/OSA Journal of Lightwave Technology, Vol. 25, No. 2, pp. 584-590, 2007.

61) A. M. Prabhu and V. Van, "Predistortion Techniques for Synthesizing Coupled Microring Filters with Loss," Optics Communications, Vol. 281, pp. 2760-2767, 2008.

62) E. Atia and A. E. Williams, "Narrow-bandpass waveguide filters," IEEE Transactions on Microwave Theory and Techniques, Vol. 20, No. 4, pp. 258-265, 1972.

63) E. Atia, A. E. Williams, and R. W. Newcomb, "Narrow-band multiple-coupled cavity synthesis," IEEE Transactions on Circuits and Systems, Vol. 21, No. 5, pp. 649-655, 1974.

64) R. J. Cameron, "General coupling matrix synthesis methods for Chebyshev filtering functions," IEEE Transactions on Microwave Theory and Techniques, Vol. 47, No. 4, pp. 433-442, 1999.

65) R. J. Cameron, "Advanced coupling matrix synthesis techniques for microwave filters," IEEE Transactions on Microwave Theory and Techniques, Vol. 51, No. 1, pp. 1-10, 2003.

66) Y.F. Lam. *Analog and digitial filters: Design and realization*. Engelwood cliffs, NJ: Prentice-Hall, 1979.

67) A. M. Prabhu and V. Van, "Realization of asymmetric optical filters using asynchronous coupled-microring resonators," Optics Express, Vol. 15, No. 15, pp. 9645-9658, 2007.

68) J. D. Rhodes, "A low pass prototype network for microwave linear phase filters," IEEE Transactions on Microwave Theory and Techniques, Vol. 18, No. 6, pp. 290-301, 1970.

69) H. L. Liew and V. Van, "Exact realization of optical transfer functions with symmetric transmission zeros using the double-microring ladder architecture," IEEE/OSA Journal of Lightwave Technology, Vol. 26, No. 14, pp. 2323-2331, 2008.

70) V. Belevitch. *Classical Network Theory*. San Francisco, CA: Holden-Day, 1968.

71) A. Fettweis, "On the factorization of transfer matrices of lossless two-ports," IEEE Transactions on Circuit Theory, Vol. 17, No. 1, pp. 86–94, 1970.

72) A. M. Prabhu, H. L. Liew and V. Van, "Generalized parallel-cascaded microring networks for spectral engineering applications," Journal of optical society of America B, Vol. 25, No. 9, pp. 1505-1514, 2008.

73) A. Ogura, "Method of fabricating SOI substrate," US Patent No. 5888297, 1999.

74) K. Mitani and U. M. Gösele, "Wafer bonding technology for silicon-on-lnsulator applications: A review," Journal of Electronic Materials, Vol. 21, No. 7, pp. 669-676, 1992.

75) M. Bruel, B. Aspar, B. Charlet, C. Maleville, T. Poumeyrol, A. Soubie, H. Auberton-Herve, J. Lamure, T. Barge, F. Metral, and S. Trucchi, "Smart-cut: a promising new SOI material technology," IEEE International SOI Conference proceedings, pp. 178-179, 1995.

76) R. Wuest, F. Robin, C. Hunziker, and P. Strasser, "Limitations of proximity effect corrections for electron-beam patterning of planar photonic crystals," Optical Engineering, Vol. 44, No. 4, pp. 043401(1-4), 2005.

77) B. Houli, V. Umansky, and M. Heiblum, "Low energy electron beam lithography with 30 nm resolution," Semiconductor Science and Technology, Vol. 8, No. 7, pp. 1490-1492, 1993.

78) M. Kirchner and M. Kahl, "Raith - Electron Beam Lithography for Research," Proceedings of the III National Conference on Nanotechnology NANO, 2009.

79) F. Laermer and A. Schilp, "Method of anisotropically etching silicon," US Patent No. 5501893, 1999.

80) A. L. Rickard and M. E. McNie, "Characterization and optimization of deep dry etching for MEMS applications," SPIE International Conference on Microelectronic and MEMS Technologies, Proceedings of SPIE 4407, p. 78, 2001.

81) S. Xiao, M. H. Khan, H. Shen, and M. Qi, "Silicon-on-insulator microring add-drop filters with free spectral ranges over 30 nm," IEEE/OSA Journal of Lightwave Technology, Vol. 26, No. 2, pp. 228-236, 2008.

82) M. S. Nawrocka, T. Liu, X. Wang and R. R. Panepucci, "Tunable silicon microring resonator with wide spectral range," Applied Physics Letters, Vol. 89, No. 7, pp. 071110(1-3), 2006.

83) Q. Xu, D. Fattal, and R. G. Beausoleil, “Silicon microring resonators with 1.5-μm radius,” Optics Express, Vol. 16, No. 6, pp. 4309-4315, 2008.

84) A. M. Prabhu, A. Tsay, Z. Han, and V. Van, “Ultracompact SOI Microring Add–Drop Filter With Wide Bandwidth and Wide FSR,” IEEE Photonic Technology Letters, Vol. 21, No. 10, pp. 651-653, 2009.

85) J. Xiao, H. Ma, N. Bai, X. Liu, and X. Sun, “Full-vectorial analysis of bending waveguides using finite difference method based on H-fields in cylindrical coordinate systems,” Optics Communication, Vol. 282, No. 13, pp. 2511-2515, 2009.

86) A. M. Prabhu, A. Tsay, Z. Han, and V. Van, “Extreme miniaturization of silicon add-drop microring filters for VLSI photonics applications,” IEEE Photonics Journal, Vol. 2, No. 3, pp. 436-444, 2010.

87) H. Haus, “Coupling of modes – resonators and couplers,” in *Waves and Fields in Optoelectronics*, Prentice-Hall, pp. 197-234, 1983.

88) R. Amatya, C. W. Holzwarth, F. Gan, H. I. Smith, F. Kärtner, R. J. Ram, and M. A. Popovic, “Low Power Thermal Tuning of Second-Order Microring Resonators,” Conference on Lasers and Electro-Optics/ Quantum Electronics and Laser Science Conference and Photonic Applications Systems Technologies, p. CFQ5, 2007.

89) S. T. Chu, W. Pan, S. Sato, T. Kaneko, B. E. Little, Y. Kokubun, “Wavelength trimming of a microring resonator filter by means of a UV sensitive polymer overlay,” IEEE Photonic Technology Letters, Vol. 11, No. 6, pp. 688-690, 1999.

90) L. Zhou, K. Okamoto, and S. J. B. Yoo, “Athermalizing and Trimming of Slotted silicon Microring Resonators With UV-Sensitive PMMA Upper-Cladding,” IEEE Photonic Technology Letters, Vol. 21, No. 17, pp. 1175-1177, 2009.

91) D. Bachman, Z. Chen, A. M. Prabhu, R. Fedosejevs, Y. Tsui, and V. Van, “Post-Fabrication Tuning of silicon Microring Resonators by Femtosecond Laser Modification,” Integrated Photonics Research, Silicon and Nanophotonics topical meeting, p. IME2, 2011.